χ_c Production at CMS in p+Pb Collisions at $\sqrt{s_{_{NN}}} = 8.16\,\text{TeV}$

By

OTA KUKRAL
DISSERTATION

Submitted in partial satisfaction of the requirements for the degree of

DOCTOR OF PHILOSOPHY

in

Physics

in the

OFFICE OF GRADUATE STUDIES

of the

UNIVERSITY OF CALIFORNIA

DAVIS

Approved:

Manuel Calderón de la Barca Sánchez, Chair

Daniel Cebra

Ramona Vogt

Committee in Charge

2023

Abstract

χ_c Production at CMS in p+Pb Collisions at $\sqrt{s_{_{NN}}} = 8.16\,\text{TeV}$

Measurements of the charmonium P-states χ_{c1} and χ_{c2} are important to understand heavy-quarkonia suppression in a quark-gluon plasma, which is created in heavy-ion collisions at high energies. Various competing processes play a role. To disentangle their effects, it is necessary to measure as many charmonium states as possible across a wide range of collision systems. In this work, the χ_c (1P) states are studied in $p + \text{Pb}$ collisions at a center-of-mass energy per nucleon pair of $\sqrt{s_{_{NN}}} = 8.16\,\text{TeV}$. The analysis is based on data with integrated luminosity of $175\,\text{nb}^{-1}$ that were collected by the CMS experiment at the Large Hadron Collider (LHC) in 2016. The χ_c states are measured via their decay to J/ψ and γ. The J/ψ is then reconstructed through its decay to a muon pair $\mu^+\,\mu^-$, while the γ is detected through its conversion to an electron-positron pair $e^+\,e^-$. The χ_c-to-J/ψ ratio is reported as the final result, in the rapidity range of $|y| < 2.4$ and transverse momentum range of $6.5 < p_\text{T} < 30\,\text{GeV}/c$. The ratio is reported as a function of p_T, y and event activity as approximated by the track multiplicity, N_tracks. The value of the ratio is found to be ≈ 0.2, effectively flat in rapidity and event activity, while showing an increasing trend with p_T. This trend is present in all the rapidity subranges that are considered. The results are compared to previous $p + p$ measurements of the ratio at a similar energy, and to other relevant charmonium results. The χ_c-to-J/ψ ratio values and trends are similar, putting limits on size of the effects which are present in $p + \text{Pb}$ collisions.

To whom it may concern

Contents

List of Figures

List of Tables

Acknowledgments

This work would not have been possible without help and support of many people, both within the scientific community and from the outside. First of all, I would like to thank my graduate advisor, Manuel Calderón de la Barca Sánchez, for his never ending support and enthusiasm. He not only guided my scientific career, but also provided advice and inspiration on various aspects of life throughout my years as a graduate student. I think of Manuel more as of a friend and mentor than as of a supervisor. I'm grateful to my second advisor, Daniel Cebra, for years of continued support and encouragement, both in physics and in sports. Daniel furthermore provided much needed view about what is realistic and achievable, and thus helped me to focus on important things in my work. It was a pleasure to be a graduate student in a group with both Manuel and Daniel as the advisors. I would also like to thank Ramona Vogt, for her invaluable theoretical insight, and for the careful and quick reading and commenting on this dissertation.

I extend many thanks to the members of the CMS heavy ion group, especially my coworkers and peers from the dilepton group. This analysis could not happen without their input and expertise. I thank fellow graduate students from UC Davis, both my colleagues from NPG group and my peers from my year. They made being in UC Davis a wonderful experience. A special thanks goes to my friend Benjamin Godfrey, who read through the dissertation and corrected its English, especially hundreds of omitted or redundant articles.

Finally, I would like to express my deepest gratitude to my family, to my parents Lenka and Ondřej, my brother Jan, and my wife Francesca. This dissertation is dedicated to them.

Chapter 1

Introduction

Quark-gluon plasma (QGP) is a novel state of matter that has been theoretically predicted [1–4] and experimentally observed [5–9] in heavy-ion collisions at very high energies. It is a state of matter where quarks and gluons are deconfined[10, 11], that is, free to move over much larger distances than in normal cold nuclear matter. The interaction of quarks and gluons within the QGP is governed by the strong force described by Quantum Chromodynamics (QCD). The study of the QGP is a major focus of the field of nuclear physics.

The universe during its evolution existed in the QGP state only a very short time ($\approx 1\,\mu s$) after the Big Bang. Nowadays, the energy densities needed for QGP creation are accessible for research in human-made accelerators, which accelerate beams of heavy-ions to relativistic energies on the order of $E =$ GeV–TeV per nucleon. The beams are brought into collision at specific crossing points around which dedicated detectors are built, creating the QGP for an extremely brief instant. It cools, dissipates, and sends particles streaming to the detectors, where they are analyzed. Studying these collisions gives us valuable insight into the QGP, which in turn, teaches us about QCD and the strong interaction.

One of the approaches for studying QGP employs heavy-quarkonia, that is, particles consisting of a bound charm+anti-charm ($c\bar{c}$) or bottom+anti-bottom ($b\bar{b}$) quark pair. These

particles are created early in the initial collision, traverse through the created QGP, and are affected by it. It was predicted that in the presence of the QGP, the heavy-quarkonia should dissolve [12] if the temperature of the QGP is high enough. Different quarkonia states are dissolved at different temperatures [13], which in turn allows us to estimate the temperature of the created QGP, if we know which states dissolved and which did not.

As our understanding of quarkonia and their interactions with the QGP improved, this simple picture of quarkonia as the QGP thermometer became more complicated. There are many possible competing effects confounding the interpretation. In order to disentangle contributions of various effects, it is necessary to study quarkonia in other collision systems, and for a wide range of quarkonia states. The commonly studied systems are proton+proton (p+p) collisions, a relatively simple system serving as a baseline, and proton+heavy-ion (p + A) collisions, which study heavy-ion related effects. The most commonly studied quarkonia states are the orbital angular momentum $L = 0$ states (S-states). This includes J/ψ ($c\bar{c}$ 1S-state) and Υ ($b\bar{b}$ S-states).

This work presents a measurement of χ_c, a $c\bar{c}$ quarkonium P-state with orbital angular momentum $L = 1$. The measurement is performed in p+Pb collisions with $\sqrt{s_{_{NN}}} = 8.16\,\text{TeV}$ at the Compact Muon Solenoid (CMS) experiment at the Large Hadron Collider (LHC). We report the results as the ratio of χ_{c1} and χ_{c2} to J/ψ, i.e. the ratio of the P-states to the S-state. The J/ψ state is relatively well measured, thus, by reporting the ratio, we mainly provide information about the much less explored P-states. The ratio is reported in various kinematic variables to further study χ_c production and modification in p + Pb collisions.

This dissertation is organized into chapters as follows: Chapter 2 provides an overview of our current theoretical understanding and of existing experimental results. Chapter 3 introduces the LHC accelerator, the CMS experiment, and the reconstruction techniques used by the experiment. Chapter 4 describes the data and Monte Carlo samples that were used in this work. Chapter 5 lists the particle selections that were used to extract the

signal, and specifies the details of the fitting procedure. Chapter 6 shows the acceptance and efficiency corrections. Chapter 7 describes the systematic uncertainties. Chapter 8 presents and discusses our final results. Chapter 9 summarizes the dissertation and its findings. There are also two appendices that present studies which have a supplementary character. They explain relevant inquiries that were performed that are not necessary for the full results, but pertain to ancillary studies done as part of this work. Appendix A explains how we derived our conversion selection. Appendix B lists additional crosschecks that were performed to ensure a high quality of data and of the analysis procedure.

Chapter 2

Theoretical background and experimental review

2.1 Standard model

The Standard Model (SM) of particle physics is the commonly accepted model describing the strong, weak, and electromagnetic interactions. The model is the pinnacle of a century of experimental and theoretical development of our understanding of these interactions. It has been validated in countless experiments, including predictions of then-unknown particles, which have since been discovered, such as the top quark t [14, 15], tau neutrino ν_τ [16], and the Higgs boson H [17, 18]. Despite its phenomenal success, we know that the model, in its current form, is incomplete. It does not describe several essential known phenomena, including neutrino oscillations, dark matter and dark energy, and most importantly, the familiar gravitational force. Nonetheless, the model explains the vast majority of the interactions in our daily life. This work describes a measurement that is interpreted within the SM and deals primarily with the strong force.

2.2 QCD and the quark gluon plasma

In the SM, the strong interaction is described by Quantum Chromodynamics (QCD). At low temperatures and densities, QCD matter is in the hadron gas phase, where the relevant degrees of freedom describing the matter are hadronic. As the energy density in the system increases, it undergoes a transition to a new state of matter called quark gluon plasma (QGP). In the QGP, the relevant degrees of freedom are thought to be the individual quarks and gluons. The transition is illustrated in Fig. 2.1, which shows the results from a QCD lattice calculation. As the temperature increases, there is a rapid increase in ϵ/T^4, where ϵ is the energy density and T is the temperature of the system, shown relative to the critical temperature T_c on the x-axis of the figure. The ratio ϵ/T^4 is proportional to the number of degrees of freedom via the equation of state. The red curve is a calculation for the case of two relevant flavors (up and down), blue is a three-flavor calculation (adding strangeness). The green is a calculation for two light and one heavy (strange) flavors. Around the critical temperature T_c, the number of degrees of freedom increases rapidly, regardless of the scenario, signifying that the matter is undergoing a phase transition [19, 20]. The arrows on the right side of the plot show the values in the limit of a non-interacting Stefan-Boltzmann gas. The limit is not reached even for a substantially higher temperature than T_c.

We can draw a phase-space diagram of QCD matter, as functions of the baryochemical potential μ_B and temperature T. The normal cold nuclear matter is at a very low temperature (room temperature is $\approx 0.025\,\text{eV}$), shown in the plot as a black dot. The quark gluon plasma lies in the high-temperature or high-density region. The transition from hadronic gas to the QGP is first order for higher values of μ_B [21] and crossover for small μ_B [22]. The first-order transition curve ends with a critical point, analogous to a critical point in other phase diagrams (e.g. a pressure-temperature phase-space diagram for water).

As mentioned in the introduction, the QGP is created in high-energy heavy-ion collisions.

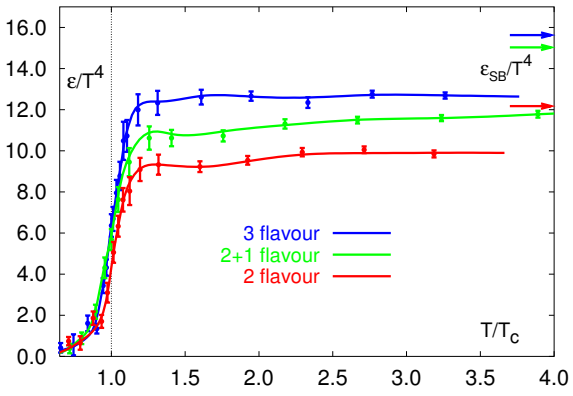

Figure 2.1: Energy density ϵ divided by T^4, plotted as a function of temperature. Three quark scenarios are explored in a lattice calculation. Details are given in the text. Figure from [20].

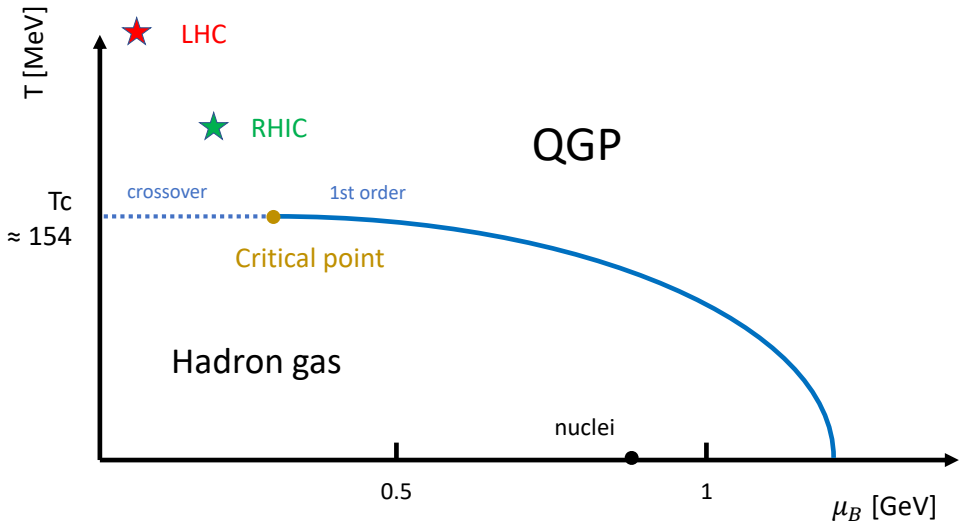

Figure 2.2: QCD phase-space diagram. The QGP occupies a region of high temperature and density.

Two major accelerators producing such $A + A$ collisions are the Relativistic Heavy Ion Collider (RHIC) and the Large Hadron Collider (LHC). The fireball created in the collisions locally thermalizes and can be placed on the diagram. The two stars show the symbolic

location of the QGP created in the respective accelerators. The energy of the LHC is larger than at RHIC, which translates to a higher initial temperature. It is important to note that the QGP is not static, but rather expands and cools immediately. As the QGP passes through the transition region, the quarks and gluons coalesce into hadrons, and the QGP dissipates. This "hadronization" happens through the crossover region for the LHC. At the RHIC, it depends on the specific parameters of the accelerator setting. The search for the exact location of the critical point is a topic of an ongoing research, notably with the RHIC beam energy scan [23].

2.3 Heavy quarkonia

Quarkonia are bound states of a quark q with an antiquark $\overline{q}$ of the same flavor. In other words, they are specific mesons with zero overall flavor. The quarkonia of interest for our study are the heavy quarkonia, where the quark is either charm c or beauty b[1]. The $c\overline{c}$ bound states are called charmonia, and the $b\overline{b}$ are called bottomonia.

2.3.1 Charmonium family

There are many bound states of $c\overline{c}$ pairs. Figure 2.3 shows a schematic diagram of the charmonium family. The left and right panel show the same information. The left panel displays all the states as of 2017. The observed well-established states are depicted as solid black horizontal lines. The solid blue and magenta lines show exotic (non-conventional) charmonium or charmonium-like states. The red dashed horizontal lines are states predicted in Ref. [26]. The various connecting lines show the potential decays between the states with different colors signifying different decay types. Of particular interest are the green lines showing the decays which radiate γ. In individual columns, we have the quantum numbers,

[1]The top quark t decays very quickly and does not form bound states.

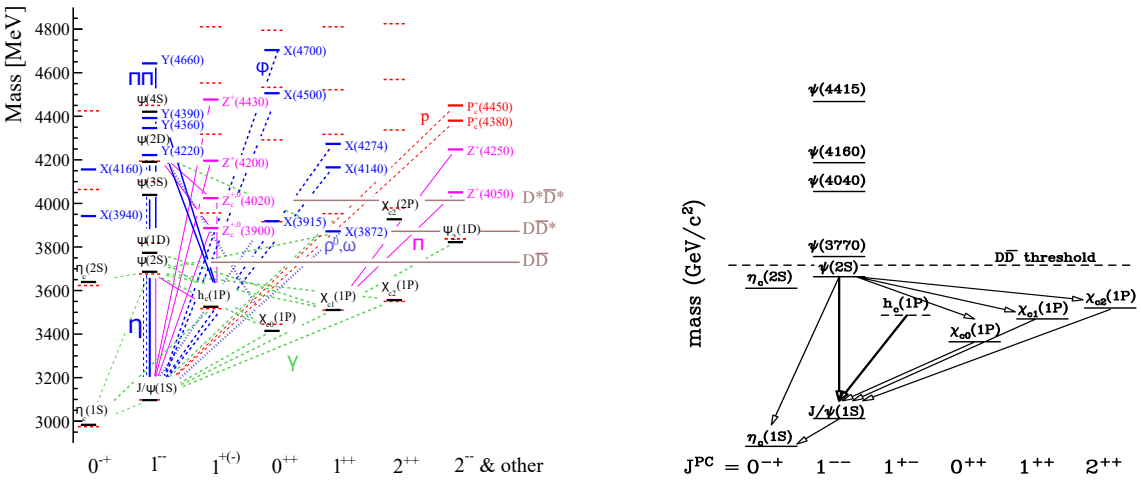

Figure 2.3: Charmonium family states. On the x-axis are their quantum numbers J^{PC}, and on the y-axis are their masses. **Left:** Full picture including recently discovered or speculative states. **Right:** Diagram showing only the main states. Figures from [24] and [25].

denoted by J^{PC}, where J is the total angular momentum, P is the parity and C is the C-parity (for charge conjugation). Plus (minus) stands for even (odd) parity/C-parity. For a quarkonium system, $P = (-1)^{(L+1)}$ and $C = (-1)^{(S+L)}$, where S is the spin, and L is the orbital angular momentum. L is shown in the figure using the spectroscopic notation in the parenthesis behind the name of the state, with $L = \{0, 1, 2, \ldots\}$ noted as $\{\mathrm{S}, \mathrm{P}, \mathrm{D}, \ldots\}$.

The right panel of Fig. 2.3 is the simplified picture that allows us to focus on the essential features relevant for this analysis. The most commonly measured $c\overline{c}$ state is J/ψ, the state that was also the first charmonium state to be discovered [27, 28]. It is a vector meson, with quantum numbers $J = 1$, $S = 1$, and $L = 0$. These numbers give $P = -1$ and $C = -1$, as shown in Fig. 2.3. The next state of note is $\psi(2\mathrm{S})$, also known as ψ', which is an excited state of J/ψ, with the same J, S, and L quantum numbers. In both panels of Fig. 2.3, there is a $D\overline{D}$ threshold line at $M = 2M_D = 3.74\,\mathrm{GeV}$, where D denotes a meson containing a $c/\overline{c}$ and a light antiquark/quark. Above the line, the charmonium states can decay into a

$D\overline{D}$ meson pair via the strong interaction. This decay is energetically forbidden below the threshold. Any states with masses above the threshold line are very short lived, because of the strength of the strong interaction.

In this analysis, we measure the χ_c states. These are the states with orbital momentum $L = 1$ and $S = 1$. The total angular momentum J is a spin addition of L and S, and can thus have three values of $J = 0, 1, 2$ corresponding to the three χ_c states χ_{c0}, χ_{c1}, and χ_{c2}. Table 2.1 summarizes the most important aspects of charmonium states relevant for this analysis. The first six columns list the particle name and basic properties. The next-to-last column shows the decay that is relevant for this analysis, because that is how the particle is detected here. The last column provides the branching ratio for the selected decay. The very low branching ratio for the χ_{c0} state is caused by the particle quantum numbers, which suppress the $J/\psi+\gamma$ decay. The branching ratio is so small that the state cannot be resolved in our experimental data, and it is not considered. This introduces a minor bias, because the state is present, but if we assume equal production of the χ_{c0}, χ_{c1}, and χ_{c2} states, χ_{c0} would comprise only about 2.5% of the total χ_c sample. This is negligible compared to other experimental uncertainties. The last state in Fig. 2.3 that needs to be considered is $h_c(1\mathrm{P})$. This state does not decay radiatively to J/ψ and is not present in our data.

State	**Mass [MeV]**	**Width [MeV]**	**L**	**S**	**J**	**Relevant decay**	**BR. [%]**
J/ψ	3096.900 ± 0000.006	0.0926 ± 0.0017	0	1	1	$\mu^+\,\mu^-$	5.961 ± 0.033
χ_{c0}	3414.71 ± 0000.30	10.8 ± 0.6	1	1	0	$J/\psi + \gamma$	1.40 ± 0.05
χ_{c1}	3510.67 ± 0000.05	0.84 ± 0.04	1	1	1	$J/\psi + \gamma$	34.3 ± 1.0
χ_{c2}	3556.17 ± 0000.07	1.97 ± 0.09	1	1	2	$J/\psi + \gamma$	19.0 ± 0.5

Table 2.1: Basic characteristics of the selected charmonium states. Data from [29].

2.3.2 Quarkonia as a thermometer

One of the reasons why quarkonia are studied is that they can be used to estimate the temperature of the QGP created in heavy-ion collisions. The QGP consists of free quarks and gluons, which carry a color charge. When a quarkonium state is present in the QGP, its binding strength is weakened by the presence of free color charge [12], because the color charge of the quarkonium constituents is screened in a similar fashion to Debye screening in electromagnetic plasma. If the screening is strong enough, the binding becomes so weak that the state dissolves. The color screening is stronger for higher temperatures of the QGP. In an idealized case, a quarkonium state exists below a certain temperature threshold and completely dissolves above that threshold. The binding strengths and radii vary for different quarkonium states, which means that the dissolution thresholds are different. If we can measure which states are dissolved and which are not, we can estimate the temperature of the QGP in which the states existed. This is illustrated in Fig. 2.4. Therefore, the quarkonia suppression acts both as the indicator of the presence of the deconfinement and as the thermometer for the created matter.

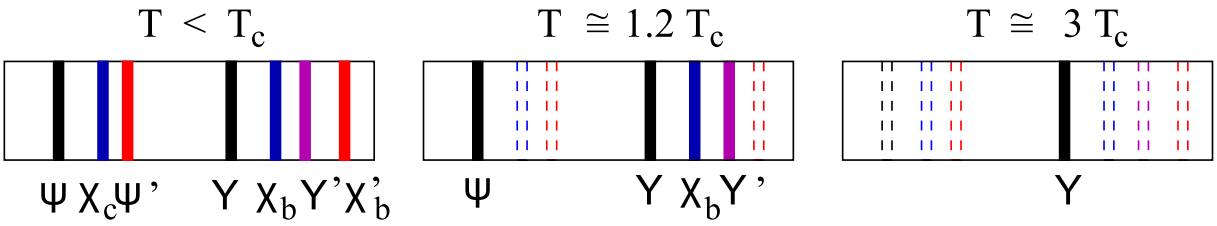

Figure 2.4: Diagram illustrating use the of quarkonia states as a QGP thermometer. Various quarkonia states disappear for systems with higher initial QGP temperatures. Figure from [30].

The picture sketched in previous paragraph is very alluring, but it is oversimplified. The

bound state is often modeled with the Cornell potential

$$V(r) = \sigma r - \frac{\alpha}{r}, \tag{2.1}$$

where r is the radial distance between the quarks, σ the strength of the linear confining part, and α is the strength of the Coulomb-like term [31]. The Debye screening is modeled as a modification to the potential by weakening the linear part. Various other models existed, however, modifications to purely-real potentials cannot fully describe the actual in-medium potential [32]. Instead, the potential develops an imaginary part in the following manner: The Wilson loop [33] in quantum field theory obeys

$$i\partial_t W_\square(r,t) = \Sigma(r,t) W_\square(r,t), \tag{2.2}$$

where $W_\square(r,t)$ is the Wilson loop, and $\Sigma(r,t)$ is a complex function that is, in the limit as $t \to \infty$, identified with the quarkonium potential. We thus obtain

$$V(r) = \lim_{t\to\infty} \frac{i\partial_t W_\square(r,t)}{W_\square(r,t)} \ . \tag{2.3}$$

Equation (2.3) is the basis for the calculation of the quarkonium potential, either in hard-thermal-loop perturbative calculations [34, 35] or using lattice QCD. The main challenge for the lattice calculations is that $W_\square(r,t)$ needs to be evaluated in real Minkowski time, as opposed to Euclidean time often used in lattice calculations [36]. The imaginary part of the potential is interpreted as the contribution of scattering and absorption of gluons from the medium. Figure 2.5 shows the results of lattice calculations for various temperatures, denoted by different colors. The left panel displays the real part of the potential, and the right panel shows the imaginary part. The results are staggered vertically in the left plot, and horizontally in the right, to avoid overlap. Note that the long range confinement portion of real potential gets weaker with increasing temperature (the slope at larger r diminishes). This is consistent with the original picture of modifications to the Cornell potential (Eq. (2.1)).

The imaginary part on the right panel increases with increasing temperature, signifying the growing contribution from scattering and absorption. The lattice calculation is compared with the results of hard-thermal-loop calculations, plotted as solid lines.

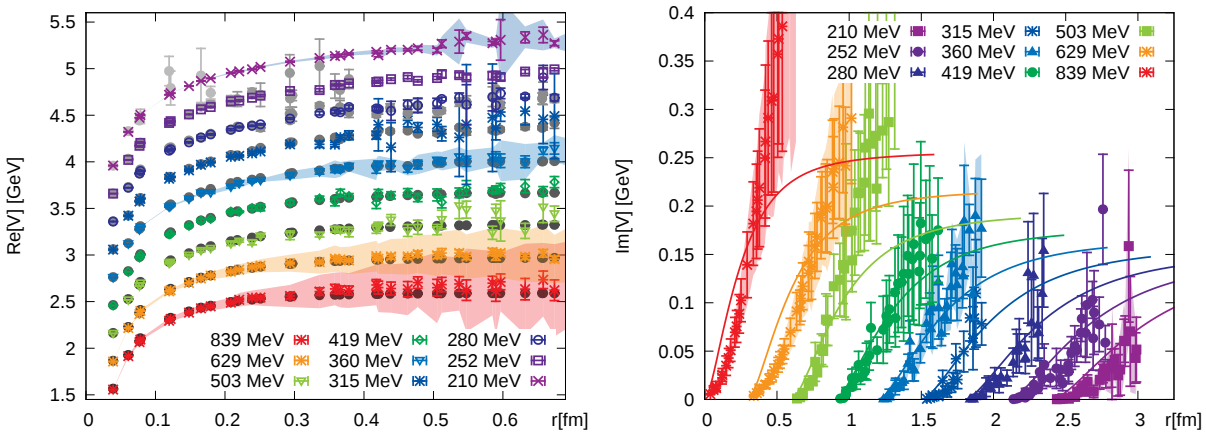

Figure 2.5: **Left:** Real part of the quarkonium potential for various temperatures as calculated by lattice QCD. More details are provided in the text. **Right:** Imaginary part of the quarkonium potential. The solid lines are calculations from hard-thermal-loops for comparison. Figure from [37].

The other important part of the logic is that quarkonia states are heavy. The typical mass for charmonium states is 3–4 GeV (see Tab. 2.1 and Fig. 2.3). For bottomonia, the mass ranges from 9–11 GeV. This is due to the heavy mass of the constituent quarks, $m_c = 1.27\,\text{GeV}$ and $m_b = 4.18\,\text{GeV}$ [29]. These masses are much higher than the typical temperature of the QGP, which is in the hundreds of MeV (see Fig. 2.2). Thus, the heavy quarks are primarily produced in the initial parton hard scattering, during the early stages of the collision. Their thermal production is heavily suppressed by a factor of $\exp(-m/T)$, and very little charm and almost no bottom is created thermally, in later stages. This is important because thermal production in late stages would mask the temperature-related dissolution. Instead, quarkonia are created on the same or shorter timescale than that of the QGP formation and thus carry information about the QGP.

The high mass of c and b quarks provides another important advantage. The mass is much higher than the typical QCD scale of $\Lambda \approx 200\,\text{MeV}$. Therefore, the strong force coupling, which decreases with increasing energy, is small at the corresponding mass scale, and quarkonia production is calculable in the perturbative expansion.

2.3.2.1 Production models

There are several models describing quarkonia production. The models that are most commonly employed in the calculations are:

- **Color Singlet Model (CSM):** A quark pair is created in the initial hard scattering with the same quantum numbers as the resulting quarkonium [38]. The model struggles to describe several measured observables, e.g. p_{T} spectrum at Tevatron [39].
- **Non-Relativistic QCD (NRQCD):** The NRQCD model incorporates both color singlet and color octet production in an effective field theory treatment [40, 41]. The model describes the yields well but is challenged to describe the polarization of quarkonia states.
- **Color Evaporation Model (CEM):** The charmonium is produced as a $c\bar{c}$ pair with an invariant mass below the $D\overline{D}$ threshold. The $c\bar{c}$ pair then radiates soft gluons to create the final charmonium state [42, 43]. In its straightforward form, the model expects the ratio of cross sections for various charmonium states to be independent of kinematics as well as of production process, which is in disagreement with data. To address this issue, an improved CEM model (ICEM) has been proposed [44].

2.3.2.2 Baseline for measurements

In order to determine if the state has dissolved or not, we need to know their production in the absence of the QGP. Then, we can compare the observed yields with yields in presence

of the QGP. Such a baseline measurement is provided by $p+p$ collisions. The $p+p$ system is relatively simple, and too small for creating the QGP[2]. Measurements are ideally performed at the same energy and with the same detector as the heavy-ion measurements in order to eliminate potential biases.

The observed yields need to be properly scaled. To a first approximation, a heavy-ion collision can be viewed as a collection of hundreds or thousands of individual nucleon-nucleon collisions happening in a single event. Such a collision naturally creates more particles than a single nucleon-nucleon $p + p$ collision. The scaling is calculated in the framework of the Glauber model [47, 48], with the nucleon-nucleon interactions assumed to be independent. The production of heavy-quarkonia is limited to the initial hard parton-parton scattering, which is directly proportional to the number of individual nucleon-nucleon collisions, labeled as $N_{\rm coll}$. The $N_{\rm coll}$ depends on the details of the collision. The $A + A$ collisions can happen head-on, with $N_{\rm coll} \approx 2000$ for fully head-on "central" $\mathrm{Pb} + \mathrm{Pb}$ collision. At the other extreme, it is possible to have a glancing impact with $N_{\rm coll} = 1$. The range of $N_{\rm coll}$ in $p + \mathrm{Pb}$ collisions is smaller, cca. 1-14 [49].

Particle production from the Glauber model is related to observables that can be measured experimentally. Commonly used variables include track multiplicity $N_{\rm tracks}$, and the energy deposited in the calorimeters. In this fashion, the yield in $A + A$ collisions can be scaled and compared to the $p + p$ yields. Results of the Glauber model calculations are validated in measurements where QGP is expected to play a negligible role, and thus the yields are expected to scale exactly (when accounting for the other known non-QGP effects). Such a test includes measuring the Z [50–52] or W [53, 54] bosons.

[2]At least in the vast majority of interactions. There is evidence of collective behavior in the highest activity events, both for $p + \mathrm{Pb}$ and $p + p$, which could be interpreted as presence of the QGP [45, 46].

2.3.2.3 Complications

Reality is much more complicated than the simple and straightforward picture of quarkonia as a thermometer outlined in the previous paragraphs. The image is obfuscated by many additional effects, which have been discovered or considered since the initial idea was proposed. A non-exhaustive overview of the most important effects is provided here:

- B **meson decays:** The B meson, a bound state of a b quark and a light quark, can decay to J/ψ and other charmonia states. These *non-prompt* charmonia do not carry the same information as the *prompt* ones, because the B mesons are affected by the QGP differently. The non-prompt contribution can be removed if the detector allows for precise vertexing. The lifetime of B mesons, $c\tau$, is on the order of 500 µm [29], which is far enough from the original interaction point to be separated.

- **Feed down and sequential melting:** A large fraction of the lower-energy quarkonia states is created via decays from higher-energy states. This so called *feed-down* happens very quickly and cannot be distinguished from the *direct* production and both sources are included in the prompt charmonia. Feed-down complicates the situation, because a lower-energy state will be suppressed already at temperature where it does not dissociate. This is because the higher state did dissociate, and, therefore, the feed-down portion of the lower-energy state disappeared [55]. The exact dissociation temperatures depend on the calculation, but the general order of dissociation temperatures for charmonia is T_d is $T_d(J/\psi) > T_d(\chi_c) \gtrapprox T_d(\psi(2\mathrm{S}))$. Therefore, we expect some J/ψ suppression already at a lower $T_d(\psi(2\mathrm{S}))$ or $T_d(\chi_c)$ because of the missing feed-down.

- **Statistical hadronization:** Statistical hadronization is an effect that should play a much larger role for charmonia than for bottomonia. As noted earlier, the charmonium

states are heavy and do not get created thermally. However, there are other free c quarks present in the QGP, created in unrelated initial parton-parton interactions. After the charmonium dissolved, its c and $\bar{c}$ quarks are still present in the QGP. At the hadronization phase, they can recombine with other c quarks to create a new charmonium. This can happen either with the unrelated c quarks at hadronization [56, 57], or dynamically, where the charmonium is destroyed and formed while passing through the medium [58]. Statistical hadronization predicts the relative enhancement of charmonia production, especially for central events and low-p_{T} charmonia [59]. The bottomonia are less affected because the b quarks are significantly scarcer, even at LHC energies. Sometimes *recombination* and *regeneration* are used as names for this effect.

- **Cold nuclear matter (CNM) effects:** These are effects that are unrelated to the QGP, but instead originate from the presence of the heavy nucleus in the collision. This modifies the quarkonia production, in comparison to a $p + p$ collision, beyond simple N_{coll} scaling. These effects are crucial for this analysis and are explored in more detail in the following section.

2.4 Cold nuclear matter effects

The main goal of this analysis is to probe cold nuclear matter (CNM) effects using $p + \mathrm{Pb}$ collisions, especially their impact on the charmonia P and S states. The CNM effects can be broadly divided into two major categories. The *initial-state* effects are those that are caused by a presence of a heavy-ion directly, without influence of the collision. They are modifications to the quarkonia production in the initial hard scattering. From the initial state effects we will discuss the *modifications to the nuclear parton distribution functions* (nPDF). On the other hand, *final-state* effects are those that affect the state after it was

formed. After the quarkonium state has been created, it streams from the initial scattering, but there are other particles present in its vicinity. These can interact with the quarkonium and dissolve it. Two effects are discussed: *comovers* and *nuclear absorption*. We also discuss *coherent energy loss*, a mechanism that is not easily categorized as either an initial- or a final-state effect.

2.4.1 Modifications to the nPDFs

As the collision energy increases, we probe smaller scales ($\lambda = h/p$). At high collision energies, the nucleons do not interact with each other directly. Rather, interactions happen between individual quarks and gluons, which, together, are called partons. The distributions of partons inside a nucleus can be plotted as a function of x, where x is the fraction of momentum of the whole nucleon that is carried by the parton, $x = p_{\text{parton}}/p_{\text{nucleon}}$, in the infinite momentum frame. This is almost universally done for protons, because they are charged, and, thus, they can be accelerated and it is much easier to set up their collisions. There are many fewer data for neutrons, but due to isospin symmetry, their parton distribution functions (PDFs) are expected to be the same as protons with exchange of $u \leftrightarrow d$. Examples of PDFs are shown in Fig. 2.6. The momentum fraction x is on the x-axis. The y-axis shows the value of the distribution function multiplied by x. The left plot shows the PDFs for different proton constituents. The proton valence quarks u_v and d_v are most prominent at large x, with u_v twice as large as u_d, corresponding to the traditional quark content of uud for proton. However, when we move towards lower values of x, we start to see the *sea* quarks, and, prominently, gluons. Gluons are so dominant at low-x values that they are divided by 10 to fit the plot.

The exact shape of the curves is obtained from theoretical fits to data, and is thus model dependent. The right panel shows the gluon PDF for various models. The y-axis

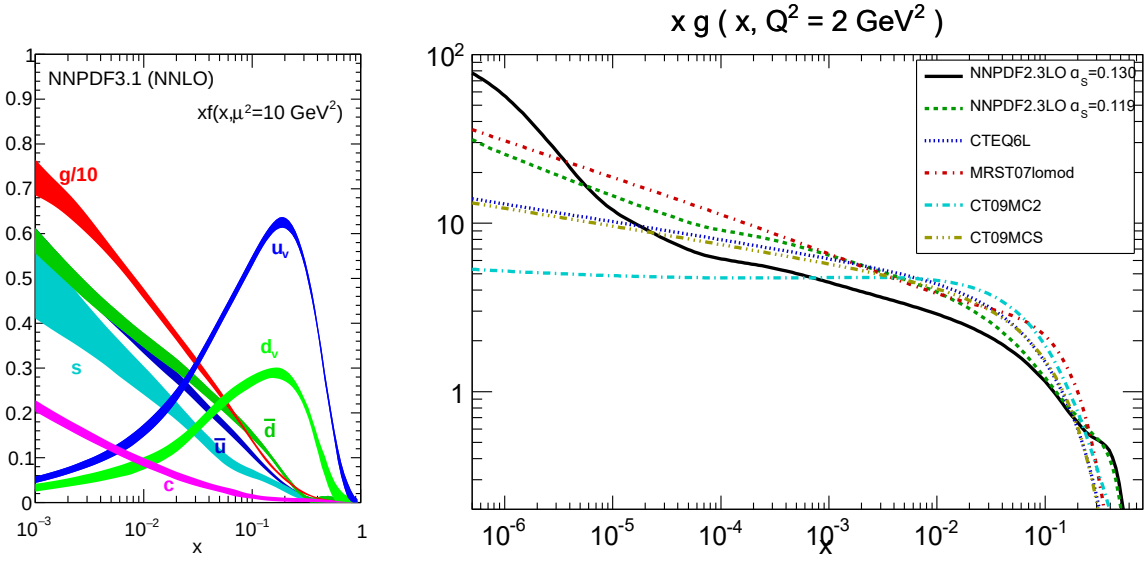

Figure 2.6: **Left:** Example PDFs for protons. The panel shows the updated NNPDF3.1. Figure from [60]. **Right:** Diagram showing various PDFs for gluons on a log-log scale. The most relevant PDF is the "NNPDF2.3LO, $\alpha_s = 0.130$". It is the PDF that is used for the simulated samples for this analysis via the PYTHIA8 CUETP8M1 tune. Figure from [61].

is logarithmic. The black line is the NNPDF2.3LO PDF, which is used by the PYTHIA8 CUETP8M1 tune in the Monte Carlo samples that we used in this work. See Section 4.2 for details of the Monte Carlo settings.

The shape of the PDFs also depends on Q^2, where Q is the momentum transfer in the interaction between the partons. Therefore, the curves shown in Fig. 2.6 need to specify the Q^2 at which they are plotted. The relevant scale for the χ_c production with mass $m \approx 3.5\,\text{GeV}$ is around $Q^2 = 10\,\text{GeV}^2$. The PDFs can be evolved to different values of Q^2 via DGLAP equations, named after the discoverers Dokshitzer, Gribov, Lipatov, Altarelli, and Parisi [62–64].

PDFs in the Pb nucleus

Heavy ions are not simple collections of independent nucleons as outlined in Section 2.3.2.2. Instead, the nuclear PDFs are modified relative to their proton counterparts. The modification is usually expressed as the ratio to the proton PDF as a function of x, with a value of 1 meaning that the PDF is the same as in the proton. Examples of modifications are plotted in Fig. 2.7.

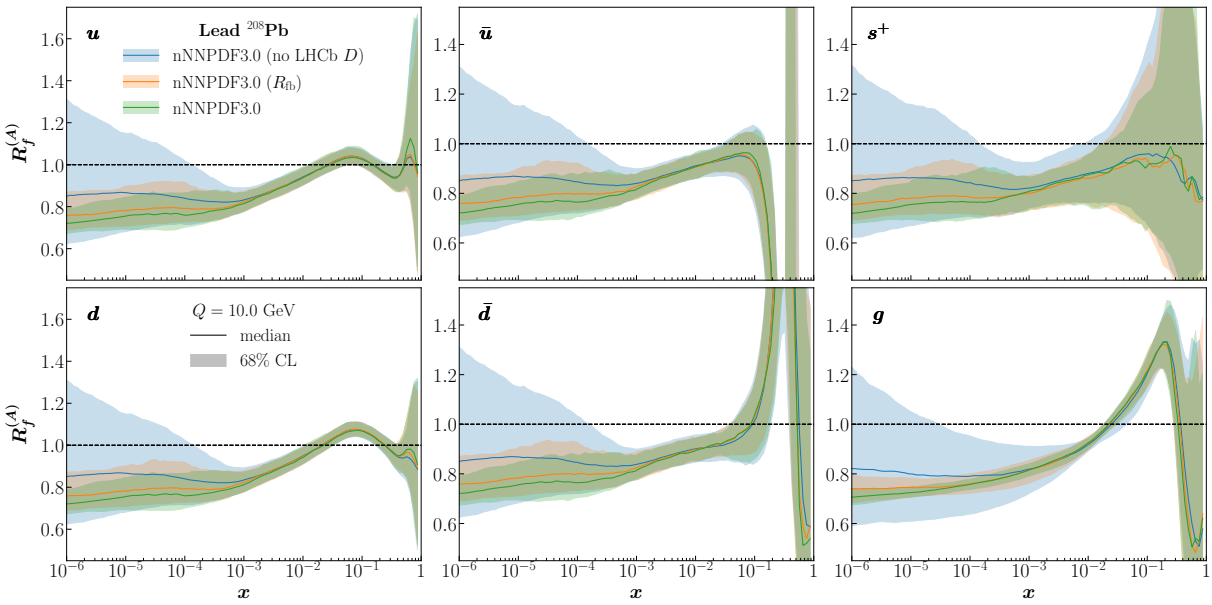

Figure 2.7: Modifications to three example PDFs for Pb nucleus, at $Q = 10\,\text{GeV}$. The six panels show a modification to a different quark or gluon. Figure from [65].

Because particle production depends on the exact PDF, the modification changes the particle yields in Pb + Pb and p + Pb collisions without any QGP related effects. The most important curve is the gluon panel in the bottom right of Fig. 2.7, because quarkonia production at the LHC is dominated by gluon fusion. For midrapidity, we are in the region of *shadowing*, with $x < 10^{-2}$, where the gluon PDFs are suppressed in Pb with respect to p. This suppression of the nPDF translates to lower quarkonia production, which should not

be dependent on event activity.

Our analysis is relatively insensitive to the influence of nPDFs, because production of the charmonium states (including χ_c and J/ψ) is affected in the same way. While the differences in the masses lead to sampling slightly different values of x for the PDFs, the impact is very small. Therefore, any nPDF-related effects cancel out in the ratio. The PYTHIA8 Monte Carlo simulation used in this work is based on a proton PDF, as are all the other quarkonia simulations done within the dilepton CMS group for this data sample. The modifications affect primarily the overall cross sections and kinematics of the produced χ_c. Neither is a concern for the simulation, as the cross section is irrelevant for the efficiency studies for which the simulation is used, and the kinematic distributions depend on other parameters and are weighted to match the data (see Section 4.3 for details).

2.4.2 Comovers

The comover interaction model (CIM) [66, 67] describes the quarkonia suppression in $p+\mathrm{Pb}$ collisions. In this model the suppression is caused by a final-state scattering with other particles created in the collision that travel in the same rapidity region as the quarkonium. The different quarkonia states have different binding energies, which explains the difference in the observed suppression. The higher energy states are more loosely bound with a larger average radii than the ground states, leading to a higher effective cross section for their break-up. Another model that uses a similar approach for the final state interaction is the *transport* model, which has been adapted for $p+\mathrm{Pb}$ collisions [68].

2.4.3 Nuclear absorption

At lower collision energies ($\approx 10-100\,\mathrm{GeV}$), the quarkonia formation time is similar to the nuclear size. The quarkonia states can be destroyed by scattering with the passing nuclear

remnant. This is quantified by an effective absorption cross section σ_{abs}. The model describes the low $\sqrt{s_{_{NN}}}$ data well [69].

Nuclear absorption is expected to play a limited role at LHC collision energies, where the relativistic boost is much larger, and the quarkonia do not form on the same time scale as its passage through the nucleus.

2.4.4 Coherent parton energy loss

A model based on coherent energy loss in nuclear matter, considering medium-induced radiation from the interference between the initial and final state emission amplitudes [70], has been developed for $p + \text{Pb}$ collisions [71, 72] and later extended to $\text{Pb} + \text{Pb}$ collisions [73]. When an outgoing parton or $c\overline{c}$ pair is produced at a small angle in the target rest frame (i.e. p_{T}/E is small), there is interference between the initial and final state radiation of gluons, which dominates the medium-induced gluon spectrum. Such an effect is expected to be more pronounced in the forward rapidity region. In $\text{Pb} + \text{Pb}$ collisions, the model describes the J/ψ suppression in peripheral events, but it cannot describe the central events. This is consistent with the picture of additional suppression due to the presence of the QGP.

2.5 Overview of relevant experimental results

2.5.1 χ_c in $p + p$ collisions

The χ_c states have been measured in $p + p$ collisions by several experiments. The χ_c-to-J/ψ ratio has been measured by the LHCb experiment at $\sqrt{s} = 7\,\text{TeV}$ [74]. The results are shown in Fig. 2.8. The LHCb measurement is in forward rapidity, $2 < y_{\text{lab}}(J/\psi) < 4.5$, and with transverse momentum $2 < p_{\text{T}}(J/\psi) < 15\,\text{GeV}$. In the left panel, the LHCb results are compared to the CDF measurement from $p + \overline{p}$ collisions at $\sqrt{s} = 1.8\,\text{TeV}$ [39]. The right

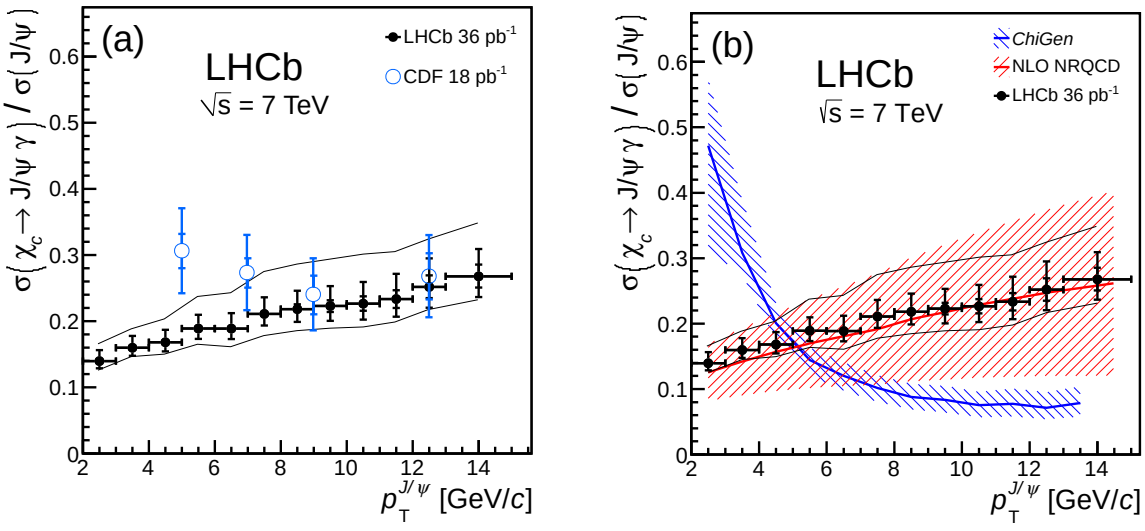

Figure 2.8: The χ_c-to-J/ψ ratio in $p+p$ collisions. Black points are the LHCb results, and blue points are the results from the CDF experiment. Two models are shown in the right panel. Blue is the prediction from ChiGen, and red is the NLO NRQCD result. Figure from [74].

panel compares the results with the ChiGen Monte Carlo generator prediction [75], which does not describe the data well, and to the next-to leading order non-relativistic QCD (NLO NRQCD) calculation [76], which is in agreement.

To explore the models, we also look at the χ_{c2}-to-χ_{c1} ratio ratio. LHCb measured the ratio using the same setup as in Fig. 2.8 [77]. The results are displayed in Fig. 2.9, with the comparison to CDF data at midrapidity $|y| < 1.0$ at $\sqrt{s} = 1.96\,\text{TeV}$ [78]. The results are compared to the same models as in Fig. 2.8. Neither model describes the ratio very well, but the ChiGen captures the general shape better. However, the ChiGen failed to describe the ratio shown in Fig. 2.8.

The χ_{c2}-to-χ_{c1} ratio has been measured at the LHC at $\sqrt{s} = 7\,\text{TeV}$ by the ATLAS [79] and the CMS [80] experiments as well. The results are plotted in Fig. 2.10. The left panel shows the ratio measured by the ATLAS collaboration in black points, and the right panel shows

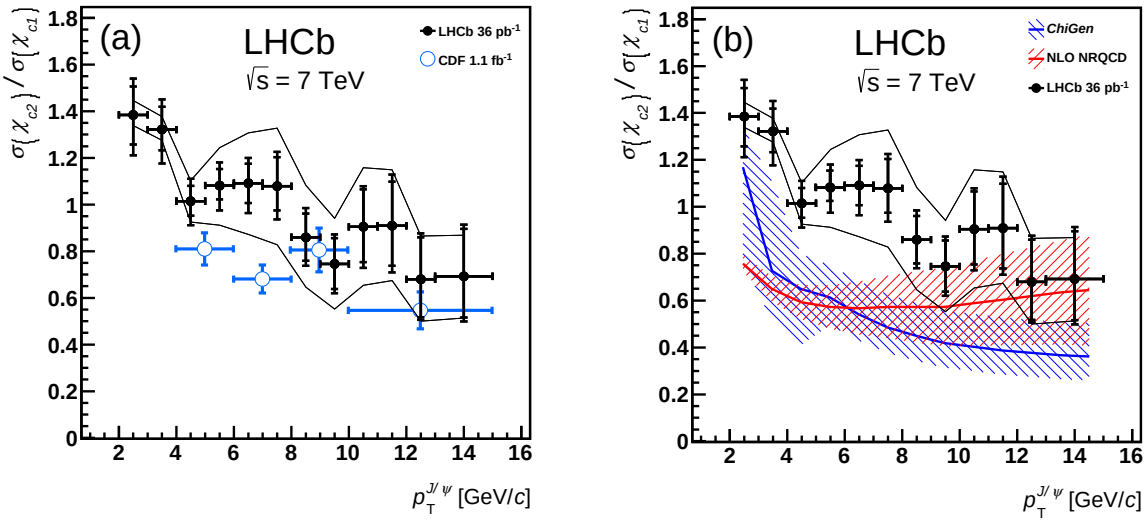

Figure 2.9: The χ_{c2}-to-χ_{c1} ratio including the branching ratios as measured in $p+p$ collisions. Black points are the LHCb results, and blue points are the results from the CDF experiment. The blue curve on the right plot is from ChiGen, and the red is from NLO NRQCD. Figure from [74].

the measurement by CMS. Both data sets assume non-polarized, isotropic decay of χ_c. The rapidity is $|y_{\rm lab}(J/\psi)| < 0.75$ for ATLAS and $|y_{\rm lab}(J/\psi)| < 1$ for the CMS measurement. The right plot shows the effect of two extreme polarization scenarios in Collins-Soper frame as dashed green ($(m_{\chi_{c1}}, m_{\chi_{c2}}) = (0,0)$), and blue lines ($(m_{\chi_{c1}}, m_{\chi_{c2}}) = (\pm 1, \pm 2)$). The NRQCD calculation [76] is included in both plots. The data are within the NRQCD uncertainties, but the overall trend is not quite the same, as the NRQCD raises with increasing $p_{\rm T}$ more than data. The left plot additionally displays leading-order CSM calculation from ChiGen, which misses the data.

The ATLAS measurement also includes the χ_c-to-J/ψ ratio at midrapidity, shown in Fig. 2.11. The results are compared to the LHCb measurement that was reported in Fig. 2.8 and to the NRQCD calculation. The ATLAS has similar $p_{\rm T}$ and rapidity range as our measurement.

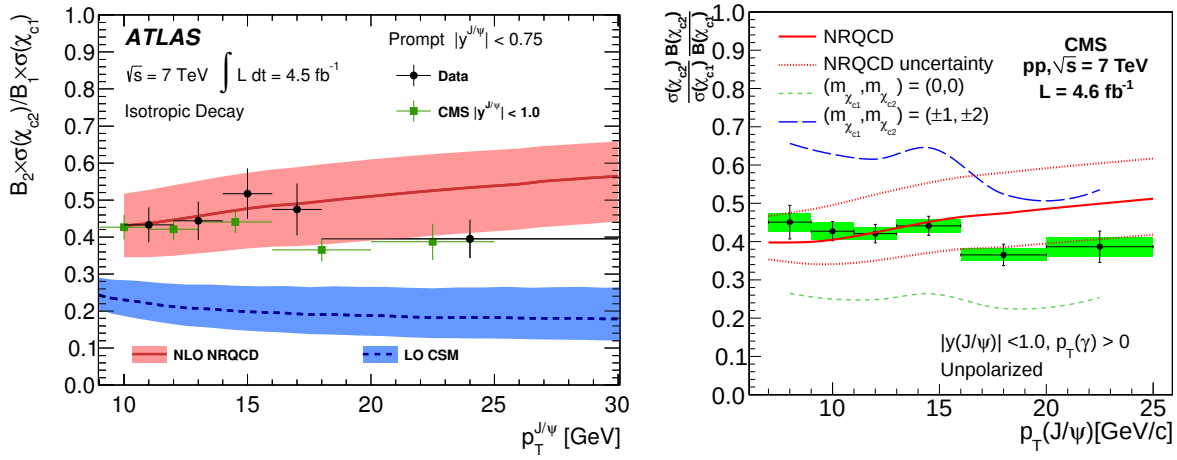

Figure 2.10: The χ_{c2}-to-χ_{c1} ratio in p+p collisions at $\sqrt{s} = 7$ TeV assuming non-polarized χ_c. Details are given in the text. **Left:** Black points are the ATLAS results, green points are the results from the CMS experiment (same as the right plot, truncated). Figure from [79]. **Right:** CMS results. Figure from [80].

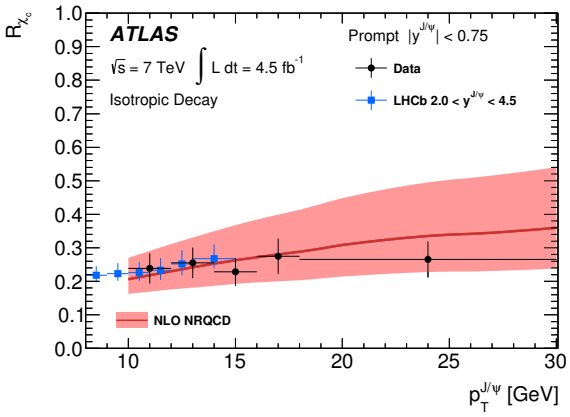

Figure 2.11: The χ_c-to-J/ψ ratio measured by ATLAS shown with black points, compared with the LHCb results in forward rapidity (blue). Figure from [79].

2.5.2 χ_c in $p + A$ collisions

There are limited data on the χ_c states in heavy-ion systems, especially at energies where the QGP is expected to form in $A+A$ collisions, and where $p + A$ measurements could constrain

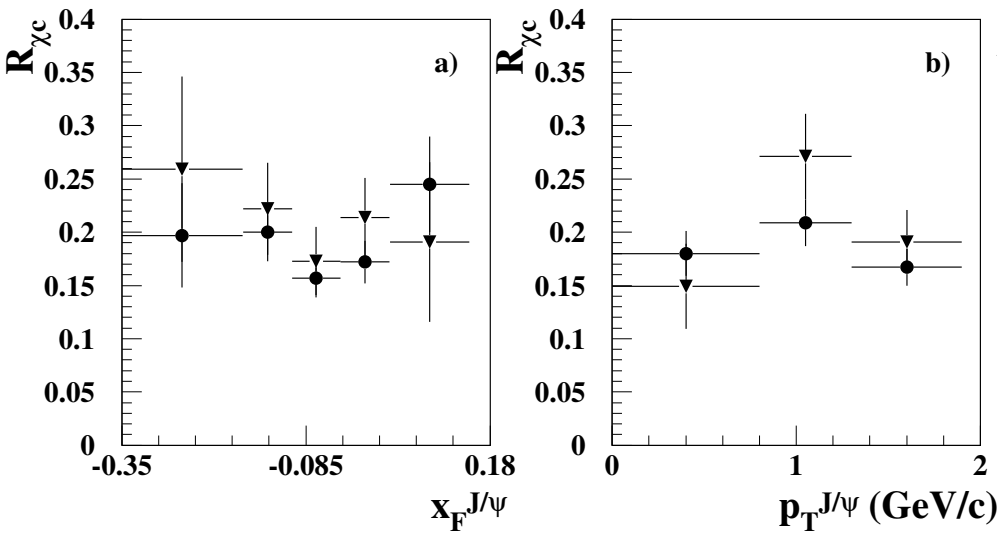

Figure 2.12: The χ_c-to-J/ψ ratio measured by the HERA experiment as a function of $x_F(J/\psi)$ (left) and $p_{\mathrm{T}}(J/\psi)$ (right). Triangles are from p + W, circles p + C. Figure from [81].

the related CNM effects. Figure 2.12 shows the results of a measurement performed at HERA [81], at relatively low energy $\sqrt{s_{_{NN}}} = 0.0416\,\mathrm{TeV}$. The left panel shows the χ_c-to-J/ψ ratio as a function of x_F, where x_F is the Feynman variable expressed in the nucleon-nucleon center-of-mass system, $x_F = p_{\parallel}/p_{\mathrm{max}}$, where $p_{\parallel}$ is the longitudinal momentum and p_{max} is the maximum momentum that the particle could have. The right panel shows the ratio as a function of $p_{\mathrm{T}}(J/\psi)$. The triangles show the p + W measurement, and the circles display p + C results. The measurement has large uncertainties, but it is still clear that going from C ($A = 12$) to W ($A = 184$) does not introduce any major differences.

At the LHC, the χ_c has been measured by LHCb at $\sqrt{s_{_{NN}}} = 8.16\,\mathrm{TeV}$ using data from the same run as this work. The reported quantity is the χ_{c2}-to-χ_{c1} ratio divided by the branching ratios [82]. The result is plotted in Fig. 2.13. LHCb used two strategies to measure the γ from the χ_c decay: *(i)* via the conversion to an $e^+\,e^-$ pair, and *(ii)* measuring the photon in the calorimeter. These are shown in the figure in red and blue, respectively. The yellow

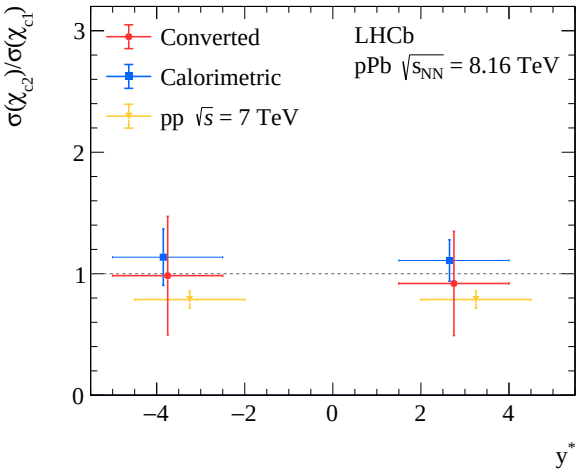

Figure 2.13: The χ_{c2}-to-χ_{c1} ratio at LHCb for forward and backward rapidity y_{CM} regions. Figure from [82].

points are from $p+p$ collisions measured by LHCb [83]. Within the large uncertainties, there are no significant differences between the ratio at forward and backward rapidities in $p+\mathrm{Pb}$, and between $p+p$ and $p+\mathrm{Pb}$ results.

2.5.3 Other charmonium measurements

In this section, we introduce select measurements of other quarkonia that directly shed light on effects pertinent to the χ_c states. Most important are the results from $\psi(2\mathrm{S})$ measurements, because $\psi(2\mathrm{S})$ is another charmonium excited state, which can help disentangle the effects related to the lower binding energy and larger size of the excited states from orbital-momentum dependent effects.

One option for studying the effect interplay is to investigate the N_{coll} dependence. The existing measurement at PHENIX in $d+\mathrm{Au}$ collisions at $\sqrt{s_{NN}} = 0.2\,\mathrm{TeV}$ is shown in Fig. 2.14 on the left panel [84]. The panel shows the ratio of production in $d+\mathrm{Au}$ collisions divided by the properly scaled production in $p+p$ collisions. Blue points show the J/ψ

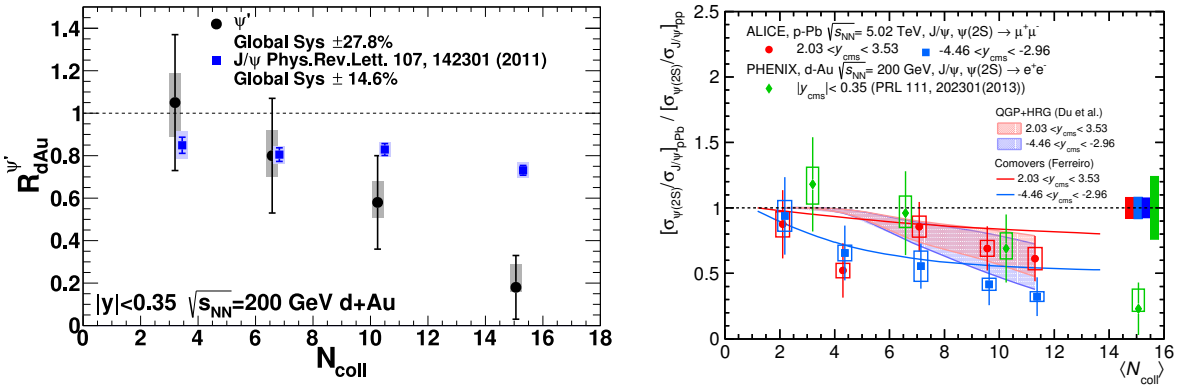

Figure 2.14: **Left:** The ratio of production at $d+\text{Au}$ collisions to $p+p$ collisions for $\psi(2\text{S})$ and for J/ψ, as measured by the PHENIX collaboration [84]. **Right:** The double ratio measured by PHENIX and ALICE [85]. Details are given in the text.

results, and the black points are the $\psi(2\text{S})$. The uncertainties for $\psi(2\text{S})$ are large, however there is a difference between the ground and excited states. This can be quantified as *double ratio*, DR, which divides the ratio for the excited state by the ratio for the ground state:

$$DR = \frac{\sigma(\psi(2\text{S}))_{p\text{Pb}}/\sigma(\psi(2\text{S}))_{pp}}{\sigma(J/\psi)_{p\text{Pb}}/\sigma(J/\psi)_{pp}} \tag{2.4}$$

The DR is shown on the right panel using green points (i.e. the green points on the right panel are the black points from the left panel divided by the blue points). This is compared in the right panel with a measurement from ALICE at $\sqrt{s_{NN}} = 5.02\,\text{TeV}$ [85]. The red points are measured at $2.03 < y_{\text{CM}} < 3.53$, and the blue are measured at backward rapidity $-4.46 < y_{\text{CM}} < -2.96$. In all instances, the excited state becomes more suppressed than the ground state as the event activity increases. This is compared to the calculation from two models from the group of models discussed in Section 2.4.2. The bands are from the QGP+HRG model [86], and the lines are from the comover model [87]. Higher suppression in backward rapidity originates from a higher density of comovers in the Pb-going direction.

Figure 2.15 explores the rapidity dependence. On the left, the ratio of production in $p+\text{Pb}$ to $p+p$ is plotted for J/ψ (blue points) and $\psi(2\text{S})$ (red points). Predictions from

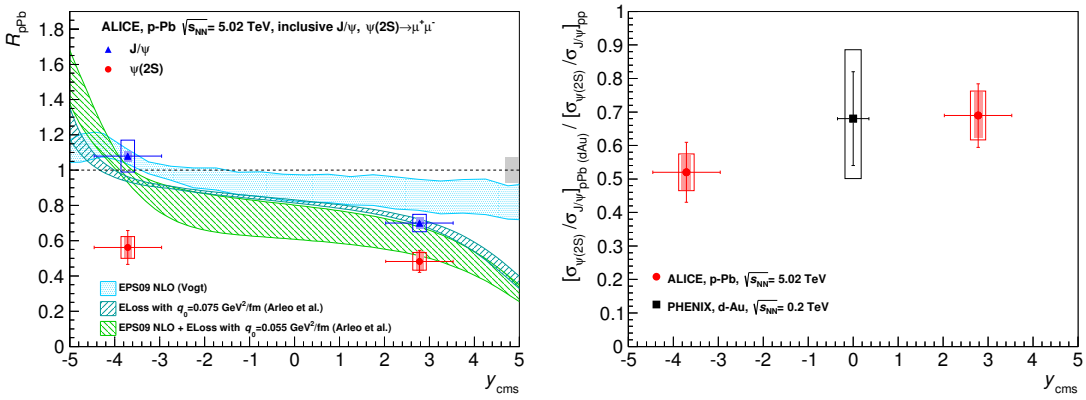

Figure 2.15: **Left:** The ratio of production at $p+\mathrm{Pb}$ collisions to $p+p$ collisions for $\psi(2\mathrm{S})$ and for J/ψ as a function of rapidity. **Right:** The double ratio measured by PHENIX and ALICE [88]. Details are given in the text. Figures from [88].

models including nuclear shadowing (discussed in Section 2.4.1) and coherent energy loss (Section 2.4.4) are shown. The right panel shows the double ratio for the ALICE result in red, with the integrated PHENIX result in black. The $\psi(2\mathrm{S})$ is more suppressed than J/ψ in both forward and backward rapidity, and there is not a strong rapidity trend.

These experimental results describe a picture where the excited state $\psi(2\mathrm{S})$ is more suppressed in $p+\mathrm{Pb}$ collisions than the ground state J/ψ, pointing to a presence of the final-state effects. A measurement of the χ_c states is then a natural next step to understand the quarkonia suppression mechanisms.

Chapter 3

Experimental facilities and techniques

3.1 LHC accelerator

The Large Hadron Collider (LHC) is the world's largest and most powerful accelerator. It spans the border between Switzerland and France, on the outskirts of the city of Geneva, and is a major part of the European Organization for Nuclear Research (CERN - Conseil Européen pour la Recherche Nucléaire). The purpose of the LHC is to accelerate charged particles (protons or heavy ions) to ultrarelativistic energies up to $E = 6.5\,\mathrm{TeV}$ for protons, and scaled by Z/A for ions.

The main part of the accelerator consists of a large underground ring, 27 km in circumference, that contains two beam pipes. In each beam pipe, an ultra-high vacuum (10^{-13} atm) is maintained, through which a particle beam is circulated around the ring. The beams are kept in circular, opposite-going trajectories using the dipole superconducting magnets with a field of $\approx 8\,\mathrm{T}$, which bend the charged particles of the beam via the Lorentz force $F = q(\vec{E} + \vec{v} \times \vec{B})$. The beam pipes are laid $\approx 20\,\mathrm{cm}$ apart in the horizontal plane, and, thus, one beam is always on the inside of the circle, and the other is on the outside. Along the ring, there are four points where the beams cross each other and, with the right timing,

collide. These points house four large experiments, which collect and analyze data from the collisions. The experiments are ALICE (A Large Ion Collider Experiment), ATLAS[1], LHCb (Large Hadron Collider beauty) and CMS (Compact Muon Solenoid). Figure 3.1 shows the aerial view of the area, and the schematic outline of the ring. The surface halls of the four LHC experiments are visible in the photograph. The ring itself and most of the actual experiments are underground. The photograph also shows the two main CERN sites, Meyrin and Prévessin.

Figure 3.1: The aerial view of the LHC accelerator and location of the four main experiments, as well as the main laboratory sites. The picture is taken from above the Jura mountains, facing southward towards Geneva and the Alps. Figure from [89].

[1]ATLAS formerly stood for "A Torroidal LHC ApparatuS", but the abbreviation is not used anymore.

The LHC additionally contains equipment to assist with the acceleration of the charged particles besides the bending dipole magnets. Because the dipole magnets are made of superconductors, they have to be kept at a very low temperature. The beam pipes and magnets are therefore cooled down to $-271.3\,^{\circ}\mathrm{C}$, which requires the world's largest cryogenic system. The beam focusing is performed by an ensemble of focusing magnets, primarily quadrupoles, but higher order magnets (sextupoles, octopoles, decapoles, etc.) are present as well. Their purpose is to keep the beam size small, because the natural tendency of a positively charged beam is to spread out due to the repulsive Coulomb force. Additionally, radiofrequency (RF) cavities are present along the beamlines. Their main purpose is to accelerate particles to a higher energy by passing them through a 400 MHz electromagnetic field. With the right timing, each cavity can add about 2 MeV per unit of charge in a single beam pass. There are a total of eight cavities along the ring (clustered together). Therefore, many millions of passes are needed to reach the final energy, in a process that takes about half an hour from the moment the beams enter the LHC. After the final energy has been reached, the RF cavities are used to maintain the energy, as the beam experiences bremsstrahlung losses due to its curved path.

3.1.1 Full accelerator chain

It is not possible to inject stationary particles directly into the main LHC ring. Rather, a minimum particle momentum is required. This is generally true for any large circular accelerator and it is not specific to the LHC. Therefore, a chain of smaller accelerators exists, each feeding a larger machine, until the sequence culminates with the LHC. Most of the smaller accelerators were not built specifically for the LHC, but they originated as final-accelerator-stage research machines, and only after years of service were repurposed as the feeders for a larger machine (while still maintaining active research). Figure 3.2 shows

the schematic of the current status of the accelerator complex. The relevant stages of the

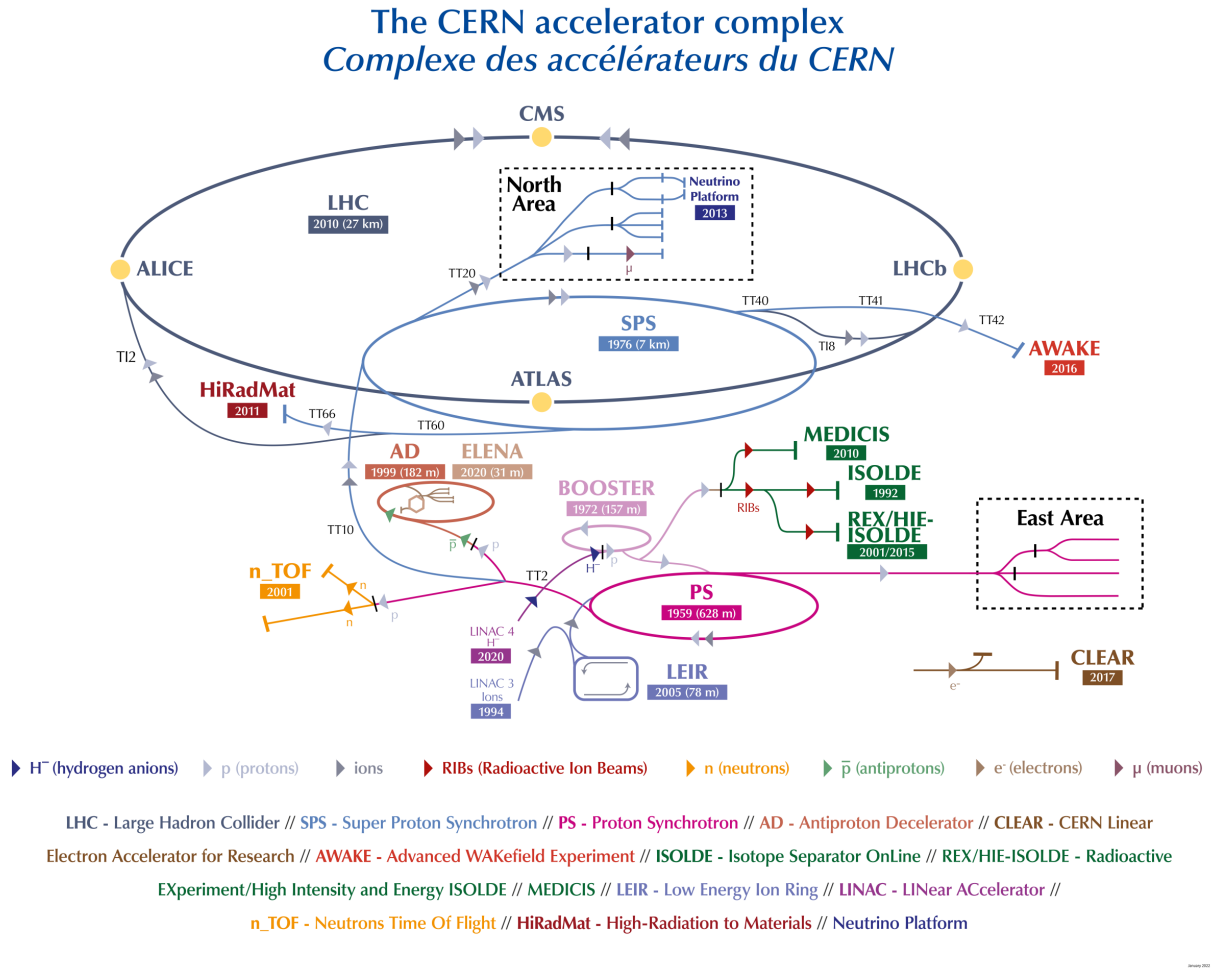

Figure 3.2: The schematic overview of the full accelerator complex at CERN. Relative sizes are not to scale. Figure from [90].

acceleration are as follows:

1. The accelerator chain starts in a linear accelerator (linac), which uses a single-path electric field to accelerate a charged particle. The specific machine differs for proton and ion beams:

a) Ion beams: The initial acceleration is performed by Linac 3. Not all electrons are stripped away at the source. The first step at the linac removes 29 electrons[2] in a microwave-heated plasma. Further electron removal is done in the next accelerating stages by passing the beam through a thin stripping foil. The full removal of the electrons from the ions is achieved only by the SPS (stage 4). The ions are accelerated to 4.5 MeV per nucleon by the time they exit Linac 3.

b) Proton beam: The initial linear accelerator used for our 2016 sample was Linac 2 (not shown), which accelerated protons to 50 MeV. Unlike ions, protons have only a single electron, which is trivial to remove. Linac 2 was replaced in 2020 with Linac 4, which is shown in the schematic.

2. A circular accelerator/storage ring performs the next step in the acceleration, which also differs between p and ion beams:

   a) Ion beams: LEIR (Low Energy Ion Ring) further accelerates the beam to about 70 MeV per nucleon, cools it (so it becomes denser), and strips more electrons.

   b) Proton beam: PSB (Proton Synchrotron Booster). The proton beam is accelerated to 1.4 GeV (until 2018, now upgraded to 2 GeV) before being passed onto the next stage.

3. PS (Proton Synchrotron) is the next step in the accelerator complex. This step, and the ones that follow, is performed by the same machine for protons and ions. The PS accelerates proton beam up to 26 GeV, the ion beam energy is proportionally smaller by a factor of Z/A. It also removes the last electrons from the heavy ions, so that all that remains is the nucleus.

[2]The exact number of electrons is somewhat random in each stage. Ions that have a different number of electrons are simply lost.

4. SPS (Super Proton Synchrotron) further accelerates beams to 177 GeV per nucleon for Pb beams (or 450 GeV for proton beams). The SPS ring is 7 km in circumference. It is the last accelerator before the beams are injected into the LHC. Besides serving as an injector for the LHC, the SPS delivers beams to many experiments in the Prévessin site, including those that are used in various detector studies for LHC experiments.

3.2 CMS detector

The CMS experiment is located in an underground cavern at one of the interaction points of the LHC (denoted as IP5 or just P5). The experiment consists of many different subdetectors [91], in an arrangement designed to detect a variety of particles across a wide range of rapidities and p_{T}. Figure 3.3 shows the schematic drawing of the CMS components. In the center of the detector, closest to the interaction point (IP), there is a silicon tracker (described in detail in Section 3.2.2). Outside of the tracker, there is an electromagnetic calorimeter (ECAL) and hadron calorimeter (HCAL). These are described in Section 3.2.3. Moving further away from the IP, we encounter the superconducting solenoid. The magnet creates a 3.8 T magnetic field inside its volume, that is roughly uniform and parallel to the beam line. The purpose of the field is to bend charged particles via the Lorentz force, which allows us to use the measured curvature of the track to calculate the charged particle momentum from $p_{\mathrm{T}}/q = Br$ where B is the magnetic field, q is the particle charge (assumed to be $|1e|$, with a sign given by the direction of track curvature), and r is the radius of the track projected onto a plane perpendicular to the field. The magnetic field outside of the solenoid is modulated by the return yoke, a large metal structure designed to adjust the magnetic field outside of the solenoid in such a way that it is uniform and parallel to the beam line, with about half the strength compared to the field inside the solenoid. The outside field provides another opportunity to measure the particle momentum. The yoke weighs 13 000 t and is the heaviest

portion of the detector. It also serves as a support structure for the experiment. Interspersed in the yoke are muon detection chambers described in detail in Section 3.2.4.

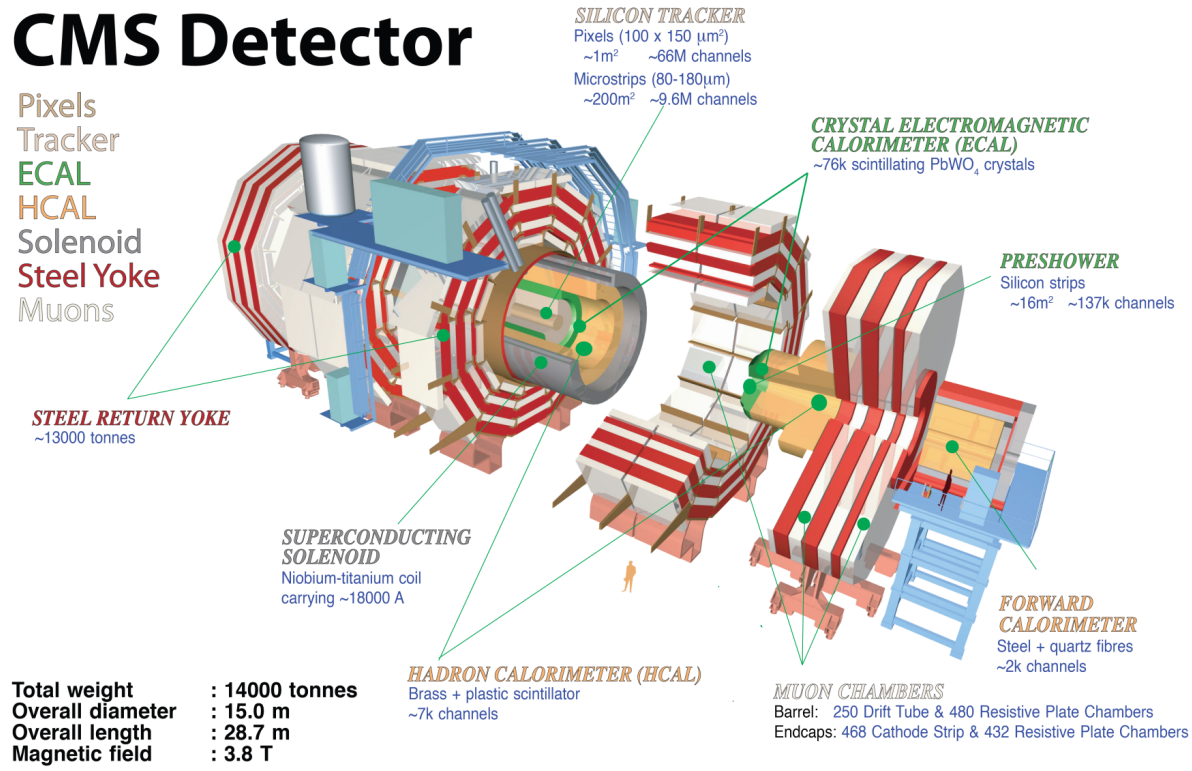

Figure 3.3: The diagram of the CMS experiment showing its components. Details are in the text. Figure from [92].

The experiment measures $\approx 30\,\text{m} \times 15\,\text{m} \times 15\,\text{m}$. To get a sense of scale, a human figure is included in the diagram in Fig. 3.3, and a photograph of the experiment is provided in Fig. 3.4. The gangways in the background of the photograph are about 2.5 m tall. The beamline is visible in the center of the picture. Beams travel left to right (and vice-versa), and the nominal IP is located in the middle of the left-hand side portion of the detector. Various detector components are visible. Their locations and descriptions are referenced in

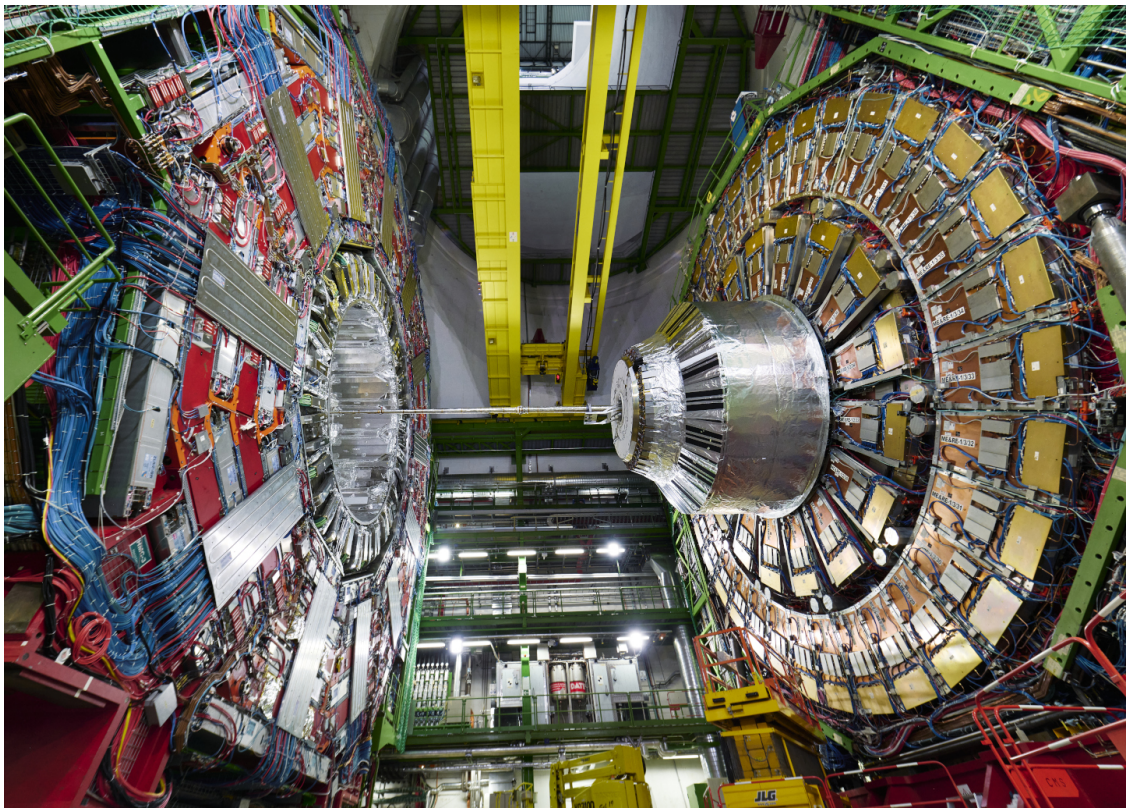

Figure 3.4: A photograph of the CMS experiment. The experiment is photographed while open and being worked on. The two halves close and fit snugly during the operation. For sense of scale, note the gangways in the middle of the picture.

their respective sections.

The CMS subdetectors are designed to complement each other, and, together, they accomplish robust particle detection and identification. The schematic diagram of the experiment is presented in Fig. 3.5. The diagram shows a slice of the CMS experiment, viewed in the plane perpendicular to the beam, with beams pointing into and out of the page. The IP is on the left side, in the center of the circles where the tracks originate. Interactions of various particle species in different systems can be used to distinguish the species:

- **Muon:** shown in the plot in cyan. Muons, similar to all charged particles, leave a signal in the silicon tracker. They leave very little signal in the calorimeters, and

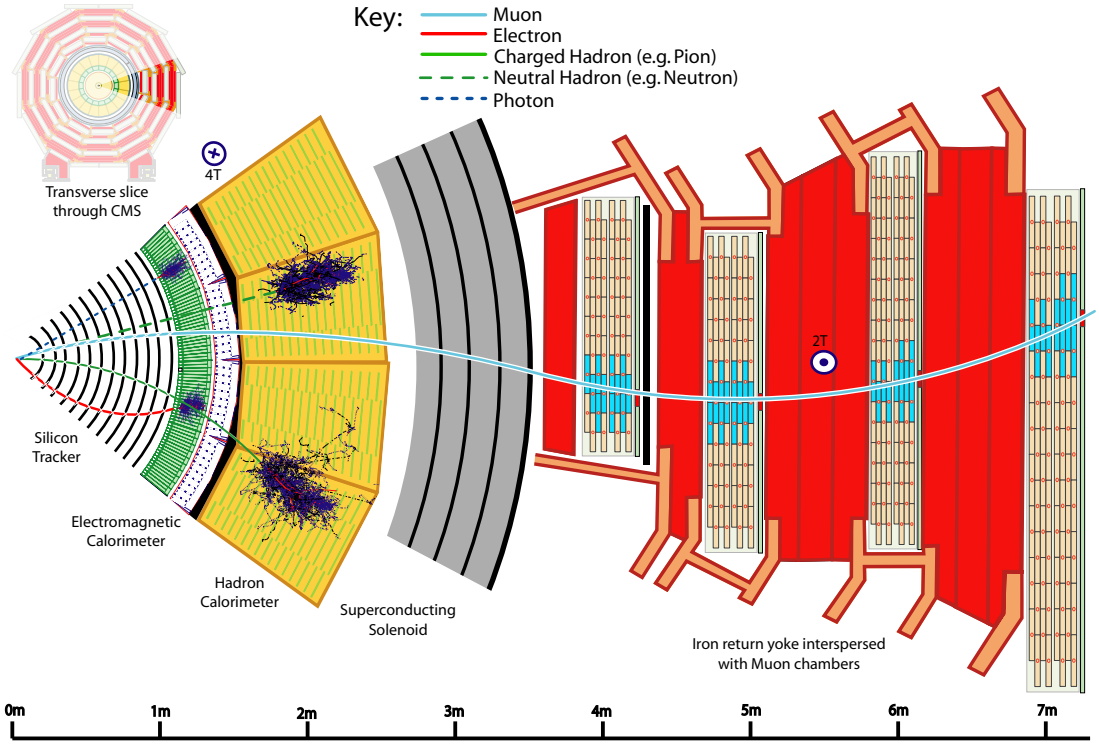

Figure 3.5: The cross-sectional schema of the CMS experiment. Idealized tracks from different particle species are shown with indications of the signals left by particles in relevant subdetectors. Figure from [92].

they pass through the solenoid to the muon chambers, where they leave a signal on their way through. The muon penetrability is its main distinguishing feature, because no other particles reach the muon chambers (at least in the ideal case, there is some hadronic "punch-through" in practice). Muons are leptons and do not interact via nuclear interactions. Moreover, their heavy mass limits their bremsstrahlung losses, which scale with $\approx m^{-4}$.

- **Electron:** shown in the diagram in red. Electrons leave a signal in the tracker, and they are stopped in the electromagnetic calorimeter, where they deposit all their energy. The difference in stopping between electrons and muons is caused by the mass,

$m_e \approx (1/200) m_\mu$.

- **Charged hadron:** shown in the plot as a solid green line. Because they are charged, charged hadrons leave a signal in the tracker. They also leave some signal in the electromagnetic calorimeter, but they largely pass through, and are fully stopped in the hadron calorimeter via a nuclear interaction.

- **Neutral hadron:** shown as a dashed green line. Neutral hadrons leave a large signal only in the hadron calorimeter. They do not leave any signal in the tracker, because they do not have any charge.

- **Photon:** shown as the dashed blue line. Photons do not leave any signal in the tracker because they are neutral. They deposit all their energy in the electromagnetic calorimeter. It is worth noting that this is not the detection method used in this analysis. We detect photons via their conversion to $e^+ e^-$, which are detected in the tracker. The majority of photons that we use are very low energy ($\approx 1\,\text{GeV}$), and the resolution obtained via the conversion method is better than the resolution in the calorimeters (for details of our selection, see Section 5.1.3).

Knowing where a particle left a signal allows us to uniquely determine its general type, and in the ideal case, its mass and species as well.

3.2.1 Coordinate system

The detector is positioned around the interaction point (P5). The nominal collision point is defined as the origin of the CMS coordinate system. The coordinate system is right-handed, defined as follows:

- **x-axis**: points towards the middle of the ring.

- **y-axis**: points upwards.

- **z-axis**: points along the beam axis. The positive z-direction is along the LHC counter-clockwise beam, that is, towards the Jura mountains, or along the ring towards ALICE (see Fig. 3.2).

For detector operations, it is useful to define the pseudorapidity, η, as:

$$\eta = -\ln(\tan(\theta/2)),$$

where θ is the polar angle with respect to the z-axis. The pseudorapidity approaches the rapidity, y, for particles in the limit of $m \ll E$. Pseudorapidity depends only on the polar angle, which is readily measured, and not on the particle mass or other characteristics. This property makes pseudorapidity very convenient for the detector related measurements.

3.2.2 Tracker

The silicon tracker is the innermost CMS detector, with a diameter of 2.5 m and a length of 5.8 m. Its purpose is to provide an accurate description of particle trajectories in order to extract their momenta and to provide high-precision vertexing, which allows us to distinguish between directly produced particles and those originating in decays and thus coming from secondary vertices. This requires precise spatial and timing resolutions. The demands are coupled with the requirement to keep the material budget low to limit effects that obscure the initial interaction (such as multiple scattering, conversions, and nuclear interactions, which all modify particle kinematics or add new particles). Therefore, silicon detector technology was chosen. It employs reverse-biased p-n junctions. As a charged particle passes, it ionizes electrons along its path. The electrons are collected on the anode, while the holes are read out on the cathode. The tracker consists of two different implementations of silicon technology: the inner pixel detector and the outer strip detector. Figure 3.6 displays the

schematic diagram of the detector. The left panel is the cross-sectional view in the xy-plane, while the right panel is in the z-r plane (where r is any vector in the xy-plane. The detector is cylindrically symmetric). The right plot illustrates the size and η coverage of the tracker. Detailed descriptions of the pixel and strip detectors follow.

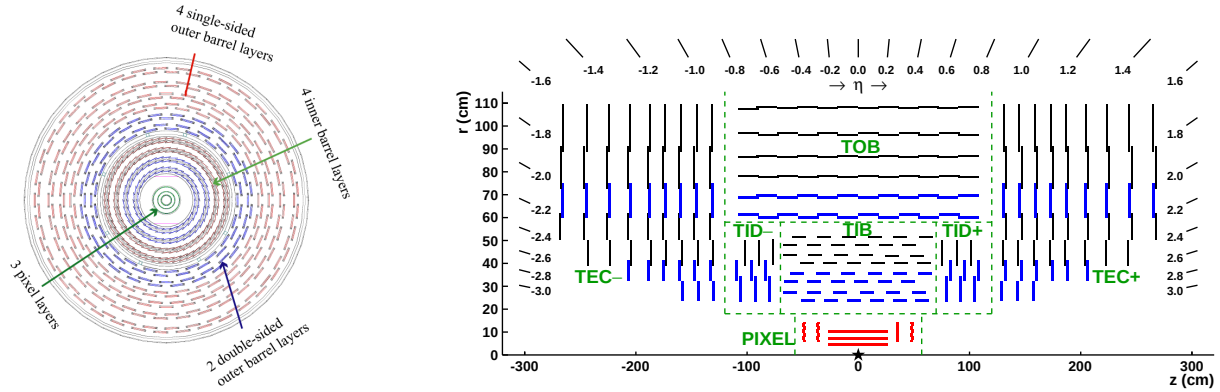

Figure 3.6: The diagram of the silicon tracker. **Left:** xy-plane cross section of the barrel portion of the tracker. The pixel detector is visible in green in the center, the strip is in blue and red on the outside. **Right:** Cross section in the z-r plane. The pixel detector is in red, and the strips are in black and blue. The figure also shows the detector's pseudorapidity, η, coverage. The acronyms are given in the text. Figure from [93].

3.2.2.1 Pixel detector

The pixel detector in 2016 consisted of three cylinders in the barrel region, at radii of 4.4, 7.3, and 10.2 cm from the interaction point, complemented by two disks on each side, arranged in a way that most tracks leave three pixel hits along their trajectories. Because the pixel is the detector which is the closest to the IP, it is crucial for the determination of the vertex from which a track originated, in an environment where the track density is the highest. Therefore, great granularity is needed, and a pixel technology, where each cell is read-out individually, was chosen. Each pixel has a size of $100 \times 150\,\mu$m, which adds up to a total of 66 million pixel cells.

The pixel detector underwent an upgrade to reach its Phase-1 configuration at the end-of-year stop in 2016/2017, adding one extra layer to the barrel region. The upgrade happened after our data were collected. For details, see [94].

3.2.2.2 Strip detector

The strip detector is composed of several subsets, shown in Fig. 3.6 as Tracker Inner Barrel (TIB), Tracker Outer Barrel (TOB), Tracker Inner Disk (TID), and Tracker Endcap (TEC). The read-out and price consideration preclude using the pixel technology for the outer layers of the silicon tracker. Instead, strip technology is used, where a single read-out channel collects information from a long thin strip. The strips are oriented along the z-axis in the barrel region, and radially for the endcaps, and are spaced $\approx 100\,\mu\text{m}$ apart. Thus, a particle measurement along a single layer provides two-dimensional information. For example, in the barrel region, we know the radius of the layer, and by detecting which strip fired we get the azimuthal angle. However, the third coordinate, z, is largely unknown (the strips have finite length and span only a small portion of the barrel layer, therefore there is some information, but it is very imprecise). To obtain a 3D measurement, several modules comprise of two layers mounted back to back, with strips at a slight angular offset with respect to each other. Combining the information from the two layers gives the remaining coordinate. The double-layered modules are shown in Fig. 3.6 in blue, while the single-layer modules are in black. The active area of the silicon strip detector covers $\approx 200\,\text{m}^2$ and consists of ≈ 10 million strips, while providing point resolution on the order of $20\,\mu\text{m}$.

3.2.3 Calorimeters

Even though the calorimeters are not directly used in our analysis, they constitute an integral part of the CMS experiment. Therefore, they are briefly described.

3.2.3.1 Electromagnetic calorimeter (ECAL)

The calorimeter induces an electromagnetic shower from high-energy electrons or photons, which converts all their energy into signal. The CMS ECAL uses lead tungstate (PbWO4) crystal scintillators. These dense crystals ($8.3\,\mathrm{g/cm^3}$) convert the energy into blue-green visible light, which is then collected by a photodetector. One of the advantages of PbWO4 is its short radiation length ($X_0 = 0.89\,\mathrm{cm}$), which allows for a fairly compact calorimeter. The size of the crystal in the barrel region is $22\,\mathrm{mm} \times 22\,\mathrm{mm}$ on the face side, and its depth is 230 mm, which corresponds to $26X_0$.The left panel of Fig. 3.7 shows one of the crystals. The right panel provides a sense of the size of the overall calorimeter.

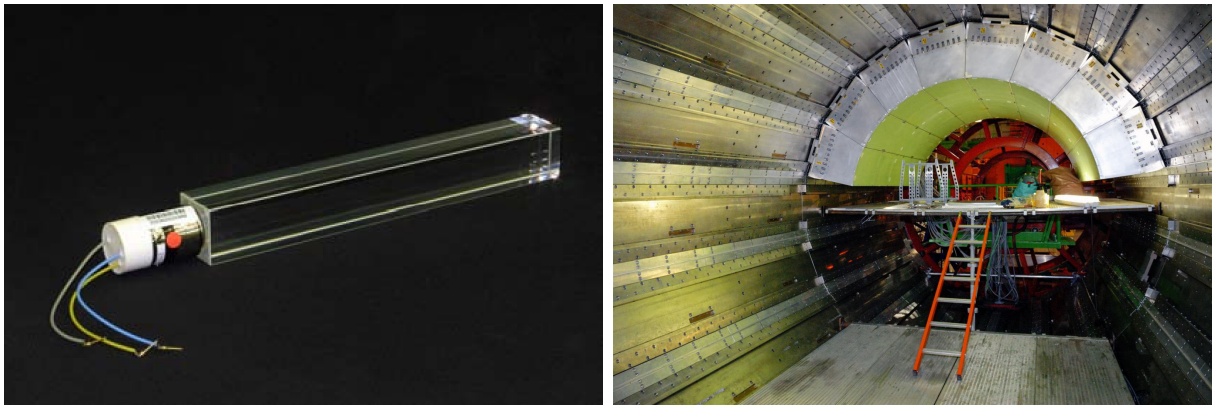

Figure 3.7: **Left:** Picture of a single PbWO4 crystal. Figure from [91]. **Right:** A quarter of the barrel ECAL mounted on the supporting structure inside of the hadron calorimeter. The internal radius is 1.29 m. The visible segments are supermodules consisting of 1700 individual crystals. Figure from [95].

3.2.3.2 Hadron calorimeter (HCAL)

The hadron calorimeter at CMS is divided into four assemblies:

- **Hadron barrel (HB)**: Placed inside the solenoid, with $1.77 < r < 2.95\,\mathrm{m}$ and $|\eta| < 1.3$, the HB is a sampling calorimeter, with alternating layers of brass and plastic

scintillator.

- **Hadron endcap (HE)**: Extends the coverage to $1.3 < |\eta| < 3.0$ and is similar in technology to the HB.

- **Hadron outer (HO)**: This is a two layer calorimeter placed outside the solenoid in the barrel region. Its purpose is to serve as a "tail catcher", detecting particles that made it through the HB.

- **Hadron forward (HF)**: This Cherenkov based calorimeter is placed 11.2 m from the interaction point, covering $3.0 < |\eta| < 5.2$. It is used in heavy-ion collisions for triggering, where the minimum-bias trigger is defined through a coincidence in the positive- and negative-z sides of the HF. The signal in the HF is also utilized to obtain collision centrality in AA collisions.

3.2.4 Muon detectors

As the name *Compact Muon Solenoid* suggests, muon detection is the central task of the entire experiment. The muon systems have three main tasks: *(i)* muon identification, *(ii)* triggering, *(iii)* momentum measurement[3]. There are three muon detectors relevant for the data presented in this dissertation, all of them placed as the outermost CMS detectors. Their respective positions are shown in Fig. 3.8.

3.2.4.1 Drift tubes (DT)

Drift tubes are positioned in the barrel region of the detector, among the steel of the flux-return yoke. They are organized in four concentric cylinders of 60-70 drift chambers each,

[3]Momentum measurement is relevant for very high-p_{T} muons, whose magnetic bending is too small for precise momentum determination in the tracker, and which benefit from the longer arm provided by the far-positioned muon chambers. At the p_{T} range relevant for this analysis, the muon-detector momentum-determination precision is too low to improve on the tracker-momentum measurement.

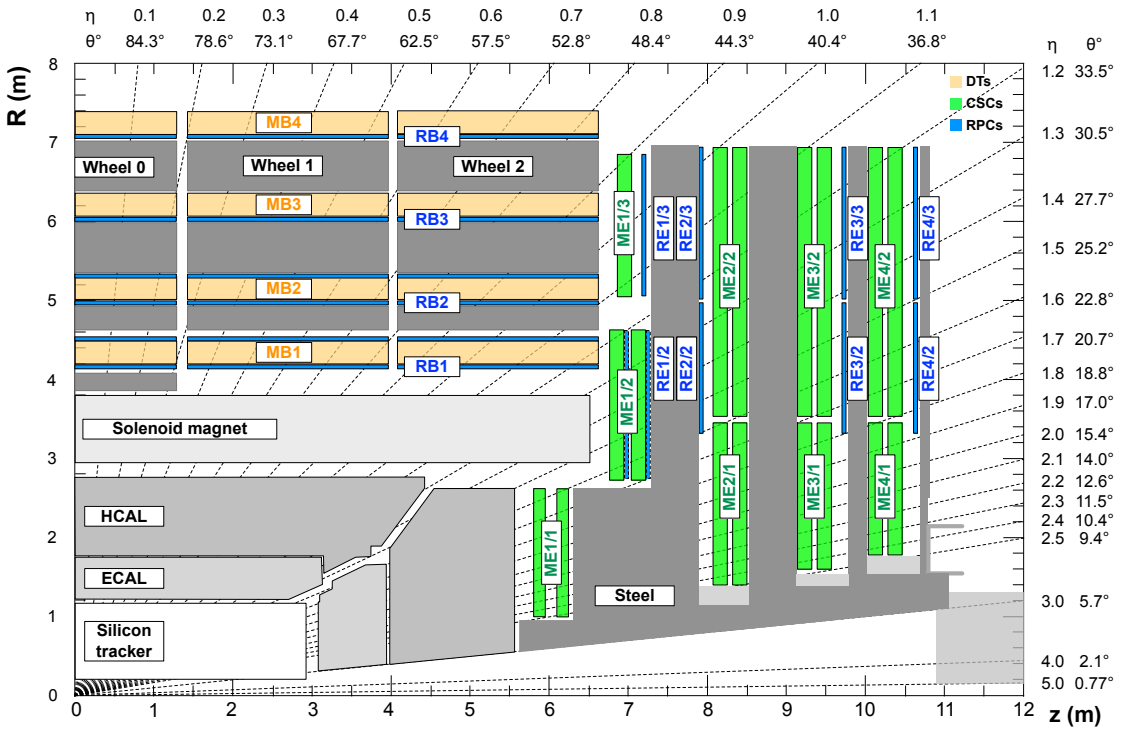

Figure 3.8: Diagram showing the cross section of CMS in the z-r plane. The individual muon stations are in yellow, blue, and green, highlighting their position and $|\eta|$ coverage. Figure from [96].

with the layers labeled as MB1-4 in Fig. 3.8. The basic technology is shown in Fig. 3.9. In the left panel, a single cell is depicted. It consists of a space with a height of 13 mm and a width of 42 mm filled with a mixture of Ar and CO_2. Each cell is about 2.4 m long. Through the middle of the cell runs an anode wire, which is held at 3600 V. A passing muon ionizes the gas in the cell. At the sides, two cathodes, held at -1200 V, collect the resulting signal. Additional electron strips are placed at the bottom and the top of the cell at 1800 V to shape the field.

The cells are combined into superlayers consisting of four layers of cells next to each other, each layer staggered by half a cell from the next one. Each chamber usually consists of three superlayers (some have only two superlayers), two of them positioned along the

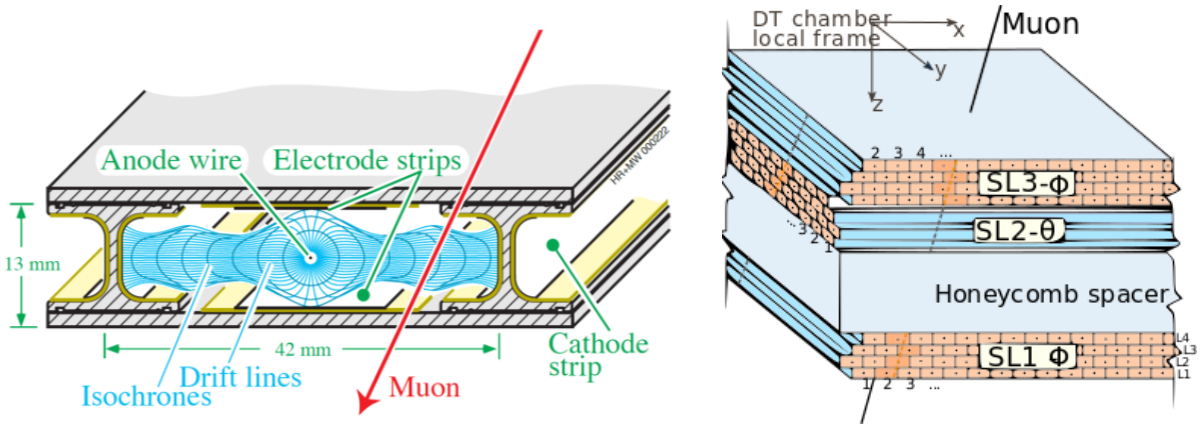

Figure 3.9: **Left:** Diagram of a single DT cell. Figure from [91]. **Right:** Diagram depicting the layout of the cells within a DT chamber. Individual cells are drawn as the small boxes with the wire in the middle. They are organized into three superlayers (labeled as "SL" in the picture), each of these consisting of four layers of cells. Figure from [97].

z-direction, and thus measuring the azimuthal angle ϕ, and one placed orthogonally to provide z measurement. The typical layout is shown in the right panel of Fig. 3.9. The realistic picture of DTs can be seen on the left side of the photograph in the introduction, Fig. 3.4, as the silver boxes placed inside the red coils of the return yoke.

3.2.4.2 Cathode strip chambers (CSC)

Cathode strip chambers are the main muon detectors in the endcap regions. The CSCs are multi-wire proportional chambers. The principle of operation is illustrated in the left panel of Fig. 3.10. A single layer consists of many anode wires that are stretched across the chamber, uniformly spaced 3.2 mm apart. They are held at a nominal voltage of 3600 V. The chamber is filled with a mixture of 40% Ar, 50% CO_2, and 10% CF_4. When a charged particle (muon) passes through the layer, it ionizes the gas. Electrons travel towards the anode. The field becomes stronger in close vicinity to the anode wire, and the accelerated electrons create an avalanche, which amplifies the signal. One coordinate is obtained from reading out the

anodes. To obtain the other coordinate, the cathode on one side of the layer is divided into strips that run perpendicular to the wires, with a pitch between 8.4 and 16 mm. There, the induced charge is read out to determine the other coordinate.

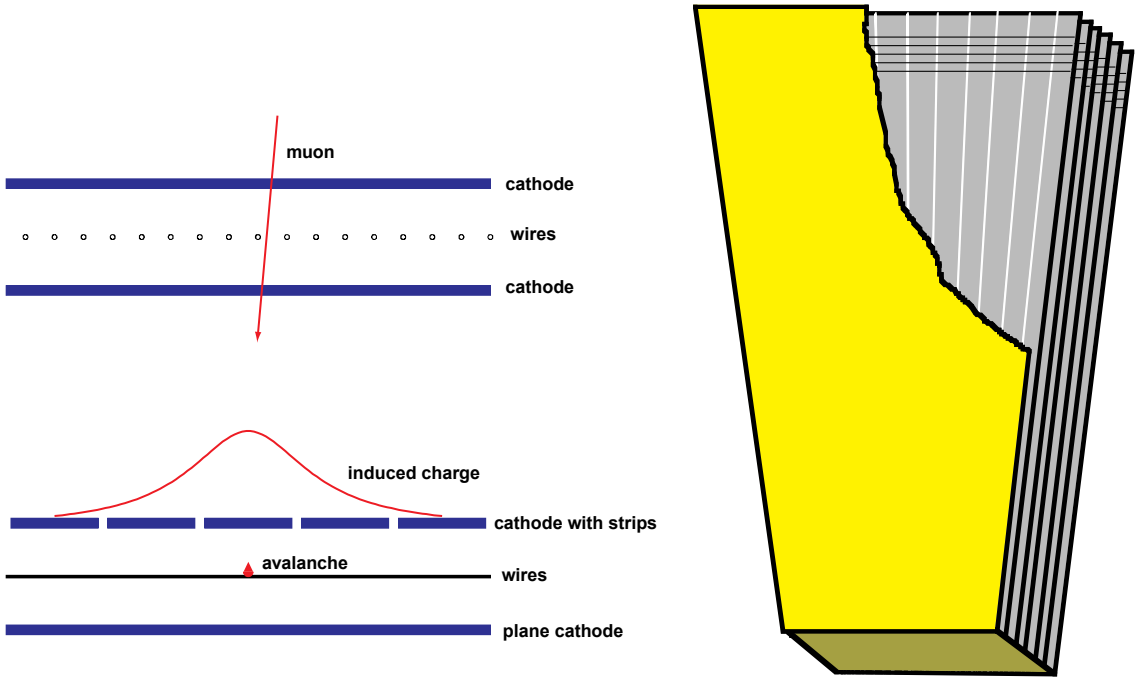

Figure 3.10: **Left:** Schema of operation of a single layer of a CSC. The panel consists of two views rotated 90° with respect to each other. The top half shows the situation looking along the direction of wires. The bottom half views the chamber along the strips, perpendicular to the wires. **Right:** The schema of a single CSC chamber. The chamber consists of six layers. The strips run in the up-down direction in the diagram. The left-right orientation of the wires is also shown at the top. Only a few wires are displayed, in reality they span the length of the chamber. Figures from [98].

The right panel of Fig. 3.10 explains how the wires and strips are oriented within each chamber. Each chamber consist of six wire and strip layers, where the wires run across (left to right) and the strips are placed along the length of the chamber. The chambers are placed in four disks on each side, each disk consisting of two (or three for the first) concentric rings of 18 to 36 chambers each. A photograph of a single chamber on a test stand can be seen

in Fig. 3.11. The placement and orientation in the actual experiment is photographed in Fig. 3.4, where CSC chambers are visible on the right side as two rings of chambers in a dark copper color.

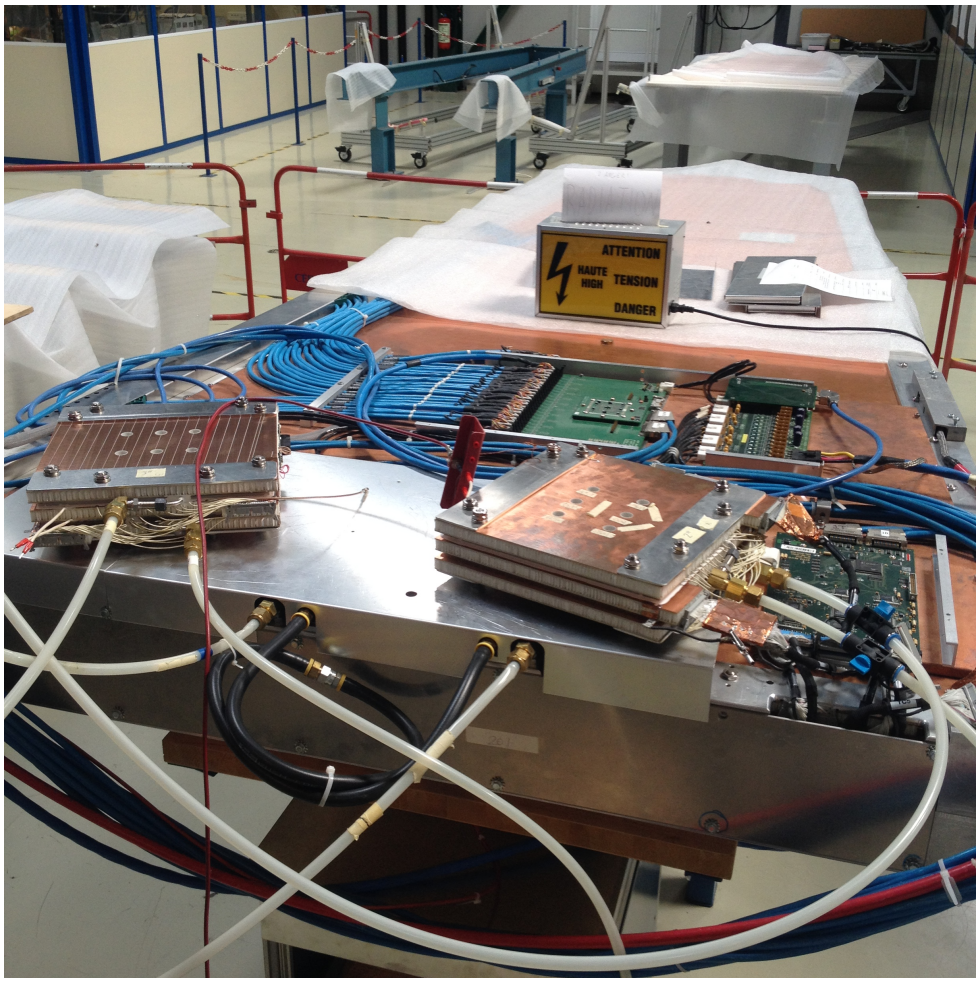

Figure 3.11: A photograph of a single CSC chamber on a test stand (the big chamber in the picture). The two small chambers on top are "miniCSCs" that the author helped to build and operate, and which were used for developing an improved working gas mixture that would not contain large amounts of CF_4.

3.2.4.3 Resistive plate chambers (RPC)

Resistive plate chambers are very fast detectors with timing resolution on the order of 1 ns (compared to the 25 ns gap between each bunch crossing). They are intended to provide bunch crossing identification as well as a fast, dedicated muon trigger. Unlike the DTs and CSCs, they are not limited to a subset of η coverage, but interspersed between both DTs and CSCs. The RPC technology is based on gaseous parallel-plate detectors. A gas mixture of 95.2% $C_2H_2F_4$, 4.5% iC_4H_{10}, and 0.3% SF_6 is enclosed between positively and negatively charged plates made out of bakelite. A passing muon triggers an avalanche, which is registered on the strip readout. The RPC design is double-gapped, which means that two layers are placed next to each other, with a common read-out in the middle, as illustrated in the left panel of Fig. 3.12. The design increases the signal on the read-out strip, improving the efficiency and allowing the detector to operate the gaps at a lower voltage. The right panel of the figure shows the actual chambers, in their endcap configuration.

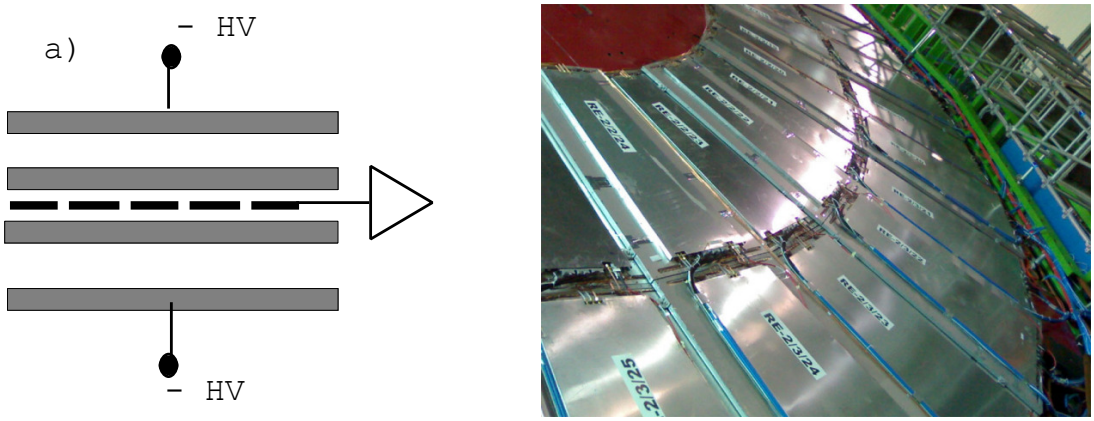

Figure 3.12: **Left:** Illustration of double-gapped design of RPCs. Two sets of gas filled gaps, shown in white, are above and below the readout, which is in the middle, common for both gaps. The gray boxes are the plates. Figure from [98]. **Right:** Photograph of the RPC chambers during installation on one of the endcaps. Figure from [99].

3.2.5 Data reconstruction

Signals from the various subdetectors need to be reconstructed into physics-oriented information, such as tracks with known p_{T}, rapidity, charge, etc., or energy deposited in the calorimeter (expressed as the energy of the particle in GeV, as opposed to an electric signal). This is the task of the CMS reconstruction algorithms. The first steps are performed individually in each subsystem. We will focus only on reconstruction in the tracker and muon chambers, as these are the relevant detectors for this analysis.

3.2.5.1 Reconstruction in the silicon tracker

First, adjacent pixels with a signal above a threshold are clustered together, and the hit position is determined through either a projection onto the coordinate axes, or based on the MC-derived template [93]. The threshold for a pixel to be considered corresponds to an equivalent charge of 3200 electrons, compared to 21 000 expected from a minimum-ionizing particle. A similar procedure is performed in the strip detectors. The hit reconstruction is very efficient, typically around 99.8 %.

In the next step, tracks are reconstructed from the hits. The tracking software that performs the reconstruction is based on a Kalman filter [100]. The track finding proceeds in several iterations, where tracks that are easiest to find are identified first, and their hits are removed. The algorithm then proceeds to find harder to identify (low-p_{T} or displaced) tracks from the remaining hits. The individual tracks are formed from the seeds obtained from the seeding layers in the inner part of the tracker, in an outward-direction search for compatible hits. There is also an inward-direction pass to recover any missing hits. Once the hits are assigned to a specific track, the track parameters are improved by refitting all the hits, taking into account scattering in the tracker material and inhomogeneities in the magnetic field. The whole track-reconstruction procedure is very computation-intensive, and

various optimizations are performed in each step.

The collection of tracks obtained from the tracking reconstruction is very permissive and contains fake tracks. In the analyses, additional conditions on the quality of tracks are usually applied (e.g. requiring a specific number of hits in the pixel or strip detectors, or χ^2/ndf requirements on the track fits). Of special note, the *high-purity* requirement is often used, including in this analysis (for details of the selection, see Section 5.1). It is the most stringent of the three selections defined in the track collection, with *loose* being the most permissive and *tight* being the middle. The *high-purity* requirement applies a set of cuts requiring a minimum number of tracker layers, a minimum number of tracker layers with 3D measurement (see Section 3.2.2 for a description), a maximum number of layers passed by the track but missing in the fit, and various parameters requiring a good quality fit with acceptable spatial and momentum resolutions. The exact requirements depend on the specific iteration of the tracking algorithm and are discussed in [93].

3.2.5.2 Reconstruction in the muon chambers

The first step in the reconstruction [101, 102] uses only local information from a single muon chamber (CSC, DT, or RPC). The hit positions are determined based on the chamber's respective technologies. RPCs have only a single layer per chamber, but CSCs and DTs obtain several hits per muon per single chamber. From these hits, track segments are formed in each chamber using a linear fit to the position of the hits. The segments are then used as seeds for a track fit in the muon system, which, similarly to fits in the tracker, is based on a Kalman filter. To improve the resolution, a beam-spot is added to the fit. The resulting tracks from the muon chambers are denoted as *standalone muons*.

3.2.5.3 Muon reconstruction

The standalone muons reconstructed in the muon chambers are available as a collection and are used in technical studies, but they suffer from poor p_{T} resolution. Therefore, information from the tracker and muon chambers is combined in an overall fit [101]. Two approaches are used:

- *Global muon reconstruction (outside-in)*: The standalone muons are used as a seed, and the algorithm seeks a matching track in the tracker. If it finds one, a common fit to both parts is performed. The resulting muon is called a *global muon*.
- *Tracker muon reconstruction (inside-out)*: The muons are reconstructed starting from tracker tracks, which are propagated outwards to the muon system, looking for a matching segment in a muon chamber. A resulting muon is called a *tracker muon*. This approach is more computationally demanding because of the large number of tracks in the tracker, but it allows muons with lower momentum to be reconstructed. These low-p_{T} muons might leave some hits in the muon chambers, but not enough for a good segment, and they are thus lost by the outside-in approach.

Another collection of muons used in CMS is obtained from a particle flow (PF) algorithm [103]. The algorithm starts with the candidates reconstructed with the standalone, tracker or global muon algorithms, and it then applies various quality criteria based on the information from other CMS subdetectors.

This analysis starts with the *tracker muon* collection. The full muon selection for this analysis is explored in Section 5.1.1.

Chapter 4

Data sets and Monte Carlo samples

4.1 Data sets and trigger

The data set used in the analysis was collected over two and a half weeks in November and December of 2016, in $p + \mathrm{Pb}$ collisions at $\sqrt{s_{_{NN}}} = 8.16\,\mathrm{TeV}$. The data taking period was divided into two ranges: in the first (runs 285479-285832), the Pb beam was circulated with its momentum pointing in the positive z-direction, and the collisions are denoted as $\mathrm{Pb}+p$. In the second part (runs 285952-286496), the p beam went in the positive z-direction and we denote the collisions as $p + \mathrm{Pb}$. Beams were reversed to get a good handle on any systematic effects due to the beam direction. While the CMS detector is designed, in ideal case, symmetric with respect to the z-axis, there are always minor differences in reality (e.g. malfunctioning "dead" modules, or the actual CMS layout is not perfectly symmetric). Note that the $(\mathrm{Pb}+p)/(p+\mathrm{Pb})$ distinction is used only when discussing the directions specifically. In general, the text "the $p + \mathrm{Pb}$ collisions" will refer in this dissertation to both portions of the data.

To collect data, we used the HLT_PAL1DoubleMuOpen_v1 trigger[1]. This trigger requires

[1]Note on the trigger naming scheme: HLT stands for High Level Trigger. CMS physics triggers universally

two muon candidates in the muon detectors at the level-1 (L1) trigger with the loosest possible selections to maximize the detection efficiency. During the 2016 $p + \mathrm{Pb}$ run, this trigger was operated without any prescale (meaning it collected all the events passing its selections). The primary data stream for the stored data is `/PADoubleMuon/PARun2016C-PromptReco-v1/AOD`, which contains all events passing the double muon trigger. The data set was processed using the standard CMS software, version CMSSW_8_0_30 and the offline *global tag* 80X_dataRun2_v19 (the global tag is an internal tag which specifies what detector conditions and settings are appropriate for the data reconstruction).

To ensure good quality of the data set, run selection is usually performed. This step is done centrally at CMS and proceeds as follows. The smallest data chunk that is considered in this step is *luminosity section*, which corresponds to about 23 s of data acquisition (for our trigger it is equal to $\approx 10\,000$ events) The luminosity sections selected for this analysis are based on a certified list, validated by the different Detector Performance Groups (DPGs) and Physics Object Groups (POGs). The certification consists of checking a set of control plots, specific to the detector or physics object, and deciding whether the data quality is good. The author performed this certification for the CSC DPG for a few years. For the CSC detector, the basic control plots primarily display active chambers, hit positions, and various resolution and timing variables. The data certification is done in two steps: *(i)* quick online to spot any problems promptly, and *(ii)* final data quality check, done offline after full reconstruction, to determine the list of good runs and luminosity sections. The list of lumi-sections deemed good by the relevant DPGs and POGs is then published as a JSON file. The data sample for this analysis is defined in the following JSON files: `/afs/cern.ch/cms/CAF/CMSCOMM/COMM_DQM/certification/Collisions16/13TeV/HI/Cert_285479-`

start with the HLT label, since, one way or the other, they always go through the HLT (even if as a simple pass-through). PA stands for proton-nucleon collisions. L1 means that the actual trigger is level-1 based. DoubleMu signifies that the trigger requires two muons for triggering. Open is a quality flag for L1 seeds, in this case the loosest possible, and without any p_{T} cut-off.

285832_HI8TeV_PromptReco_pPb_Collisions16_JSON_NoL1T.txt for the Pb + p portion of the run and /afs/cern.ch/cms/CAF/CMSCOMM/COMM_DQM/certification/Collisions16/13TeV/HI/Cert_285952-286496_HI8TeV_PromptReco_Pbp_Collisions16_JSON_NoL1T.txt for the p + Pb portion of the run[2].

The integrated luminosity corresponding to the trigger and selection used in this thesis is listed in Table 4.1 for each portion of the run.

Direction	Delivered L_{int} [nb^{-1}]
Pb + p	62.65
p + Pb	111.91
Total	174.56

Table 4.1: Integrated luminosities for our data.

4.1.1 Event selection

In the next step, the quality of each event in approved lumi-sections is considered. This is done event by event in the analysis code when creating our data skims. This selection is standard in the HI dilepton group and not specific to this analysis. The purpose is to select inelastic hadronic collisions and to remove the background sources present in our trigger, such as beam and residual-gas or beam-halo and beam-pipe (scraping) interactions. Only events passing the following selection are accepted for further analysis:

- **HF coincidence:** At least one tower hit with an energy above 3 GeV is required in coincidence on each side of the hadronic forward (HF) calorimeter. This selects the hadronic inelastic collisions, which are expected to produce particles going both in

[2]The naming scheme (pPb/Pbp) in the certified files is opposite to the usual convention for pA collisions. The naming was chosen by a pp expert, who labeled first portion of the run as pPb (despite it being really Pbp), and then labeling the other portion as Pbp. This was never corrected.

the positive and the negative z-direction that are then detected by the HF. A similar selection is used in minimum bias data collection and is highly efficient for the events of interest. The cut removes most of the beam-nonbeam (gas, wall) interactions, as well as the ultraperipheral collisions (where the interaction is between the electromagnetic fields surrounding the nuclei, which pass near each other, but not close enough for a hadronic interaction).

- **Vertex selector:** Events are required to have a good-quality primary vertex with at least two tracks originating from it. The vertex has to be positioned within 25 cm of the detector center in the z-coordinate, and within a 2 cm radius in the xy plane. Figure 4.1 shows the distributions of primary vertices in z-coordinate (left panel) and in the xy plane (right panel). Plotted are values for all PV present in the data sample, regardless of whether they contain any particle of interest. Both plots are in a log scale. While only the events passing the vertex selector and other event cuts are plotted, we can observe that the vertex distribution is well separated from the cut values (25 cm for z, 2 cm for xy), and therefore the vertex selector is not removing any real events.

- **Scraping filter:** The filter removes the interactions between the beam halo and beam pipe walls. If the actual beam center hit the wall, the number of particles produced would almost surely damage CMS, or, at least, end the run (and such event does not need to be considered here). However, the beam halo is diffuse enough that it can interact non-catastrophically with the wall and create a large multiplicity event that is characterized by many tracks without a common origin within the CMS tracker. The fraction of these tracks that are good quality is low. The filter removes these events by requiring that all events with at least 10 tracks have at least 25% of their tracks to be of good quality.

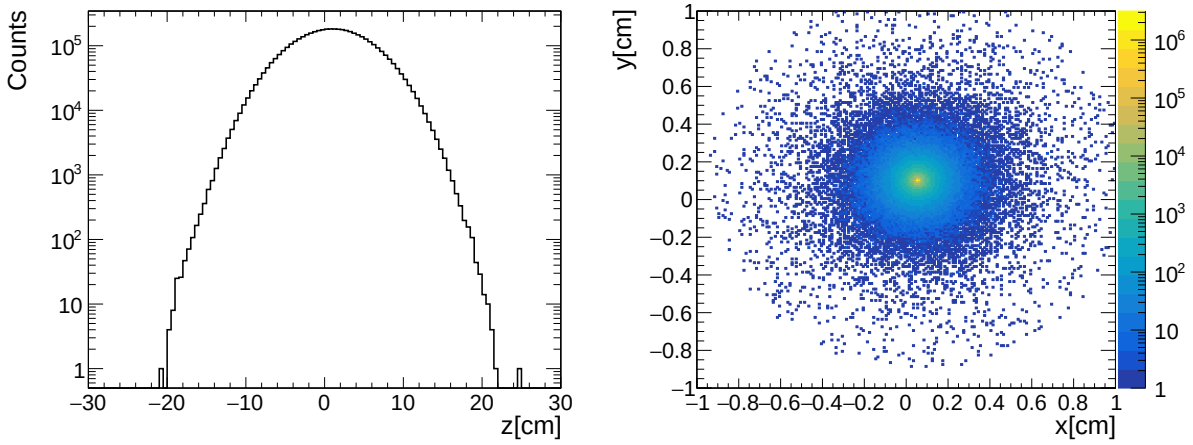

Figure 4.1: The distribution of all primary vertices for the data sample. **Left:** The z-coordinate distribution. **Right:** The distribution in the xy plane.

4.2 Monte Carlo

The analysis uses MC samples officially created by CMS, which were requested with tailored settings specifically for this analysis. The initial hard-scattering nucleon-nucleon process is simulated with PYTHIA8 [104]. The settings for this step were chosen to be comparable with the other relevant analyses either in pp or HI collisions. The event requires generation of either χ_{c1} or χ_{c2} via a gg, gq or qq interaction. The PYTHIA tune was CUETP8M1 [105], which is a CMS-derived tune based on the Monash Tune [61] that additionally incorporates underlying event measurements. The PYTHIA parameter $\hat{p_{\mathrm{T}}}$(Min) that selects the minimum invariant p_{T} used for the generating parton-parton interaction is set to 4.5 GeV. The $\hat{p_{\mathrm{T}}}$(Min) parameter affects the hardness of the resulting p_{T} spectrum, and the value of 4.5 GeV was found to approximate the data spectrum well (for further treatment of the p_{T} distributions, see Section 4.3.2). Additionally, at this stage the χ_c decay to J/ψ and γ is simulated and constrained to be the only decay channel. The J/ψ is also forced to decay primarily to $\mu^+\,\mu^-$, however, the final state radiative decays of ($\mu^+\,\mu^-$ + any # γ) are allowed and modeled by

PHOTOS [106]. To optimize the event generation, two *acceptance filters* are applied at this step. First, only events which produced a J/ψ with $p_{\mathrm{T}} > 5.7\,\mathrm{GeV}$ are considered. Second, the events must have a $\mu^+\,\mu^-$ pair, where each muon fulfills $|\eta| < 2.5$, $p_{\mathrm{T}} > 1.2\,\mathrm{GeV}$, and $p > 3.3\,\mathrm{GeV}$. All of these acceptance cuts are supplanted in the analysis by stricter offline cuts and thus play no role besides lowering the amount of computer resources wasted on events that fall outside of the detector acceptance.

Next, the PYTHIA event is embedded in an underlying heavy-ion collision that is simulated with EPOS LHC (v3400) [107]. The full CMS detector response to the overall event is modeled with GEANT4 [108]. Afterward, the event is processed through the trigger emulation, and finally reconstructed by the CMS software as if it was a real-data event.

There were two MC samples created: one in the p + Pb and the other in the Pb + p direction. The center-of-mass is moving with respect to the lab frame in p-going direction with 0.465 units of rapidity. The two PYTHIA samples are generated (independently of each other) in the center-of-mass frame with $\sqrt{s_{_{NN}}} = 8.16\,\mathrm{TeV}$, and then boosted in the appropriate directions. Similarly, two independent EPOS samples are used with the matching boost. Each of the samples consist of ≈ 15 million simulated events (post acceptance filters). Given the acceptance filter efficiency of $\approx$ 10%, a total of roughly 300 million PYTHIA interactions had to be generated. This required a significant amount of computer resources. However, the large sample was necessary because the overall reconstruction efficiency of the χ_c is low, on the order of 1%, and we need a reasonable number of reconstructed χ_c in each kinematic region of the analysis. The official samples are organized in the CMS Data Aggregation Service (DAS) as `/Chic1Chic2_JpsiTogg_MuMuTogg_pThat4p5_Pbp-EmbEPOS_8p16_pythia8_evtgen/pPb816Summer16DR-80X_mcRun2_pA_v4-v7/AODSIM` for the Pbp direction and `/Chic1Chic2_JpsiTogg_MuMuTogg_pThat4p5_pPb-EmbEPOS_8p16_pythia8_evtgen/pPb816Summer16DR-80X_mcRun2_pA_v4-v5/AODSIM` for the pPb direction.

Additionally, several smaller private samples were used to optimize the MC settings, as

well as for some early studies. However, these have no effect on the analysis, because all the parts where it could matter were redone with the official MC production.

4.3 MC weighting

Three weights are added to the official MC sample, in order to improve the MC match to the data:

1. Number of tracks
2. Transverse momentum p_{T}
3. pPb/Pbp direction

The details of each weight are described in the following section. These three weight categories are assumed to be independent of each other. Therefore, they are simultaneously applied to the MC as a product.

4.3.1 N_{tracks} weighting

The PYTHIA events are embedded in an EPOS event that simulates the underlying event. However, the primary track distribution in data and MC do not quite match (see left panel of Fig. 4.2, blue points are data and red unweighted MC). This could introduce a bias when using the MC sample for efficiency estimation, because the events which have a low number of tracks in the primary vertex would be overrepresented in the sample. And since we observe that the reconstruction efficiency (especially of photon conversions) decreases with the increasing number of tracks in the detector, we would overestimate the overall efficiency in any result that integrates in the number of primary tracks. Therefore, weighting is applied

to the MC sample to ensure that high-multiplicity events have the proper impact on the MC sample.

There are several possible definitions of number of tracks that can be used for the weighting. Three options were considered: an overall number of tracks in the event, the number of tracks originating in the primary vertex associated with the J/ψ (uncut, raw number), and the number of tracks originating in the primary vertex with J/ψ that satisfy a quality selection. Following the study documented in Section 5.2.1.2, the number of tracks in the primary vertex with quality selection is used for weighting as well as for our results.

The J/ψ candidates are used in the weighting procedure. There are two main reasons for using J/ψ instead of χ_c: *(i)* the statistics are much better, which reduces random fluctuations that would otherwise be present in the χ_c samples, and *(ii)* the background is much smaller in the peak region, so the estimation can be made directly from the distributions without the need for background subtractions. The underlying assumption is that the production mechanism of χ_c and J/ψ is similar enough that we do not expect that the particles have noticeably different distributions as a function of the number of primary tracks. The N_{tracks} distributions are shown in Fig. 4.2 on the left side, while the actual weight as a function of N_{tracks} is shown on the right side. The weights are obtained by dividing the distribution in data (blue on left plot) by the unweighted MC distribution (red on left plot) with a suitable normalization. The normalization was chosen such that the overall normalization of the weighted sample equals the normalization of the unweighted sample (the total number of events is preserved).

4.3.2 p_{T} weighting

The p_{T} distribution of χ_c in the MC is a bit softer than the distribution in data. Because the p_{T} spectrum differs between the χ_c and J/ψ (our final result of χ_c to J/ψ ratio is equal

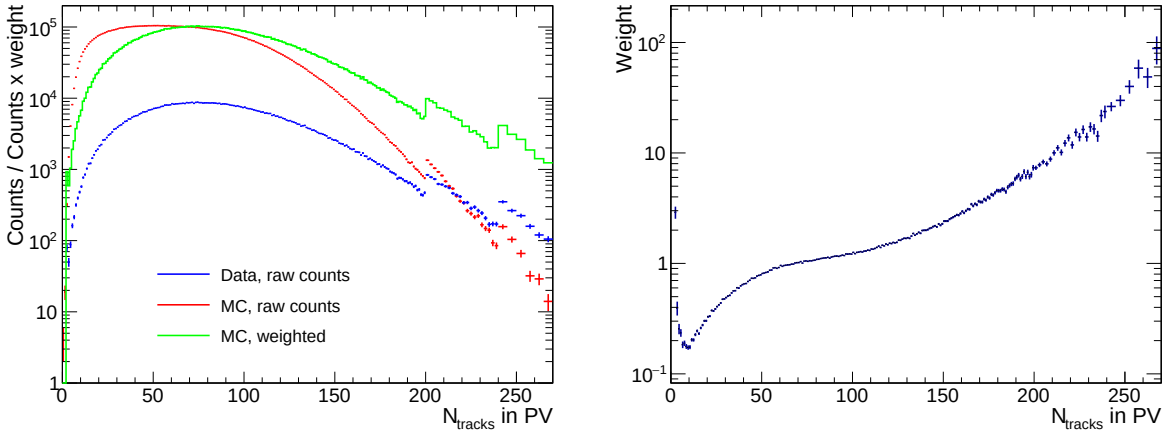

Figure 4.2: **Left:** The distribution of primary tracks in events with J/ψ for data (blue), unweighted MC (red) and MC after the weights were applied (green). The discontinuities present at 200 and 240 are caused by a change in the binning (from 1 track value per bin to 2, and then to 5) and have no effect on the ratio of the distributions (i.e. weight). **Right:** Weights for the MC sample.

to the ratio between the spectra of χ_c and J/ψ, and the ratio is p_{T} dependent), we cannot use J/ψ to derive this type of weighting. Instead, the raw yield of χ_c from the MC sample in the given p_{T} bin is compared with the raw yield obtained by fitting data in the same p_{T} bin using the nominal fitting procedure, and the ratio of data/MC is calculated. This is done in the p_{T} of the J/ψ from χ_c decay, since that is the variable that we use for our results. We thus have 4 data points in the binning of final results. Because the χ_c statistics are limited, the points are then fitted by a straight line. The fit as a function of p_{T} is than used as the p_{T} weight. The results are in Fig. 4.3. The top plot shows the raw yield for the MC and the data. The overall normalization for the MC is chosen so the total raw yield between the data and the MC is the same. This ensures that the weight, shown in the bottom panel, is normalized to 1, i.e. does not affect the overall MC statistics. The linear fit yields

$$W(p_{\mathrm{T}}) = 0.104 * p_{\mathrm{T}} - 0.07, \tag{4.1}$$

where W is the weight and p_{T} is the p_{T} of the J/ψ that came from the χ_c decay. The function is applicable in the range of $6.5 < p_{\mathrm{T}} < 30\,\mathrm{GeV}$.

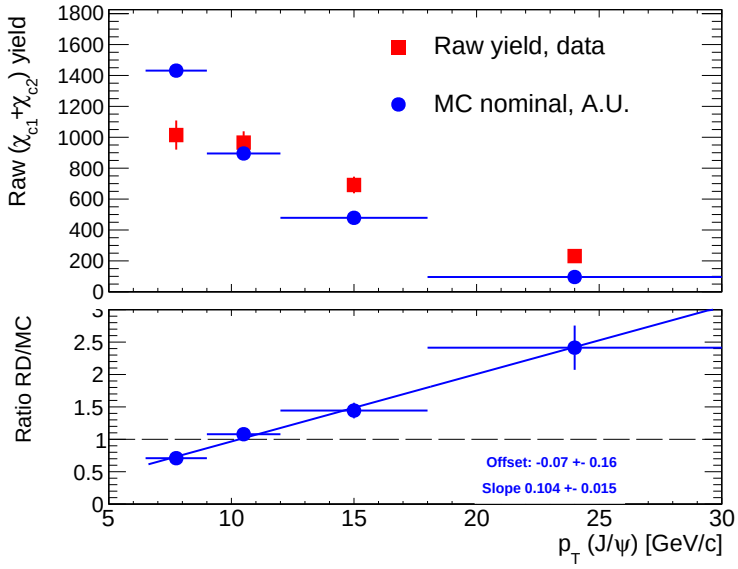

Figure 4.3: **Top:** The raw χ_c yield as a function of p_{T} of the daughter J/ψ. The data points are in red, nominal MC in blue. The MC is scaled to match the integrated data counts. **Bottom:** Ratio of the data/MC, fitted with a linear function in blue.

4.3.3 Combining $p + \mathrm{Pb}$ and $\mathrm{Pb} + p$ directions

For most results, we want to combine sample from the two run directions (p+Pb and Pb+p). We checked that the CMS detector efficiencies for χ_c are largely symmetric (see Section B.1). However, to take into account any possible differences, the MC samples were weighted to match the recorded luminosity for each direction. In this case, the weight is a single number for each direction: 0.72 for MC in the $\mathrm{Pb} + p$ direction (corresponding to $62.65\,\mathrm{nb}^{-1}$) and 1.28 for $p + \mathrm{Pb}$ ($111.91\,\mathrm{nb}^{-1}$).

Chapter 5

Signal extraction

Obtaining uncorrected yields consists of two steps. First, we apply selection criteria to particles of interest (i.e. decay daughters of χ_c). For this analysis, the decay chain is $\chi_c \to J/\psi\,\gamma \to \mu^+\,\mu^- + e^+\,e^-$ (conversion). We need to select muons in order to reconstruct the J/ψ. We used the established procedure within the dilepton HI group and standardized criteria for muon selection. However, there is little guidance within the HI group for reconstructing photon conversions to electron-positron pairs. The conversion selection was inspired by a comparable χ_b analysis in $p+p$ collisions [109, 110], and then updated for $p+\mathrm{Pb}$ collisions. Section 5.1 details the selection stage.

The second step in the yield extraction combines the selected particles to create an invariant mass spectrum, where the parent resonance is visible, and then fitting the spectrum with a suitable function to extract the yield. This stage is described in Section 5.2.

The acceptance, efficiency, and overall corrections that are applied to the results in order to account for the selection are discussed in Section 6.

5.1 Particle selection

The selection criteria are divided into subsections for muons, conversions, J/ψ, and χ_c. For each particle, the acceptance region and identification selection are provided. In the case of muons, an additional trigger selection is performed. For the χ_c, no specific acceptance is required, because the χ_c kinematics are largely constrained by the J/ψ selections (since the decay photon from $\chi_c \to J/\psi\,\gamma$ is very soft in the particle rest frame, the χ_c kinematics are very similar to its daughter J/ψ).

5.1.1 Muon selection

5.1.1.1 Acceptance

The muons are selected with the acceptance cut recommended by the HI group for analyses using the double muon trigger (HLT_L1DoubleMuOpen). The acceptance cut is listed in Table 5.1 and illustrated by the blue line in Fig. 5.1.

$\lvert\eta\rvert$ range	p_{T} cut [GeV]
$0 < \lvert\eta\rvert < 0.3$	$p_{\mathrm{T}} > 3.4$
$0.3 < \lvert\eta\rvert < 1.1$	$p_{\mathrm{T}} > 3.3$
$1.1 < \lvert\eta\rvert < 2.1$	$p_{\mathrm{T}} > 5.5 - 2.0 \times \lvert\eta\rvert$
$2.1 < \lvert\eta\rvert < 2.4$	$p_{\mathrm{T}} > 1.3$

Table 5.1: Muon acceptance used in the analysis

5.1.1.2 Identification

There are three muon selections that are commonly used in the dilepton group, called *tight* ID, *soft* ID, and *hybrid-soft* ID. The tight ID [112] is the most stringent, and is used for high-p_{T} analyses (e.g. Z boson) or analyses that need a very pure sample of muons with

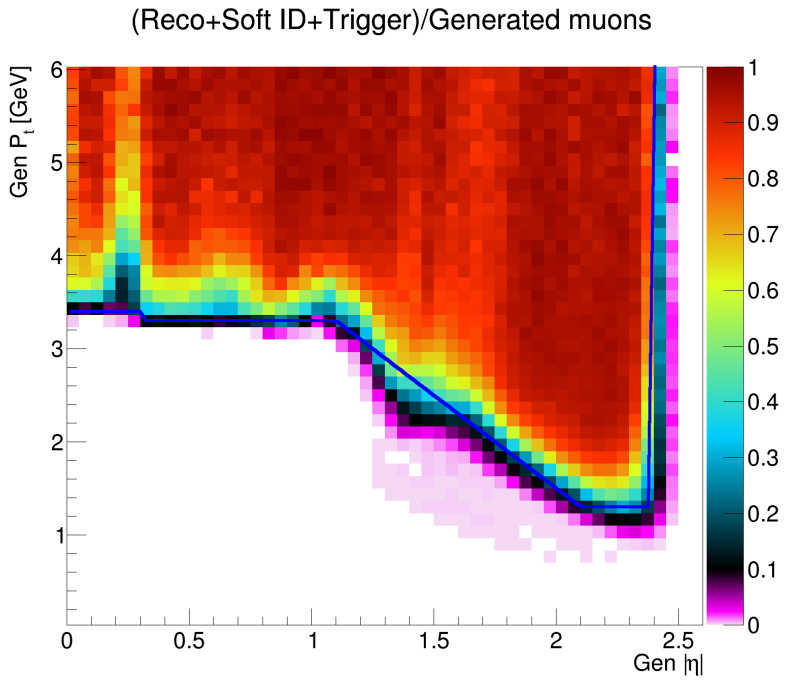

Figure 5.1: Blue line: Muon acceptance cut for the analysis. The efficiency shown is the MC single muon efficiency of *soft* muon identification and trigger. Figure from [111].

low background. The soft ID [112, 113] is more permissive and has the largest efficiency of the three selections, especially at the low-p_{T} edge of acceptance, and is commonly used for analyses studying particles that decay into muons with low p_{T} (e.g. J/ψ, Υ), such as this analysis. Hybrid-soft [111] is a modification of soft ID derived specifically for the Pb + Pb collisions, where the soft ID allows too much background. Hybrid-soft is in the middle in terms of stringency. Muons in this analysis are required to pass the *soft muon* ID selection, as recommended by the muon Physics Object Group (POG) and used by other comparable analyses. The soft muon selection consists of several cuts:

- *Tracker Muon One Station Tight*: The muon is reconstructed as a tracker track matched with at least one muon segment within 3σ of the track projection, in x- and y-coordinates. The muon tracks are also arbitrated, which means that the matches of

different inner tracks to a single muon segment are resolved, and a unique match is obtained.

- *Track high purity*: Tracks in the tracker are required to pass a high-purity flag, which rejects poor quality tracks.

- *n pixel layers* > 0 and *n strip layers* > 5: To further improve the muon track quality, a minimum number of pixel and strip layers with hits is required.

- $Dxy < 0.3$ cm $Dz < 20$ cm: There is a limit on the maximum distance between the event vertex and the muon track in the transverse plane, *Dxy*, and the longitudinal plane, *Dz*.

5.1.1.3 Trigger

Muons are matched to the online trigger objects triggering the event (HLT_PAL1DoubleMuOpen_v1, see Section 4.1), i.e. the muons are required to be the ones that fired the trigger. The matching is done kinematically, by comparing the direction and p_{T} between the offline and online muon. If they are within a certain range of each other, they are assumed to represent the same muon. The values required for matching were the same as in the other comparable HI dilepton analyses.

5.1.2 J/ψ selection

The J/ψ candidates are formed by combining all possible muon pairs within a single event. Then, we require that the muon pair has the opposite sign of charge, rapidity $|y_{\mathrm{lab}}(J/\psi)| < 2.4$, and $6.5 < p_{\mathrm{T}}(J/\psi) < 30\,\mathrm{GeV}$. Additionally, the dimuon vertex fit is performed on the muon pair, and the resulting fit must have a probability larger than 1% that the tracks originated from a common vertex. Contributions from non-prompt decays are removed by

requiring that the J/ψ lifetime over its uncertainty is smaller than 3, i.e. that there is not a strong evidence that the J/ψ lifetime is inconsistent with zero.

5.1.3 Conversion selection

5.1.3.1 Acceptance

The photon conversion acceptance region is defined as $|\eta(\gamma)| < 2.4$ and $p_{\mathrm{T}}(\gamma) > 0.5\,\mathrm{GeV}$. The p_{T} cutoff is motivated by the conversion reconstruction efficiency, which becomes very small below $0.5\,\mathrm{GeV}$.

5.1.3.2 Identification

Photons are reconstructed via their conversion to electron-positron pairs. This is the most complex part of the reconstruction. The overall reconstruction efficiency of conversion is low (a few percent), because it includes not only the efficiency of the reconstruction itself after the photon was converted, but also the probability that the conversion will happen in the first place. The inner trackers, where the conversion needs to take place, are optimized for a low material budget, and the conversion probability is not very high. Therefore we lose the majority of χ_c decays because the photon simply does not convert in the detector material. Despite the low efficiency, this analysis employs conversions, because the momentum resolution is good, especially in the barrel region. This is in contrast to the most obvious method to reconstruct photons via the electromagnetic calorimeter, which does not have a good resolution for relatively soft photons from $\chi_c \to J/\psi\,\gamma$ decay.

Photon conversions are characterized by an electron-positron pair originating from the conversion vertex with an e^+e^- invariant mass consistent with zero. The CMS software performs the initial conversion reconstruction. The software selects conversion candidates and creates a photon-conversion collection (similar to collection of muons). The next steps

are done at the analysis level. First, the *duplicate* conversions are removed. These come from tracks that were split in the tracker, creating a second, fake conversion with almost identical kinematics. All conversions in a single event that come from general tracks are considered in this step. The logic for removing the *duplicate* conversion is illustrated in Fig. 5.2, and is as follows:

1. If the conversion does not share either of its tracks with any other conversion, it is kept (left panel in the figure).

2. If the conversion shares a single track with another conversion, but the other (non-shared) track is different, the conversion is considered to be a genuine combinatorial option and is kept (middle panel in the figure).

3. If the conversion shares a track with another conversion, and the other (non-shared) track is almost identical (defined as having difference of p_{T} smaller than $0.1\,\mathrm{GeV}/c$ and the difference in direction $dR = \sqrt{\Delta(\eta)^2 + \Delta(\phi)^2}$ smaller than 0.05), then the conversions are considered duplicate (right panel in the figure). The number of valid tracker hits in the split track is compared, and the conversion with the higher number is kept, while the other is removed. In case of a tie in the number of valid hits, the conversion vertex probability is used as a tie-breaker.

This process removes around 3% of the conversions both in data and in the MC.

Furthermore, basic quality criteria are applied to the conversion collection in order to be used for χ_c reconstruction:

- *conversion quality*: The electron tracks for the conversion are required to be reconstructed as general tracks in the tracker.

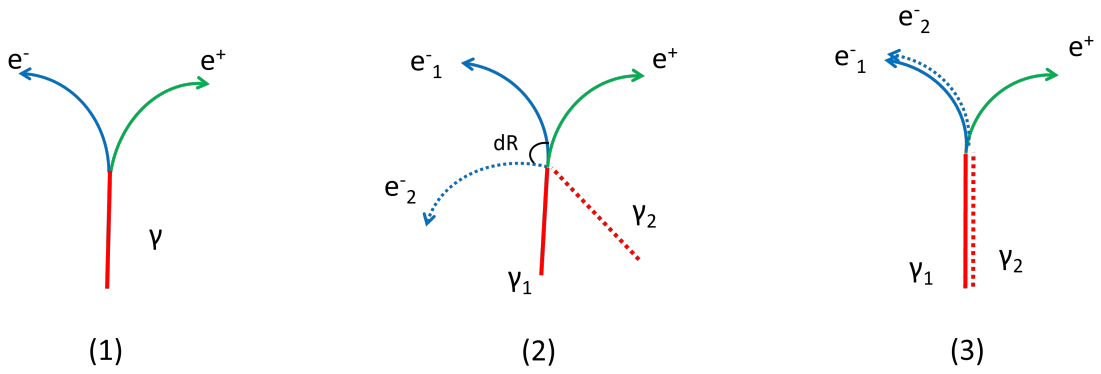

Figure 5.2: **Duplicate conversion removal - example cases: (1)** Regular conversion. The conversion does not share any track with another conversion and is kept. **(2)** Two conversions share a single track (e.g. positron). However, the other track is sufficiently different. This case is regular combinatorics, and both conversions are kept. **(3)** Two conversions share a track (e.g. positron). The other tracks are very close in dR and p_{T} (e.g. e_1^- and e_2^- in the figure). The second conversion is likely only an artifact of a track split in the tracker. The conversion whose split track has a lower number of valid hits is removed.

- *compatible inner hits*: The two candidate conversion tracks must have one of the two innermost hits in the same detector layer to reduce the contribution of fake conversions due to soft displaced tracks that are spuriously propagated backwards.

- *dz to the closest primary vertex PV*: The distance between z-position of the primary vertex calculated from the reconstructed conversion (by propagating its momentum backwards) and the z-position of the PV has to be smaller than $dz < 10\,\mathrm{cm}$.

- *min distance of approach in xy-plane*: $-10\,\mathrm{cm} < dca$. The conversion distance of minimum approach in the xy (transverse) plane, dca, must satisfy the condition -10 cm $< dca$, where dca is the distance between the centers of the two circles made by projecting the track helices onto the transverse plane minus the sum of their radii, $dca = d_{O_1-O_2} - (R_1 + R_2)$. In the ideal case, the tracks would point exactly to the common vertex, and $dca = 0$. Due to the uncertainties, the experimental value has

RMS $\approx 0.2\,\text{cm}$. The value can be negative if the two circles overlap. The cut at $-10\,\text{cm}$ removes only conversions with $dca = -999$, which is a placeholder value.

These cuts were derived for the $p+\text{Pb}$ data specifically and this selection is referred to in this dissertation as *loose*. The details of the studies are in Appendix A.

5.1.4 χ_c selection

For each event, the $\chi_c \to J/\psi\,\gamma$ candidates are formed by combining the J/ψ dimuon with the converted photons. The dimuon candidate mass is required to be between 2.9 and 3.25 GeV in order to reduce the contribution from the combinatorial background. The χ_c mass is calculated using the world average of experimentally determined values of the J/ψ mass [114] instead of the invariant mass of the dimuon [$m(\chi) = m(\mu^+\,\mu^-\,\gamma) - m(\mu^+\,\mu^-) + 3.097\,\text{GeV}$[1]]. This improves the χ_c mass resolution by removing the effect of the dimuon resolution.

5.2 Signal fitting

Once we have the χ_c and J/ψ candidates selected, we look at their invariant mass distribution. The candidates contain a mixture of genuine signal, as well as various sources of background that passed the selections (e.g. combinatorial background). We try to disentangle their respective contributions by fitting the mass distributions with a sum of two functions: an appropriate function describing the signal contribution, and another appropriate function for the background. Thus, the uncorrected signal yield can be obtained directly from the fits. Details of the fitting procedure are described in this section, separately for J/ψ (5.2.2) and χ_c (5.2.3), because the details of the fitting differ.

[1]The world average of J/ψ mass is $3.096900 \pm 0.000006\,\text{GeV}$. However, the precision of our analysis is such that the value is rounded to three decimal places without affecting the results.

5.2.1 Division of data (binning)

Eventually, we want to report the χ_c-to-J/ψ ratio as a function of selected variables, in a binning that provides a decent compromise of statistical significance and granularity. The data for fitting are therefore divided into ranges corresponding to the chosen binning and fitted in these subsets. The division is usually trivial, however there are a few nuances for this analysis, which are discussed here.

5.2.1.1 Kinematic variables for χ_c and for the χ_c-to-J/ψ ratio

The main result pursued in this dissertation is the χ_c-to-J/ψ ratio. If J/ψ and χ_c are binned in their "natural" variables [e.g. χ_c in p_{T} (χ_c) and J/ψ in p_{T} (J/ψ)], then the ratio's variable is unclear as it is neither p_{T} (χ_c) nor p_{T} (J/ψ). It was therefore decided to use the kinematic variables of the J/ψ daughter for the χ_c binning. This approach was done in other studies of the same ratio in $p+p$ collisions in CMS and elsewhere, and ensures that the ratio is well defined. Due to the similarity of kinematics between the χ_c and its daughter J/ψ, the difference for χ_c yields is minor. This approach is used throughout the analysis, and is relevant for rapidity y and transverse momentum p_{T}.

5.2.1.2 N_{tracks} definition

The number of tracks is used to quantify the activity of the $p+\mathrm{Pb}$ collision, and is similar to the centrality variable that is used in $\mathrm{Pb}+\mathrm{Pb}$ collisions. However, the correlation between N_{tracks} and the interaction impact parameter is much weaker in the $p+\mathrm{Pb}$ collisions than it is between the centrality variable and the impact parameter in $\mathrm{Pb}+\mathrm{Pb}$. This is caused by the nature of the collision. There are only about 15 binary collisions in a "central" $p+\mathrm{Pb}$ interaction with impact parameter of ~ 0, compared to ≈ 2000 in $\mathrm{Pb}+\mathrm{Pb}$ [115], and the random fluctuations play a much larger role. Therefore, we usually talk about event

"activity" rather than "centrality" when discussing $p + \mathrm{Pb}$ collisions.

There are several reasonable definitions for the number of tracks that we could use:

1. N_{tracks} **in event:** The CMS reconstruction software provides this variable. It corresponds to the number of tracks passing the quality cuts that are associated with the largest primary vertex (PV) in the event. The quality cuts are: track is required to be of high purity, track $p_{\mathrm{T}} > 0.4\,\mathrm{GeV}$, $|\eta| < 2.4$, relative p_{T} resolution (as estimated from the track fit) better than 0.1, and 3-sigma compatibility with the PV in xy- and z-directions. The main advantage of the variable is that it is readily available, and provides a good estimate of the multiplicity-related conditions in the detector. The downside is that if the χ_c or J/ψ did not originate in the largest PV, a wrong producing collision is assigned to it. This is most relevant to particles of interest originating in low-activity events. Because of pile-up, there is a decent probability of another collision in the same bunch crossing, which is likely to have larger N_{tracks}, and the particle would be assigned to it instead. For this reason, the next two options were developed.

2. N_{tracks} **in dimuon PV:** The first improvement was to use the number of tracks originating from the PV that is associated with the dimuon, which is information that is also readily available from the CMS software. However, no quality cuts are applied, which inflates the number of tracks by about 10%.

3. N_{tracks} **in dimuon PV, quality cuts:** This option is not available by default, and needed to be implemented at the analysis level. We loop over the tracks associated with the dimuon PV, and apply the same quality criteria as is done for "N_{tracks} in event". The resulting number is then stored as a value for the dimuon.

The difference between the first and third option is shown in Fig. 5.3. The figure shows the distribution of the number of tracks for each J/ψ candidate which passes all the selection

criteria and is in the right mass range[2]. N_{tracks} in event is shown in red. Blue and green lines are N_{tracks} in dimuon PV with quality cuts. The difference between the green and blue curves is the method used to associate the dimuon with a PV. Since the green and blue are almost identical, details of the matching between the dimuon and PV are irrelevant, and the blue curve was used.

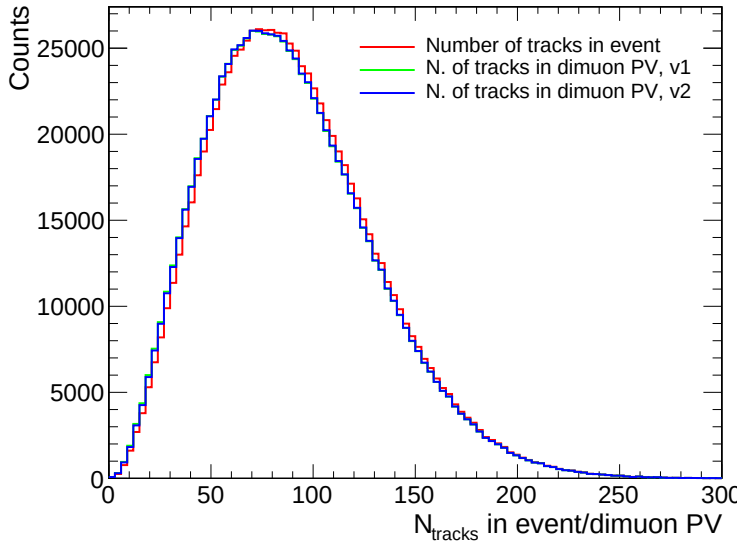

Figure 5.3: N_{tracks} distributions for different definitions of N_{tracks} that were considered.

There has not been an established decision within the HI dilepton group which definition of N_{tracks} to choose. We decided to use the "N_{tracks} in PV associated with the dimuon, with selection", because it describes the physics of the χ_c-producing interaction the best, while maintaining compatibility with the "N_{tracks} in event" variable (in most cases, the dimuon PV is the largest PV, and the values are identical). This variable is referred throughout the text simply as N_{tracks}.

[2]Approximately 90% of such a sample should consist of good J/ψ, since the background is rather small.

5.2.1.3 Combining $p + \mathrm{Pb}$ and $\mathrm{Pb} + p$ directions - rapidity

When combining the $p + \mathrm{Pb}$ and $\mathrm{Pb} + p$ parts of the overall data sample, care needs to be taken in how to treat rapidity. There are two possible options for how to combine both portions of the run:

1. **Adding directly in y_{lab}:** The directions are combined with values of rapidity in the lab frame left intact. That means that the same rapidity value always describes the same region of the detector. This is ideal for exploring whether or not there are any asymmetries in the detector, as any such detector-related effects will also show in the combined data set. The downside is that the positive rapidity for the first part of the run denotes the Pb-going direction, while for the second part it denotes the p-going direction. Thus, any effects related to the actual physical system are obscured in the combined data set.

2. **Flipping $\mathrm{Pb} + p$:** The data sets are combined with the p-going direction defined as positive y (i.e. the rapidity for the $\mathrm{Pb} + p$ portion of the run is flipped). In contrast to the other option, this definition tends to obscure any detector effects, while preserving physics related p/Pb effects.

The main purpose of this dissertation is to report on the physics effects, therefore the second method is primarily used, and in all the physics results the rapidity is defined with respect to the proton beam rather than the lab coordinate system. However, all the plots where we are concerned with the detector (e.g. efficiency and acceptance) are reported in the unflipped lab rapidity. The rapidity is specified in cases where there could be confusion. In such cases, we denote the flipped version as $y_{\mathrm{lab},p}$, and the pure lab-frame rapidity as y_{lab}.

Center-of-mass rapidity The center-of-mass is not at rest for p+Pb collisions, but rather is traveling in the direction of p beam with $y_{\mathrm{CM}} = y_{\mathrm{lab},p} - 0.465$. This is caused by the LHC

using the same strength magnetic field for bending both the p and Pb beams, as the same dipole provides the field for both beam pipes. Because the bending force is proportional to charge, but the required centripetal force is proportional to mass, the Pb beam is bent less than the p beam at the same energy, proportionally to the charge-to-mass ratio Z/A. To offset this difference, the Pb beam is kept at a lower energy. The nominal energy for the p beam is 6.5 TeV, and the energy of the Pb beam is $6.5\,\text{TeV} \times Z/A = 6.5\,\text{TeV} \times 82/208 = 2.56\,\text{TeV}$ per nucleon, ensuring that both beams follow a trajectory of the same radius. The side effect is the aforementioned center-of-mass rapidity offset.

5.2.1.4 Overview of binning

Binning set	**Variable**	**Subrange**	**Bin edges**
Number of tracks	N_{tracks}	Integrated	0, 50, 100, 150, 250
Rapidity	$y_{\text{lab},p}$ (J/ψ)	Integrated	-2.4, -1.6, -1.0, 0, 1.0, 1.6, 2.4
Transverse mom.	p_{T} (J/ψ)	Integrated	6.5, 9, 12, 18, 30 [GeV]
Backward rapidity p_{T}		$-2 < y_{\text{CM}}(J/\psi) < -1$	
Midrapidity p_{T}	p_{T} (J/ψ)	$-1 < y_{\text{CM}}(J/\psi) < 1$	6.5, 9, 12, 18, 30 [GeV]
Forward rapidity p_{T}		$1 < y_{\text{CM}}(J/\psi) < 1.935$	

Table 5.2: Overview of the divisions of data that are used in this analysis.

The binning chosen for the analysis is outlined in Table 5.2. We divide our results into 6 sets. The division into N_{tracks} and integrated p_{T} is straightforward. The integrated rapidity is presented in bins in the lab frame, covering the whole range of the detector ($-2.4 < y_{\text{lab},p} < 2.4$). The Pb + p direction is rapidity flipped, and the positive $y_{\text{lab},p}$ always refers to the p-going direction. Lastly, we have three sets showing the dependence on p_{T} in a particular rapidity in the center of mass to explore backward (Pb-going), mid, and forward (p-going) rapidity regions. $y_{\text{lab},p}$ and y_{CM} are offset from each other by 0.465 ($y_{\text{lab},p}$ =y_{CM} +0.465) due to the p-beam having higher energy per nucleon. This slightly limits the range in the forward rapidity region, which is constrained by the detector acceptance ($y < 2.4$),

and, thus, does not quite reach the full unit of rapidity. The value of 1.935 is often for clarity rounded to 1.9 in figures and the text.

5.2.2 J/ψ fits

Making the J/ψ fits is relatively easy because the particle is plentiful in the data set and has a very good signal-to-background ratio. Therefore, the fits are performed without any constraints from the Monte Carlo, using the well-trodden dilepton procedure. The J/ψ peak is fitted with the sum of two one-sided crystal ball (CB) functions [116], each defined piece-wise as

$$\mathrm{CB}(m;\mu,\sigma,\alpha,n) = \begin{cases} \mathrm{e}^{-0.5\,t^2} & \text{if } t > -\alpha \\ \mathrm{e}^{-0.5\,\alpha^2}\left[\frac{\alpha}{n}\left(\frac{n}{\alpha}-\alpha-t\right)\right]^{-n} & \text{if } t < -\alpha \end{cases} \tag{5.1}$$

where $t = (m-\mu)/\sigma$. The crystal ball function has a Gaussian core to describe the detector resolution and a one sided tail, which describes radiative decays of J/ψ, where J/ψ decays to $\mu^+\,\mu^-$ and one or more γ's. The photons from these decays are undetected, which manifests in lowered invariant mass for the reconstructed dimuon (i.e. the extended tail). In our fits, we use two CB functions to account for the different resolutions in the various kinematic regions of the detector. The tail parameters, α and n, and the mean, μ, are common to both CB functions, while the width, σ, and the normalization can be different. The background is described by a single exponential function. Figure 5.4 shows example fits for the J/ψ peaks. For the fits, parameters "sigmaRatioJpsi" ($\sigma_{CB2} = \mathrm{sigmaRatioJpsi} \times \sigma_{CB1}$) and "ratioJpsi" ($N_{CB2} = \mathrm{ratioJpsi} \times N_{CB1}$) are introduced. Their purpose is purely technical, to improve the stability of the fits and to extract parameter of interest, raw J/ψ yield "nsigJpsi", directly from the fit. Note the difference in resolution between midrapidity (left panel) and forward rapidity (middle panel), where the width of the peak almost doubles.

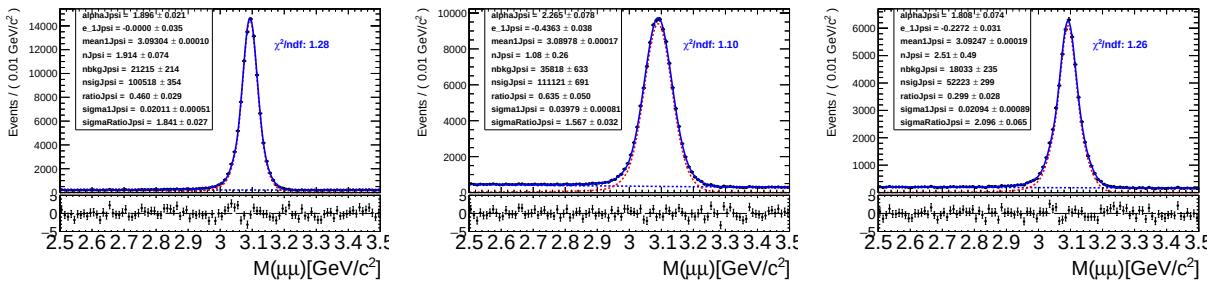

Figure 5.4: Nominal fits to dimuon invariant mass spectrum in the J/ψ region in data. The signal is fitted with two CB functions which share α, n and mean. The background is described by an exponential function. **Left:** Midrapidity ($|y_{\mathrm{CM}}| < 1.0$), lowest p_{T} bin ($6.5 < p_{\mathrm{T}} < 9.0\,\mathrm{GeV}$). **Middle:** Forward rapidity ($1.0 < |y_{\mathrm{CM}}| < 1.9$), lowest p_{T} bin ($6.5 < p_{\mathrm{T}} < 9.0\,\mathrm{GeV}$). **Right:** High multiplicity bin (150 < number of tracks in PV < 250), p_{T} and rapidity integrated.

5.2.3 χ_c fits

Compared to the J/ψ, fitting χ_c is much more challenging, and several steps had to be taken to obtain good-quality fits.

5.2.3.1 Signal model

The chosen fitting model uses a double-sided crystal ball function (DCB), which is an extension of the CB function (see Eq. (5.1)) with tails on both sides. It has been seen in previous CMS χ_c and χ_b analyses that the simulated signal shapes also show a small tail on the high-mass side of the peak, an observation corroborated by our MC. The origin of the high-mass tail was not investigated. We attempted to use a single-sided CB in order to reduce the number of parameters, however the description was not satisfactory.

The full definition of the DCB function is

$$\mathrm{DCB}(m;\mu,\sigma,\alpha_L,n_L,\alpha_H,n_H) = \begin{cases} \mathrm{e}^{-0.5\,t^2} & \text{if } -\alpha_L < t < \alpha_H \\ \mathrm{e}^{-0.5\,\alpha_L^2}\left[\frac{\alpha_L}{n_L}\left(\frac{n_L}{\alpha_L} - \alpha_L - t\right)\right]^{-n_L} & \text{if } t < -\alpha_L \\ \mathrm{e}^{-0.5\,\alpha_H^2}\left[\frac{\alpha_H}{n_H}\left(\frac{n_H}{\alpha_H} - \alpha_H + t\right)\right]^{-n_H} & \text{if } t > \alpha_H \end{cases} \tag{5.2}$$

where $t = (m-\mu)/\sigma$. The subscripts L and H refer to the low-mass and high-mass tail parameters.

The DCB function has a total of seven parameters (μ and σ for the core, $\alpha_{L/H}$ and $n_{L/H}$ for the low/high-end tail, and the overall normalization). Because we fit two peaks of χ_{c1} and χ_{c2}, and the background description is non-trivial, there are too many parameters for a free fit. Therefore we needed to constrain some of the parameters. For that purpose, a MC sample was used.

5.2.3.2 MC constraints

We used the official MC (as described in Section 4.2) to constrain the parameters of the signal. In the MC, we can distinguish between χ_{c1} and χ_{c2}. Therefore, the MC sample is divided into one data set for each of the two states, and each peak is fitted in a simultaneous fit with a single DCB function for each state, where the individual DCBs share several parameters: the tail parameters α_{L}, n_{L}, α_{H}, and n_{H} are constrained to be the same for the χ_{c1} and χ_{c2} peaks, under the assumption that the tails for each peak follow the same shape. Furthermore, the peak width, σ, is constrained to $\sigma_{\chi_{c2}} = (M(\chi_{c2}) - M(J/\psi))/(M(\chi_{c1}) - M(J/\psi)) \times \sigma_{\chi_{c1}} = 1.11\,\sigma_{\chi_{c1}}$, where the masses are from PDG [29]. The peak-width scaling follows from the previous $p+p$ study. All of these constraints were checked so as to not to compromise the quality of the fits. The remaining parameters (peak position, μ, and the overall normalization) are kept separate for each peak. The fits are performed in each of

the bins considered for this analysis, and all peak shape parameters are recorded. The MC samples thus fitted are weighted in N_{tracks}, p/Pb direction, and p_{T} (J/ψ) (see Section 4.3 for details).

Figure 5.5 shows examples of the fits as described above, in different kinematic bins. The red points correspond to the χ_{c1} peak, the green to the χ_{c2}. The goodness-of-fit measure χ^2/ndf is shown for each fit, where χ^2 is the sum of the squares of the pulls for all bins, $\chi^2 = \sum ((y - f_y)/\sigma_y)^2$ and ndf is number of degrees of freedom calculated as the number of bins minus number of the fit parameters. The pull for a given bin is the distance of a point y value from a fit function's value f_y in that bin, expressed in number of standard deviations, σ_y, for that point $((y - f_y)/\sigma_y)$. The bottom panel of each plot shows the pulls. The fits are chosen to be a representative sample. Each figure shows the parameter values, which are then used to constrain fits to real data. Only parameter values are propagated; statistical uncertainties are not used.

5.2.3.3 Background model

The background description is rather challenging because the χ_c invariant mass distribution contains a lot of background in addition to signal, as well as a kinematic turn-on. Moreover, the shape of the background changes depending on the kinematic region where the fit is performed. Several options were explored, and, at the end, a *threshold* function is used, defined as

$$\text{BKG}(m) = (m - q_0)^{\alpha_1} \cdot e^{(m-q_0)\cdot\beta_1} \tag{5.3}$$

where α_1 and β_1 are free parameters, and q_0 is fixed to 3.2 GeV. The exponential term describes the combinatorial background, with β_1 constrained to be negative. The first term describes the kinematic threshold. The q_0 is the position where the turn-on starts. Its value in free fits tended to settle at 3.2 GeV, which is close to the kinematic threshold for the decay

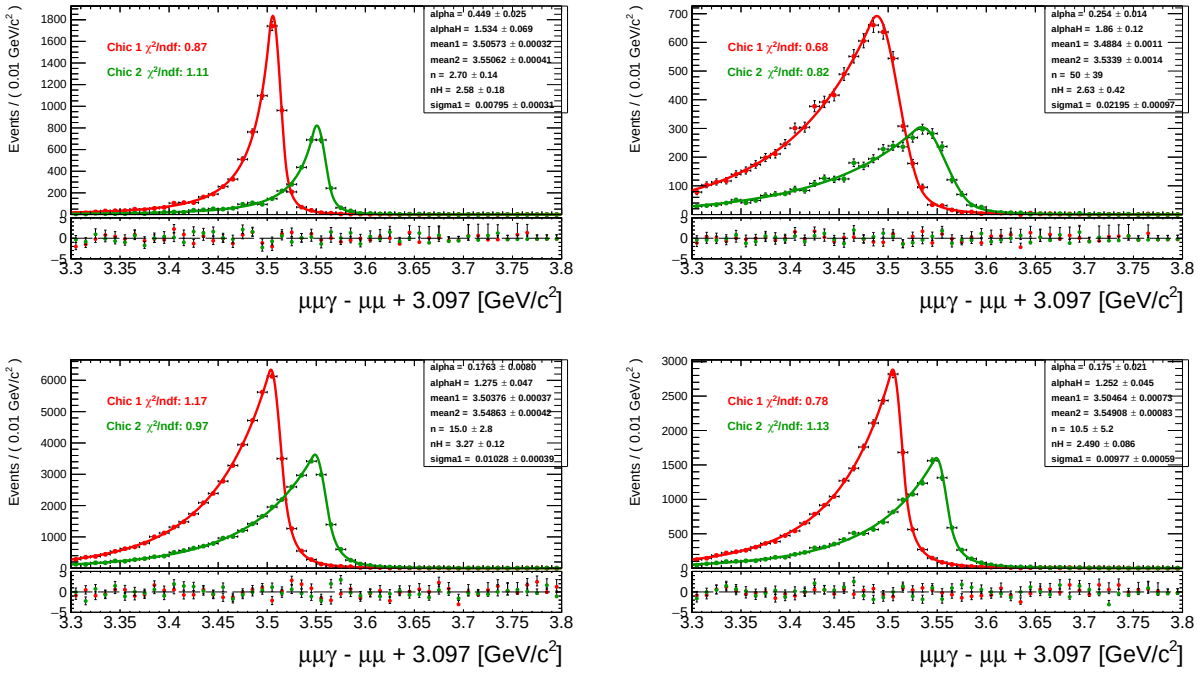

Figure 5.5: Examples of simultaneous fits to two χ_c peaks in MC. Each peak is fitted with a DCB function. See the text for a detailed description of the fitting procedure. **Top row:** Comparison of the resolution in different rapidity regions. Left: midrapidity ($|y_{\mathrm{CM}}(J/\psi)| < 1.0$), third p_{T} bin ($12 < p_{\mathrm{T}}(J/\psi) < 18\,\mathrm{GeV}$). Right: forward rapidity ($1.0 < |y_{\mathrm{CM}}(J/\psi)| < 1.9$), third p_{T} bin ($12 < p_{\mathrm{T}}(J/\psi) < 18\,\mathrm{GeV}$). **Bottom:** Examples of multiplicity bins. Left: $0 < N_{\mathrm{tracks}} < 50$. Right: $100 < N_{\mathrm{tracks}} < 150$.

given that the mass of J/ψ is assumed to be 3.097 GeV and the decay photon has a minimal $p_{\mathrm{T}}(\gamma)$ requirement of 0.5 GeV. Therefore, the value was fixed to improve the fits stability. The threshold function was used in previous χ_c and χ_b analyses in $p+p$ collisions, and it was found to be applicable in $p+\mathrm{Pb}$ too. It describes the shape of the background well while having a reasonably low number of parameters.

5.2.3.4 Data fits

The overall fit function is defined as

$$N_{\chi_{c1}} \cdot \mathrm{DCB}_{\chi_{c1}}(m) + N_{\chi_{c2}} \cdot \mathrm{DCB}_{\chi_{c2}}(m) + N_{\mathrm{bkg}} \cdot \mathrm{BKG}(m) \tag{5.4}$$

The fit has two DCB functions (defined in Eq. (5.2)), one for χ_{c1} and one for the χ_{c2} peak, and a threshold function BKG (defined in Eq. (5.3)) to describe the background. The parameters of the DCB functions are constrained as outlined in Section 5.2.3.2. Therefore, the overall fit has five free parameters: $N_{\chi_{c1}}$ and $N_{\chi_{c2}}$ for the signal, and α_1, β_1, and N_{bkg} for the background. For practical reasons, Eq. (5.4) is rewritten as $N_{\chi_{c1}+\chi_{c2}} \cdot (\mathrm{DCB}_{\chi_{c1}}(m) + c2_{\mathrm{ratio}} \cdot \mathrm{DCB}_{\chi_{c2}}(m)) + N_{bkg} \cdot \mathrm{BKG}(m)$ for the actual fits. Thus, the overall raw signal yield and the ratio $N_{\chi_{c2}}/(N_{\chi_{c1}} + N_{\chi_{c2}})$ are extracted directly from the fit. Figures 5.6, 5.7, and 5.8 show the example fits for N_{tracks}, rapidity, and p_{T} binning, respectively. The overall fit is shown in blue, individual peak DCB functions are shown in red for χ_{c1} and green for χ_{c2}. The dashed blue line is background. The χ^2/ndf of the overall fit is also shown, and the bottom panel shows the pulls. In all the cases the raw yield is statistically different from zero. There are a few cases where the $N_{\chi_{c2}}/(N_{\chi_{c1}} + N_{\chi_{c2}})$ ratio is consistent with zero, indicating that the yield of the χ_{c2} state in that bin is not statistically significant (e.g. right panel of Fig. 5.6).

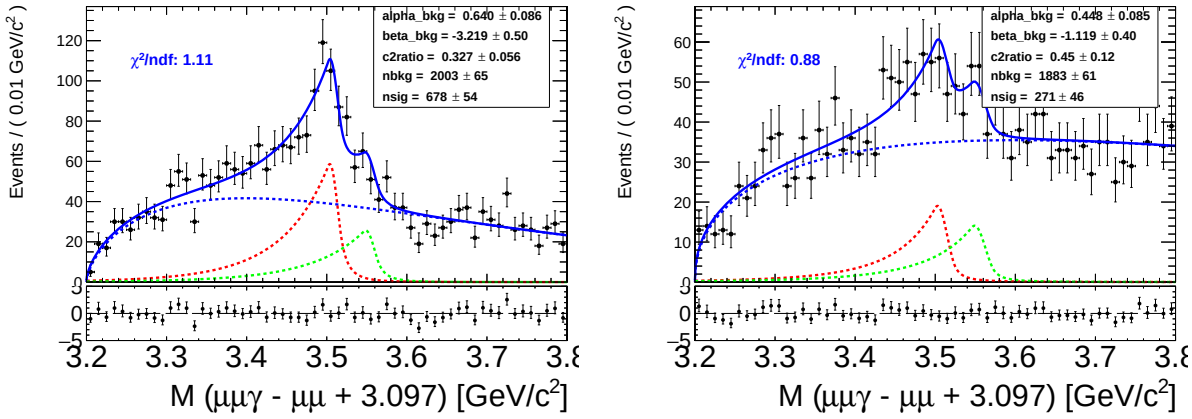

Figure 5.6: Examples of χ_c fits for N_{tracks} binning (p_{T} and rapidity integrated). Each peak is fitted with a DCB function, and the threshold function is used to describe the background. **Left:** Lowest multiplicity bin ($0 < N_{\text{tracks}} < 50$). **Right:** Highest multiplicity bin ($150 < N_{\text{tracks}} < 250$).

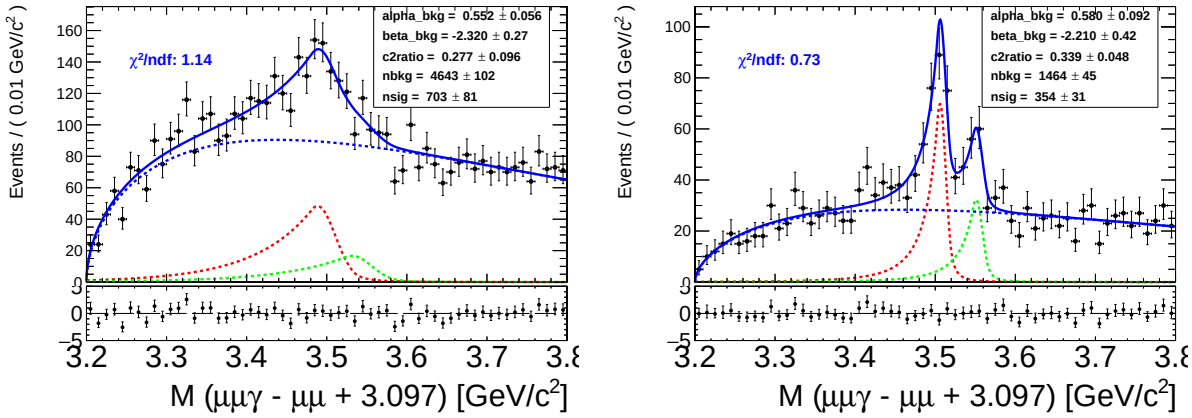

Figure 5.7: Examples of χ_c fits for $y_{\text{lab},p}$ binning (p_{T} and N_{tracks} integrated). **Left:** Most-backward rapidity bin ($-2.4 < y_{\text{lab},p} < -1.6$, corresponding to $-2.865 < y_{\text{CM}} < -2.065$). **Right:** Midrapidity bin ($0 < y_{\text{lab},p} < 1.0$, $-0.465 < y_{\text{CM}} < 0.535$).

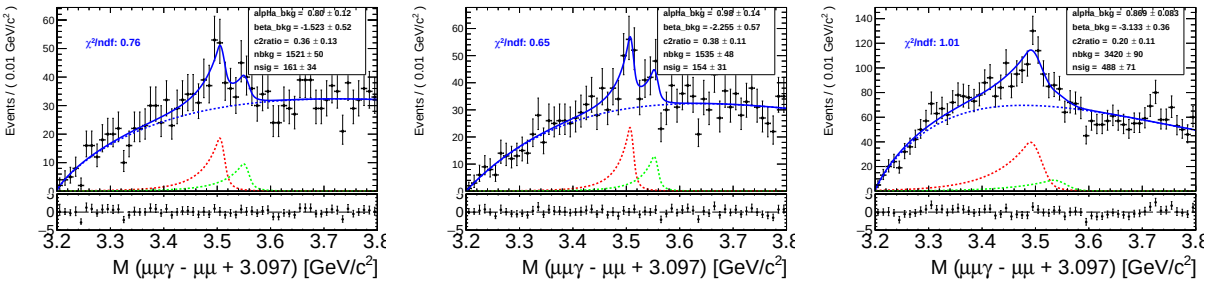

Figure 5.8: Examples of χ_c fits for p_{T} binning for various subranges in y_{CM}. Lowest p_{T} bin ($6.5\,\mathrm{GeV} < p_{\mathrm{T}} < 9\,\mathrm{GeV}$) is shown in all three cases, as it has the most challenging background description. **Left:** Backward rapidity($-2.0 < y_{\mathrm{CM}} < -1.0$). **Middle:** Midrapidity($-1.0 < y_{\mathrm{CM}} < 1.0$) **Right:** Forward rapidity ($1.0 < y_{\mathrm{CM}} < 1.9$).

Chapter 6

Efficiency and acceptance corrections

6.1 Overview of the corrections

Once we have raw, uncorrected yields, we need to correct them for efficiency and acceptance effects originating from the fact that this is an experimental measurement. The relevant particle selections were discussed in Section 5.1, in this chapter the corrections are examined. The single-particle acceptance is explored in Section 6.2, and the efficiency in Section 6.3. It is important to note that the final result is the χ_c-to-J/ψ ratio, where most of the corrections cancel out. The final corrections for the ratio are taking full advantage of this cancellation, and are calculated directly (Section 6.4). Therefore, the acceptance and efficiency results shown in Sections 6.2 and 6.3 are effectively supplemental, since they do not enter in the final results. However, the single-particle acceptances and efficiencies are an important crosscheck of the validity of the particle selections and results, as well as of the quality of the Monte Carlo. As such, they need to be explored.

6.2 Single particle acceptances

The acceptance $\mathcal{A}$ is defined as the ratio of particles of a given type, which pass all our acceptance selections, to all the particles coming from the interaction in a given phase-space region. In essence, it is the fraction of particles that go into an active volume of the detector either directly, or if they decay, the fraction of those particles where all their decay products go into the active volume. The acceptance is usually explored in MC, and shown in bins to obtain a better picture (as a single particle is always either in or out of the acceptance). The overall J/ψ and χ_c acceptance is defined as the ratio of J/ψ (χ_c) whose decay products are passing our acceptance cuts,

$$\mathcal{A}(\text{bin}) = \frac{N_{\text{pass}}(\text{bin})}{N_{\text{gen}}(\text{bin})} \tag{6.1}$$

where $N_{\text{pass}}(\text{bin})$ is the number of particles that passed the acceptance selection in a certain phase-space bin, and $N_{\text{gen}}(\text{bin})$ is the number of generated particles for the bin.

In the case of muons and photons, the acceptance is trivial - a particle of certain p_{T} and η is either always accepted or not[1]. Therefore, the acceptance for muons and photons is either 1 or 0.

6.2.1 J/ψ and χ_c acceptance

The overall $\mathcal{A}$ would be the ratio to all the particles coming from the interaction (as modeled by the MC). However, it is not calculated for two reasons:

- **Limitations of the MC generation:** In order to obtain overall acceptance, we have to generate MC sample without any constraints in order to obtain as realistic a distribution of created particles as possible. However, that also means generating

[1]It is customary in CMS to consider acceptance only in terms of kinematic acceptance selection. The effects that could also be reasonably regarded as a part of the acceptance (e.g. muon decaying and therefore never reaching the detector, or detector having a missing or dead non-responsive volume) are considered under the efficiency instead. The CMS convention is followed in this work.

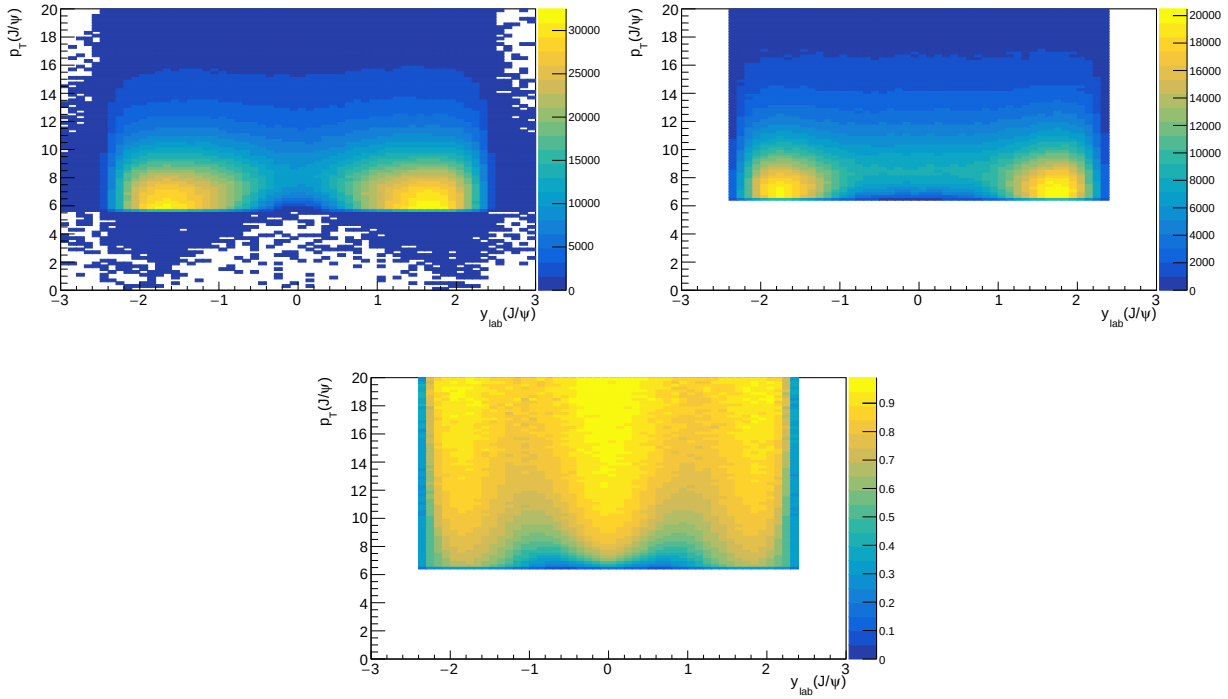

Figure 6.1: Acceptance plots for J/ψ, as a function of y_{lab} and p_{T} (J/ψ). **Top left:** Distribution of generated J/ψ including pre-filter (see text for details). **Top right:** J/ψ passing acceptance cuts, including acceptance cuts on the daughter muons. **Bottom:** Acceptance of J/ψ (specific to our MC).

many particles that we know will not be in the acceptance and, thus, will not be reconstructed (e.g. with $y_{\text{lab}} = 5$ and $p_{\text{T}} \approx 0\,\text{GeV}$). This is very inefficient, and the MC samples have a set of pre-filters generating only decays with interesting kinematics (see Section 4.2 for details).

- **Superfluousness:** The above limitation could be circumvented with a smaller MC sample containing only generator (e.g.PYTHIA) information. However, since we report the χ_c to J/ψ ratio in the J/ψ fiducial region only, the acceptance correction largely cancels out. The only acceptance correction that is applied is a correction for the fraction of γ from χ_c decays that were not in the photon acceptance. This is explored

in Section 6.4.

It needs to be understood that the acceptance plotted in Figs. 6.1 and 6.2 is not an overall acceptance due to the above mentioned limitations. Nonetheless, it is still useful to plot the J/ψ and χ_c acceptance and the $\mathcal{A}$ numerator and denominator distributions, because it serves as an effective crosscheck of the MC sample. In both figures, the effects of the pre-filters are clearly visible in the denominator plot (top left panel) as the cut-offs for p_{T} and y_{lab}. The few scattered particles beyond the cut-offs come from post-filter effects and additional particles from the background samples, and their counts are very low. The bulk of the simulated data post-filter lies in the acceptance, and the ratio of passing J/ψ (χ_c) is reasonable for the MC sample.

6.3 Single particle efficiencies

The efficiency is defined as the ratio of particles passing our selection cuts to all particles that passed the acceptance. Similarly to Eq.(6.1), it is often defined for a given phase-space bin:

$$\mathcal{E}(\mathrm{bin}) = \frac{N_{\mathrm{pass}}(\mathrm{bin})}{N_{\mathrm{acc}}(\mathrm{bin})} \tag{6.2}$$

where $N_{\mathrm{pass}}(\mathrm{bin})$ is the number of particles that passed the efficiency selection in a certain phase-space bin, and $N_{\mathrm{acc}}(\mathrm{bin})$ is the number of particles that were in the acceptance in the same bin. Usually, the kinematic variables for the efficiency, both numerator and denominator, would be the generated MC values, as those are considered the "true" values for the particle. However, we use reconstructed kinematic values in the numerator. Thus construed efficiency includes not only efficiency proper, but also adds the detector resolution correction. For the particles considered in this analysis, the resolution effects are small, and thus, the difference between using reconstructed or generated values in the numerator is slight.

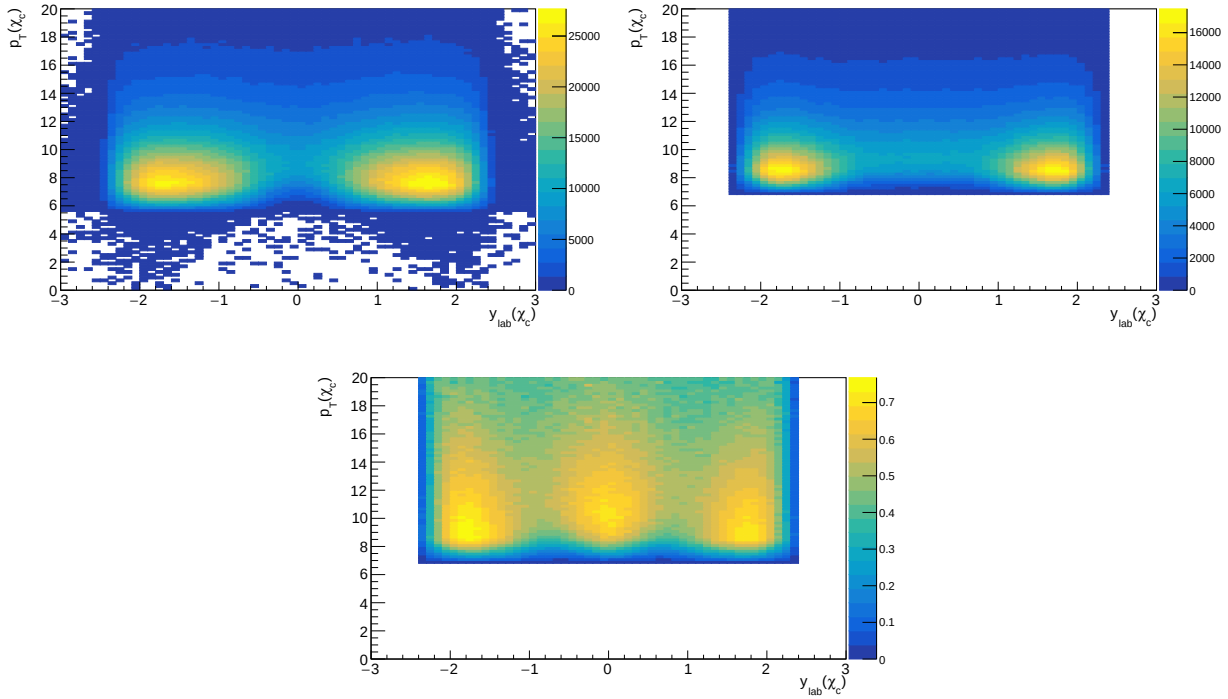

Figure 6.2: Acceptance plots for χ_c, as a function of y_{lab} and p_{T} (χ_c). **Top left:** Distribution of generated χ_c including pre-filter (see text for details). **Top right:** χ_c passing acceptance cuts, which are acceptance cuts on daughter J/ψ, muons, and photon (no direct cut on χ_c). **Bottom:** Acceptance of χ_c (specific to our MC).

Unlike the acceptance, the efficiency does not depend on the pre-filters applied during the MC generation. On the other hand, a full detector simulation, including the reconstruction, is needed.

Figure 6.3 shows the single muon efficiency. The top left panel displays muons coming from χ_c decays and passing the acceptance selection. The top right panel shows the distribution of muons that also passed the selection (soft identification). The bottom panel is the efficiency (ratio of the two panels above). For most of the region of interest, the muon efficiency is around 80-90%. You can notice two lines around $|\eta| = 0.25$. The lines are visible in the official plots made for 2016 p + Pb run (see Fig. 5.1, for example) and also present

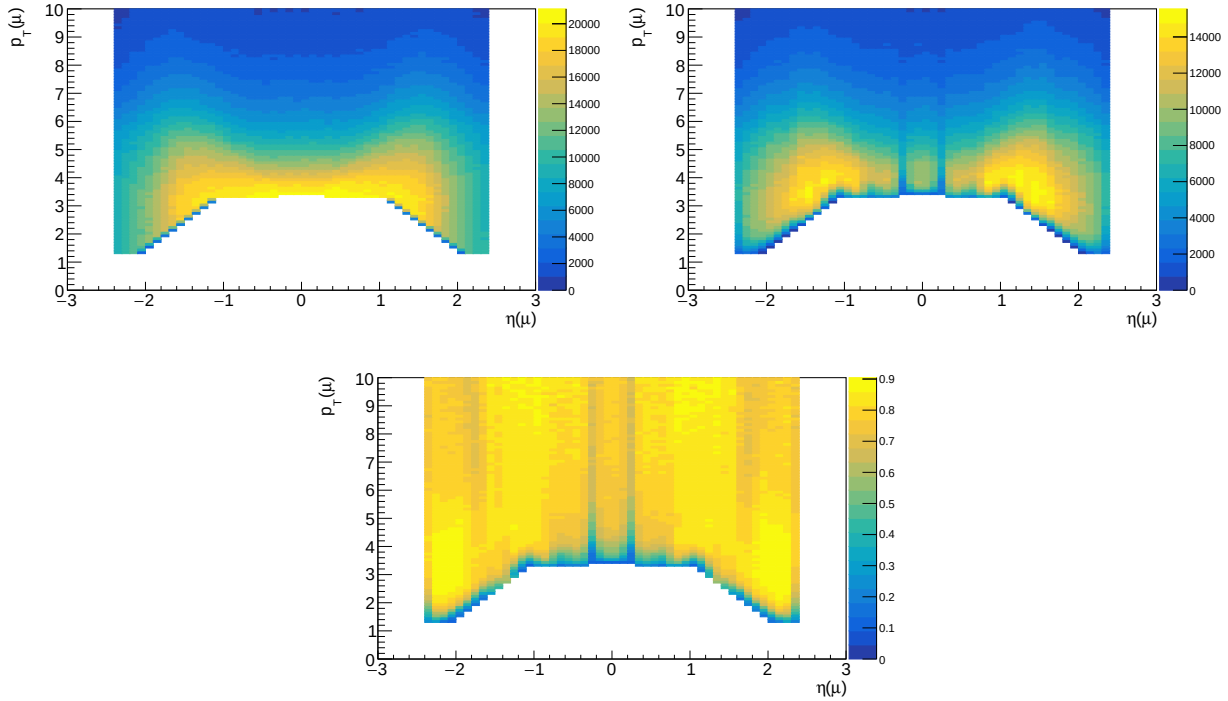

Figure 6.3: Rapidity vs p_{T} plots for the MC muons coming from χ_c decays (through J/ψ). **Top left:** Distribution of generated muons passing acceptance cuts. **Top right:** Distribution of muons passing acceptance cuts and selection (soft ID). **Bottom:** Muon selection efficiency.

in $p+p$ data. They are caused by a region of detector with less redundancy due to the gap between the wheels of iron yoke in the barrel region, and they are well documented [113].

Similarly, Fig. 6.4 shows the distribution of the generated J/ψ coming from χ_c decays and passing the acceptance selection (both for muons and the J/ψ itself), on the top left panel. The top right panel shows the distribution of the J/ψ that also passed the selection (for muons and J/ψ). The bottom panel is the efficiency (ratio of the two) and for J/ψ represents the overall J/ψ reconstruction efficiency. There is a region of lower efficiency at $p_{\mathrm{T}}(J/\psi) \approx 7\,\mathrm{GeV}$ in midrapidity. It is caused by CMS not reconstructing muons below $\approx 3.4\,\mathrm{GeV}$ in midrapidity, which due to the decay kinematics, translates to an inability

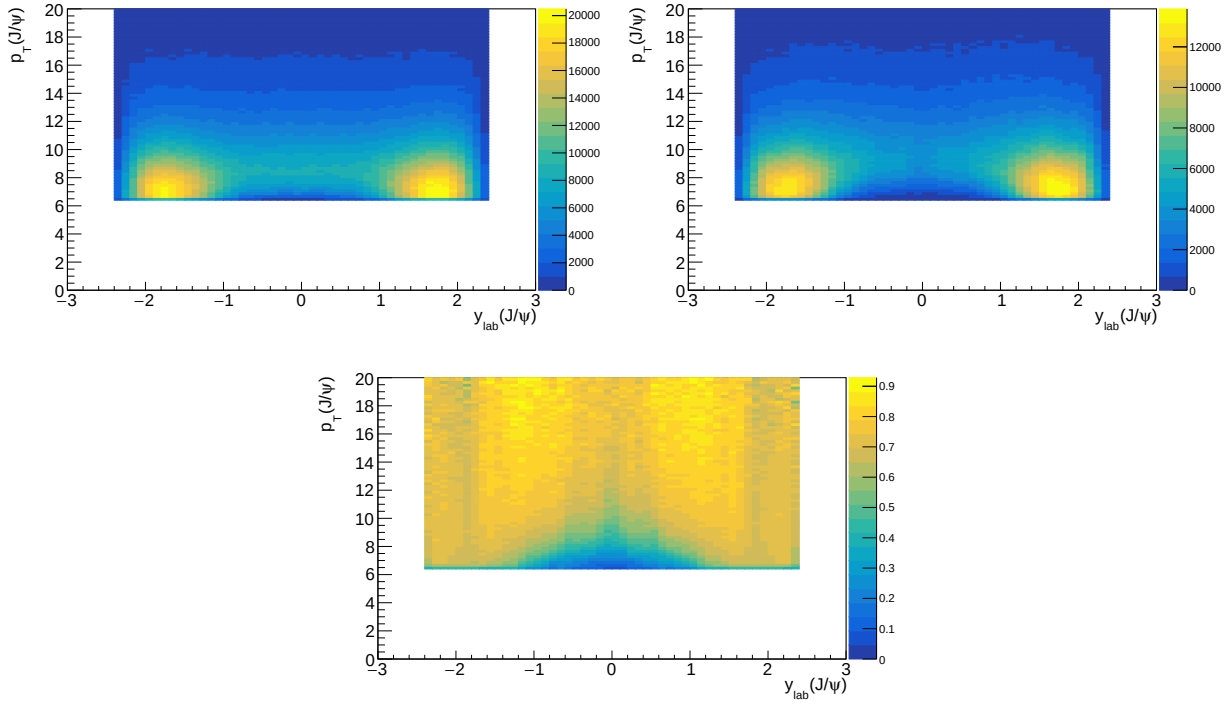

Figure 6.4: Rapidity vs p_{T} plots for MC J/ψ coming from the χ_c decays. **Top left:** Distribution of generated J/ψ passing muon and J/ψ acceptance cuts. **Top right:** Distribution of J/ψ passing acceptance cuts, muon selection (soft ID) and J/ψ selection. **Bottom:** Overall J/ψ selection efficiency.

to reconstruct J/ψ much below 7 GeV. This is the reason why we, as well as other CMS analyses, place the J/ψ p_{T} cut-off at 6.5 GeV. This limitation does not exist for forward rapidity, where it is, in principle, possible to go all the way to p_{T} (J/ψ) of 0 GeV. The possibility to extend the acceptance reach was explored for this analysis. However, the background contribution is dominant in that region. Moreover, the mass resolution for χ_c is worse in forward rapidity than in midrapidity, which, coupled with the background, leads to drowning out the signal.

The top left panel of Fig. 6.5 shows the distribution of generated photons coming from χ_c decays and passing the acceptance selection. The top right panel shows the distribution

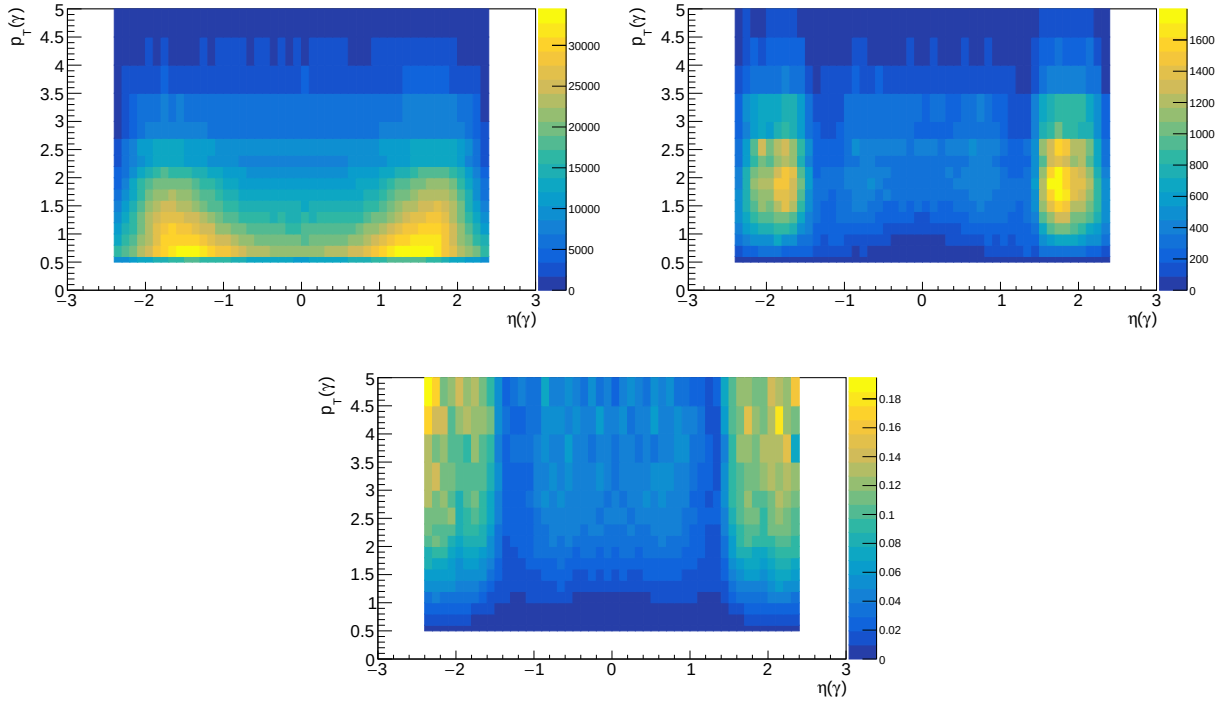

Figure 6.5: Rapidity vs p_{T} plots for MC photons coming from the χ_c decays. **Top left:** Distribution of generated photons passing acceptance cuts. **Top right:** Distribution of photons passing acceptance cuts and selection (loose selection). **Bottom:** Photon selection efficiency.

of photons that additionally passed the analysis selection (loose selection). The bottom panel is the efficiency (ratio of the two). The most notable features are that the selection efficiency is higher in the forward region, and that the efficiency shows a strong p_{T} trend. The inefficiency and the trends are present directly in the reconstructed conversion collection. The probability that the photon appears in the collection includes the efficiency of the reconstruction algorithm, but most importantly, the probability that the photon converts in the first place. The loose selection is $\approx 90\%$ efficient for those photons for which the conversion exists. See Appendix A for details.

Figure 6.6 shows the total χ_c reconstruction efficiency assuming that all the decay prod-

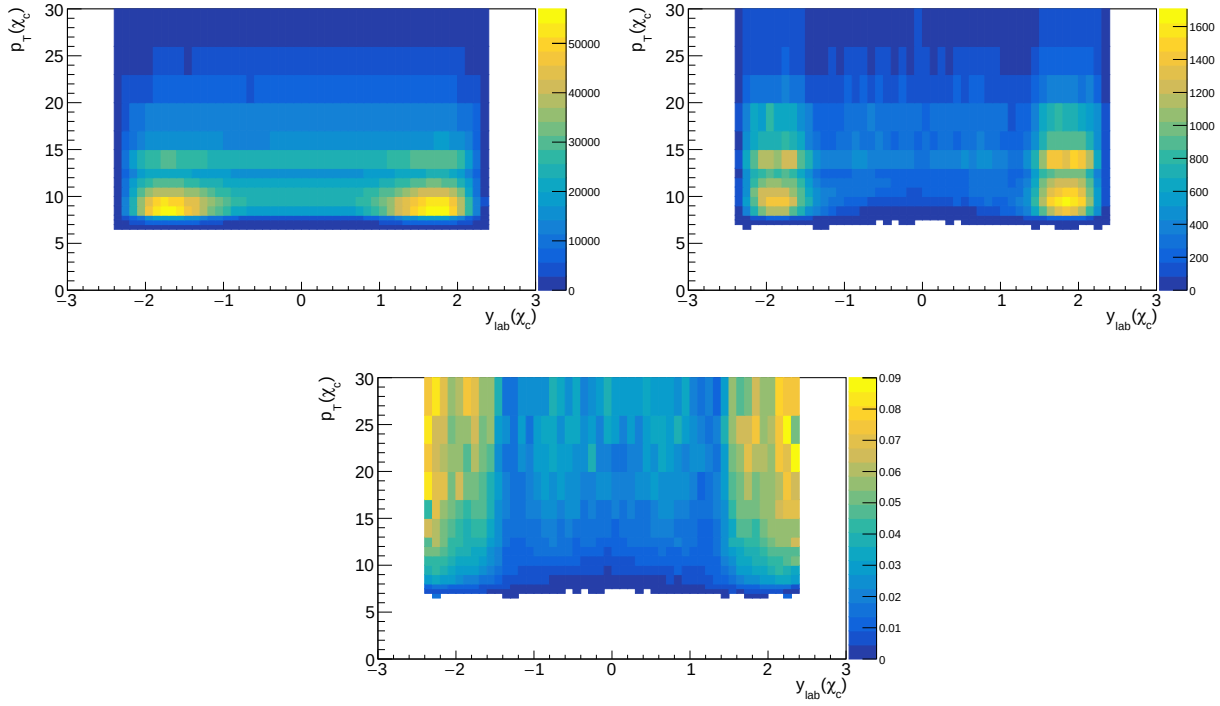

Figure 6.6: Rapidity vs $p_{\mathrm{T}}(\chi_c)$ plots for both χ_c states (combined MC). **Top left:** Distribution of generated χ_c passing all the individual acceptance cuts. **Top right:** Distribution of χ_c passing acceptance cuts and selection for χ_c and all the decay products. **Bottom:** Overall χ_c selection efficiency.

ucts are in the acceptance as defined in Section 5.1. The top left panel shows the distribution of all the χ_c where the decay products are in the acceptance. The top right panel shows the distribution after all the selections were applied. The bottom panel shows the total reconstruction efficiency for χ_c. The fuzzy bottom edge is indirectly caused by the fact that we do not have a specific acceptance cut on χ_c itself. The phase space for χ_c is thus similar to J/ψ, but with additional smearing due to the decaying photon, which, due to the low $(\chi_c - J/\psi)$ mass difference, does not change the χ_c kinematics much. This leaves the lowest-p_{T} bins scarcely populated. Note that the bin p_{T}-size varies in order to maintain a decent statistical sample in each bin. This is not corrected in the two top panels (i.e. only

raw counts are recorded), creating an illusion of additional structure around $p_{\mathrm{T}} \approx 13\,\mathrm{GeV}$. There is, obviously, no effect on the ratio.

6.4 Efficiency for χ_c to J/ψ ratio

The overall correction is calculated in a similar fashion as the individual efficiencies. However, the fact that the result is a ratio is taken into account by merging the individual corrections into a single number for each bin. The correction is then the ratio of the probability that we reconstruct the χ_c over the probability that we reconstructed J/ψ. As discussed in Section 5.2.1.1, χ_c uses kinematic variables of its daughter J/ψ. The total efficiency is calculated directly in the analysis bins:

$$\mathcal{E}_{\mathrm{total}}(\mathrm{bin}) = \frac{\mathrm{prob}(\chi_c\,\mathrm{reco.})}{\mathrm{prob}(J/\psi\,\mathrm{reco.})} = \frac{N_{\mathrm{pass}}(\chi_c)(\mathrm{bin})}{N_{\mathrm{pass}}(J/\psi)(\mathrm{bin})} \tag{6.3}$$

$N_{\mathrm{pass}}(\chi_c)(\mathrm{bin})$ is the number of χ_c that we successfully reconstructed, and $N_{\mathrm{pass}}(J/\psi)(\mathrm{bin})$ are successfully reconstructed J/ψ, all originating from our simulated χ_c. Individual muon and J/ψ efficiencies and acceptances cancel out in this ratio, because they are present both in the numerator and in the denominator. The only remaining parts are γ acceptance and selection, and χ_c selection. Fig. 6.7 shows the resulting correction to the χ_c to J/ψ ratio for various analysis bins. In all the plots, the $\mathrm{Pb}+p$ MC data set is flipped with $y_{\mathrm{lab},p} = -y_{\mathrm{lab}}$ in order to have the proton beam always going in the positive y-direction. The p_{T} plot is binned in the center-of-mass rapidity y_{CM}. Since the center-of-mass of the $p+\mathrm{Pb}$ system is shifted by $y = 0.465$ in the p-direction with respect to the lab frame (see Section 5.2.1.3 for details), particles produced in the opposite center-of-mass rapidities (e.g. $y_{\mathrm{CM}} = 1$ and -1) do not decay to the same parts of the detector, even if assuming a completely symmetric CMS experiment. This explains the difference in efficiencies for forward and backwards directions in Fig. 6.7. The center-of-mass forward region is shifted towards the detector

end-caps, where the reconstruction efficiency is higher, while the center-of-mass backward region is shifted towards the barrel region with lower efficiency (but better resolution).

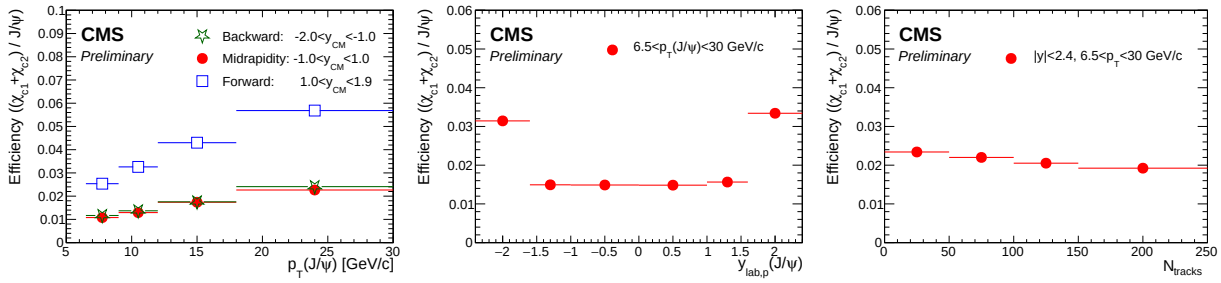

Figure 6.7: The ratio efficiency dependencies are shown for $\chi_{c1+c2}/J/\psi$ samples in $p_{\mathrm{T}}(J/\psi)$ bins for mid, forward, and backward center-of-mass rapidity (left), in rapidity $y_{\mathrm{lab},p}(J/\psi)$ bins (middle) and in number of primary track (right) regions, respectively.

6.4.1 The rationale for the selected approach

There are two standard approaches for correcting the results. The method that is described in this chapter calculates the final correction in the analysis bins, and then uses it to correct raw yields that were obtained independently for J/ψ and χ_c. The other commonly accepted method is to obtain efficiency and acceptance corrections from the MC in some (usually much finer) binning, and then apply $1/\langle\mathcal{A}\cdot\mathcal{E}\rangle$ from the corresponding bin as the weight that is attached to each event in the data. Then, when the signal invariant-mass fits are performed, the resulting yields are already corrected. While this method was briefly tested, we decided not to adopt it for two related reasons. First, the individual weights that would be used for the χ_c and J/ψ invariant-mass fit cannot take advantage of the cancellation of several acceptances and efficiencies. Second, the γ efficiency is low, which leads to large weights $w = 1/\langle\mathcal{A}\cdot\mathcal{E}\rangle$. The weights also vary noticeably among different regions of the detector. The large and varied weights coupled with somewhat low statistics for the χ_c sample then lead to an artificial amplification of point-to-point fluctuations in the invariant-mass distributions.

While the uncertainties on each point are correctly propagated, this, nonetheless, presents an issue for the fits stability, and leads to overestimation of yield uncertainties.

There are two further points to consider for the current correction method:

- **Binning:** Since the method uses the analysis bins, which are somewhat large, it is sensitive to the underlying kinematic and multiplicity distributions. Therefore, it is crucial to guarantee that the MC and data have similar p_{T}, rapidity and N_{tracks} spectra. We therefore weighted the MC data sets as described in Section 4.3.

- χ_c **states:** Both χ_{c1} and χ_{c2} are corrected together with the same correction. It was checked that the efficiencies for the two states are very similar, and the error thus introduced is negligible.

Chapter 7

Systematic uncertainties

As in any experimental measurement, there are various systematic uncertainties affecting the results. One of the main advantages of constructing our results as the ratio of χ_c to J/ψ is that many of the systematic uncertainties cancel out (most notably reconstruction efficiency and acceptance for J/ψ, and luminosity uncertainty). The remaining uncertainties are studied in this chapter in the order used to obtain the results.

7.1 Signal selection

We reconstruct χ_c via decay to J/ψ and γ. The exact selection that is used to select the daughter particles could influence the result. The size of the effect is therefore explored.

7.1.1 Conversion selection

To obtain the systematic uncertainty from the photon conversion, we vary the conversion selection presented in 5.1.3 (nominal = *loose*). The alternate selections that are considered are called *medium* and *very loose*. The *medium* selection is a tighter version of the nominal

loose selection, while the *very loose* selection is less strict. The individual cuts are listed in Table 7.1.

	Very loose	**Loose (nominal)**	**Medium**
conversion quality	isGeneralTracksOnly	isGeneralTracksOnly	isGeneralTracksOnly
compatible inner hits	-	required	required
dz to closest PV	-	$dz < 10\,\text{cm}$	$dz < 10\,\text{cm}$
minimum distance of approach	-	$-10\,\text{cm} < dca$	$-10\,\text{cm} < dca$
track 1 and 2 ndf	-	-	track ndf > 3
conversion vertex probability	-	-	prob > 0.0005

Table 7.1: The three conversion selections used to determine the systematic uncertainty. The selection on the left is looser and that on the right is tighter than the nominal (middle).

The alternative selections were chosen based on the study documented in Appendix A. The *medium* selection is explored there, and the *very loose* selection was newly-formed for this systematic study and chosen to be a reasonable less-strict alternative to the nominal *loose* selection, while still being sufficiently different. The efficiencies of the selections are shown in Fig. 7.1. We see that the selections are adequately varied and distinct from each other.

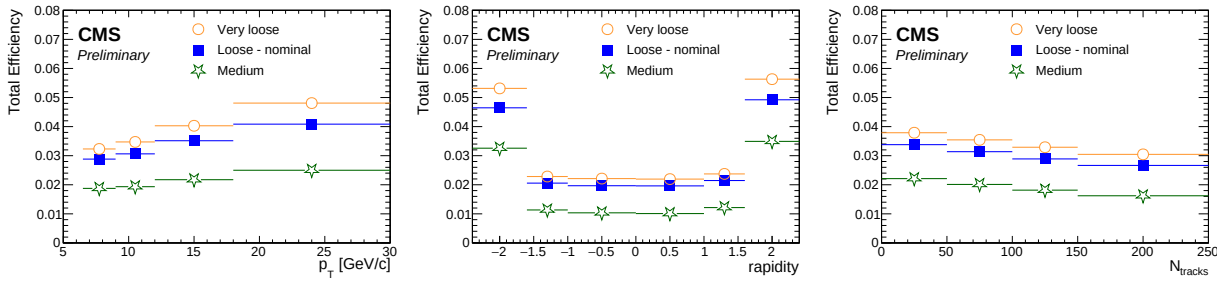

Figure 7.1: Efficiencies for the three conversion selections used in the study of the systematic uncertainty. Left, middle and right plot shows their dependence as a function of p_{T}, rapidity y_{lab}, and number of tracks, respectively.

The uncertainty originating from the photon conversion will not cancel in the $(\chi_c/J/\psi)$

ratio and is expected to be significant. To obtain an estimate of the effect of the conversion selection on our results, the nominal results have been recalculated for each alternative selection, using the nominal analysis procedure. The efficiencies are different enough to affect the shape of the χ_c peak. Therefore, the peak-shape constraints that are obtained from the MC needed to be rederived for each conversion selection. This is part of the normal analysis procedure and is mentioned here for completeness[1]. The effect of the constraints is illustrated in Fig. 7.2. The plot in the left panel is obtained using the simplified procedure assuming the same χ_c peak shape for all the selections, while the right panel is derived using the full procedure for each selection. We can see from the left panel that the results meaningfully change when one keeps the simplifying assumption that the signal shape parameters are the same irrespective of the conversion criteria. Thus, the simplifying assumption does not work and is not used further.

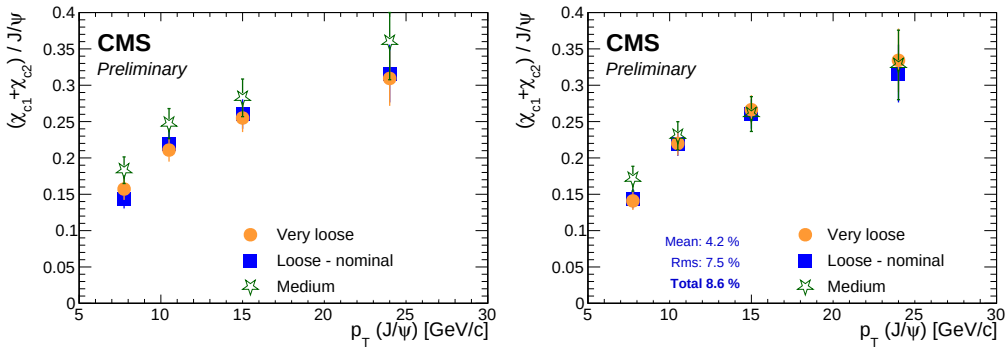

Figure 7.2: **Left:** The results as a function of p_{T} (J/ψ) for the various selections under the assumption that the peak shape stays the same. The results are not used since the assumption does not hold. **Right:** The same results with the full analysis procedure used.

Figure 7.3 shows the overall results for the three different conversion selections. The left panel shows the overall $p_{\mathrm{T}}(J/\psi)$ dependence, the middle shows the rapidity, $y_{\mathrm{lab},p}(J/\psi)$,

[1]The need to rederive the constraints might not be obvious. We originally expected the χ_c shape to be unaffected.

dependence, and the dependence on the number of tracks is shown on the right panel. The results are largely overlapping and consistent with each other, confirming that the conversion selection does not introduce a bias. For each point, the difference between the nominal results (loose selection) and the others is calculated and expressed in percent. Then, for each plot, these differences have their means and RMS values calculated. The values are listed in the figure. The overall uncertainty for the plot is obtained by adding the mean and RMS in quadrature. This procedure mirrors what was done with the toy MC for systematic uncertainty of signal extraction described in Section 7.2. While arbitrary, we believe that the value provides a reasonable estimate of potential variation of the results due to the conversion-cut selection. We avoided using point-by-point variations, which would be dominated by random fluctuations. The resulting uncertainties for $p_{\mathrm{T}}(J/\psi)$, $y_{\mathrm{lab},p}(J/\psi)$, and N_{tracks} are 8.6 %, 15.5 %, and 9.8 % respectively. However, these come from projections of the same total data set, and the differences are unlikely to be meaningful. The values are thus averaged to 11.3 % and rounded to 12 %, which is then used as the flat overall systematic uncertainty due to the conversion selection.

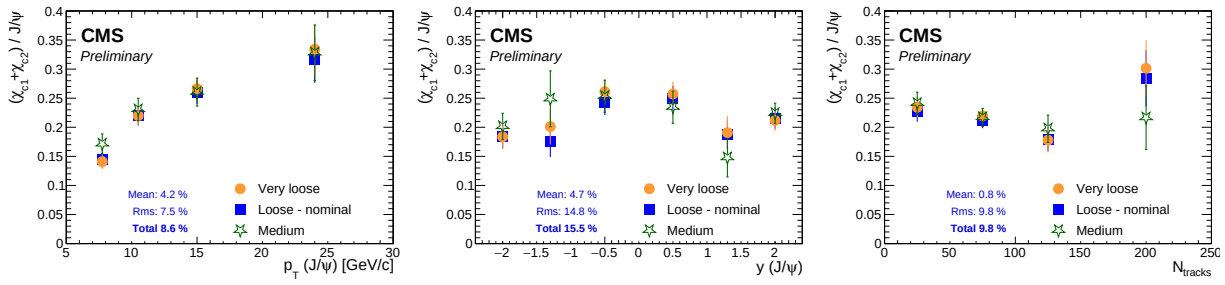

Figure 7.3: The variation of final results for the nominal and alternative conversion selections as a function of $p_{\mathrm{T}}(J/\psi)$, $y_{\mathrm{lab},p}(J/\psi)$, and N_{tracks} in the left, middle, and right panel, respectively. The mean difference of alternative results to the nominal, and its RMS, are included in the plots.

The differences between selections are cross-checked in Fig. 7.4. The figure shows the

variation for the other kinematic ranges that we use in this analysis, in the backward-, mid- and forward-rapidity regions. The 12 % uncertainty derived above seems a reasonable estimate for these results as well.

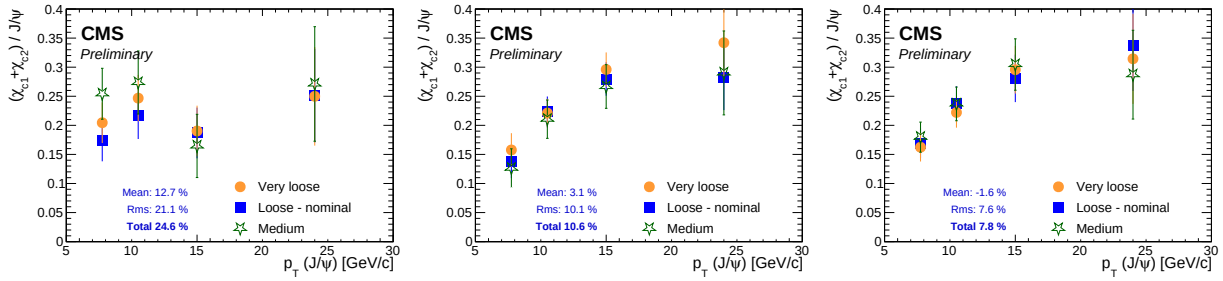

Figure 7.4: The variation in final results for the nominal and alternative conversion selections as a function of p_{T} for different rapidity regions of the colliding system. The ranges are backward rapidity (Pb-going direction, $-2 < y_{\mathrm{CM}} < -1$), midrapidity ($-1 < y_{\mathrm{CM}} < 1$), and forward rapidity (proton-going direction, $1 < y_{\mathrm{CM}} < 1.9$) for the left, middle, and right panel, respectively. The results shown in the plots are used only as a crosscheck.

The uncertainty tested by varying the cuts is not entirely comprehensive, since our results rely on the MC, and the cut systematic tests only part of the MC-derived reconstruction efficiency. The procedure does not test the initial conversion algorithm that is used to obtain the conversion collection (the algorithm is standard for CMS and was used in past analyses). Moreover, the cut variation is more of a consistency cross-check than a proper procedure to obtain the uncertainty. However, there is no other independent procedure to check the MC directly (for example with tag and probe, as is the case for muons). The problem was discussed with the CMS *e-gamma* group representatives without a clear alternative approach emerging. Therefore, the cut variation is used. Despite these reservations, the variation obtained from the different cuts does provide at least a rough estimate of how big the effects from the conversion selection are, and thus gives us a reasonable estimate of the systematic uncertainty.

7.1.2 J/ψ reconstruction

Systematic uncertainties on the extraction of J/ψ are readily available via approved heavy-ion tag-and-probe (T&P) studies done for the HLT_PAL1DoubleMuOpen_v1 trigger and for Soft-muon ID in the kinematic range that we use. There is a recommended procedure to obtain the systematic uncertainty. However, due to the nature of the results (ratio of χ_c to J/ψ, all in kinematic variables of J/ψ), it is expected that the systematic uncertainty due to the J/ψ selection is well under 1%, which is negligible compared to the other sources of systematic uncertainty[2].

7.2 Signal and background models

The uncertainty from our description of the signal and background shape is evaluated using the toy MC pseudodata. This lets us repeatedly sample the differences coming from the different signal and background descriptions, while minimizing the effects of limited statistics. The procedure is as follows:

1. In a given phase-space bin, the nominal fit is performed and recorded.

2. The nominal fit (signal+background) is used to generate toy pseudodata with the same number of overall counts as the real data.

3. The pseudodata are fitted with the nominal fit again, performing the fit in exactly the same manner as if they were the real data. This is then used as the baseline to which the alternative signal and background results are compared.

[2]In fact, the T&P based corrections cancel out exactly in the approach that we use (correcting directly the χ_c-to-J/ψ ratio). However, if we worried about negligible effects, we could consider differences in kinematic distributions between χ_c and J/ψ. Since those distribution are not identical, the T&P corrections to the numerator and denominator would, in principle, need not to be exactly the same. This in turn would mean that the T&P contributions in the ratio might not cancel out exactly. As the T&P corrections themselves are on order of a few percent, and do not show a strong dependence on the kinematic variables, this does not need to be explored.

4. The pseudodata are fitted with the alternative signal. The percent difference in the yield between the alternative and the nominal fit to pseudodata is recorded.

5. The pseudodata are fitted with the alternative background. The percent difference in the yield between the alternative and the nominal fit to pseudodata is recorded.

6. Steps 2-5 are repeated 100 times.

7. The resulting distributions of deviations for the alternative signal and for the alternative background are examined for any abnormalities. The expectation is that they are single peaked with a well-defined mean and RMS. The systematic uncertainty for the signal and background shape is then obtained from the distribution as $\epsilon = \sqrt{(\text{mean}^2 + \text{RMS}^2)}$.

Figure 7.5 illustrates steps 2-5 for two toy MCs in the same bin. The gray line in the figures is the original nominal fit to real data, which are not shown. It is the same for all 100 toy fits. The black points are pseudodata points generated from the gray curve (step 2). The blue line is the fit with the nominal function to the pseudodata (step 3); in these fits it tends to be hidden behind the other curves. The red curve is the fit to pseudodata with the alternative signal description (step 4). And the green is the alternative background description fit (step 5). The toy fits are shown for $6.5 < p_{\text{T}}(J/\psi) < 9.0\,\text{GeV}$, $-1 < y_{\text{CM}}(J/\psi) < 1$ bin. The bottom panel of each figure shows the pulls in the same color scheme as the top panel.

Figure 7.6 illustrates the resulting distribution of deviations from the nominal fit for the example χ_c bin. The left and right plot show identical results. The only difference is that the right plot is zoomed in. The red curve shows the signal variations, the green the background. The example toy fits shown in Fig. 7.5 are included in the distributions as two entries for the signal distribution and two entries for the background distribution. Both distributions

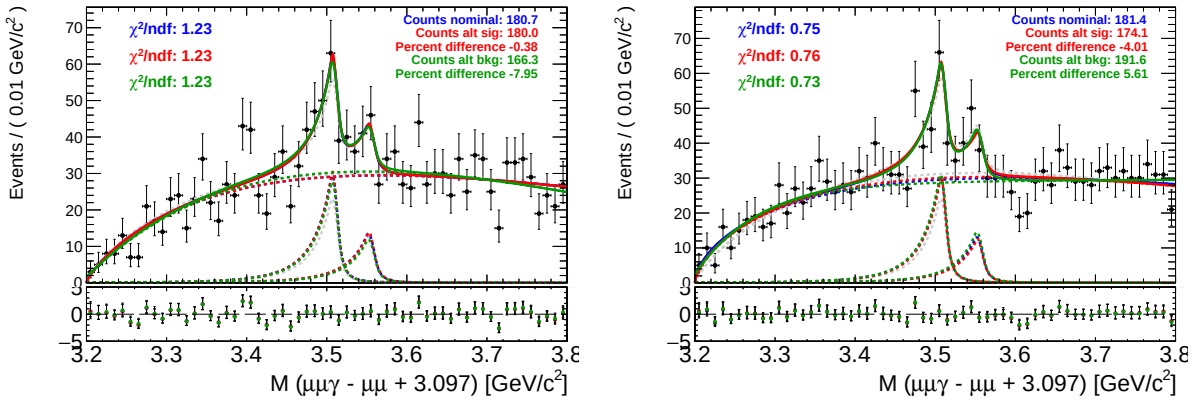

Figure 7.5: Two example toy fits for the same bin for the χ_c systematic uncertainty. The description of the lines is in the text.

are single peaked and well behaved. The overall uncertainty for the signal can be obtained from the mean and the RMS on the right plot ($\sigma_{\text{fit}} = \sqrt{0.13^2 + 0.61^2} = 0.62\%$), and for the background on the left plot ($\sigma_{\text{fit}} = \sqrt{3.1^2 + 9.2^2} = 9.7\%$). Please note that the actual values of the mean and RMS are independent of the binning shown on the plots, and are recorded automatically.

The outlined procedure is used for both J/ψ and χ_c fits.

7.2.1 Alternative signal and background for J/ψ

The alternative fits for the J/ψ peaks are performed directly on data, without constraining the peak shape with MC. This is the same approach as in the nominal case. The alternative signal shape was chosen to be a sum of a Gaussian and a Hypatia function [117]. The

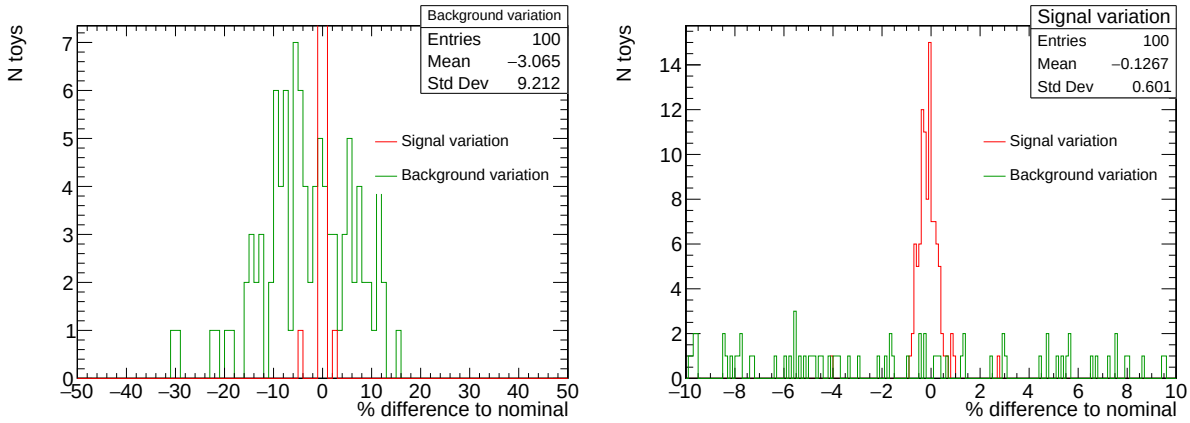

Figure 7.6: Distribution of the percent difference between alternative signal (red curve) and background (green) toy fits for the case of χ_c yield in the first rapidity bin (a more challenging case). Both plots show the same distribution, with the right plot zoomed in.

Hypatia function is defined as:

$$\mathrm{Hyp}(m;\mu,\sigma,\lambda,\zeta,\beta,a_L,n_L,a_H,n_H)\begin{cases} G(m,\mu,\sigma,\lambda,\zeta,\beta) & \text{if } a_L < \frac{m-\mu}{\sigma} < a_H \\ \dfrac{G(\mu-a_L\sigma,\mu,\sigma,\lambda,\zeta,\beta)}{\left(1-\frac{m}{n_L\frac{G(\mu-a_L\sigma,\mu,\sigma,\lambda,\zeta,\beta)}{G'(\mu-a_L\sigma,\mu,\sigma,\lambda,\zeta,\beta)}-a_L\sigma}\right)^{n_L}} & \text{if } \frac{m-\mu}{\sigma} < -a_L \\ \dfrac{G(\mu+a_H\sigma,\mu,\sigma,\lambda,\zeta,\beta)}{\left(1-\frac{m}{-n_H\frac{G(\mu+a_H\sigma,\mu,\sigma,\lambda,\zeta,\beta)}{G'(\mu+a_H\sigma,\mu,\sigma,\lambda,\zeta,\beta)}-a_H\sigma}\right)^{n_H}} & \text{if } \frac{m-\mu}{\sigma} > a_H \end{cases} \tag{7.1}$$

where m is the invariant mass which we fit, and $\mu,\sigma,\lambda,\zeta,\beta,a_L,n_L,a_H,n_H$ are function parameters (five for the core, and two for each of the low- and high-mass tails). The function $G(m,\mu,\sigma,\lambda,\zeta,\beta)$ is defined as

$$G(m;\mu,\sigma,\lambda,\zeta,\beta) = \left((m-\mu)^2 + A_\lambda^2(\zeta)\sigma^2\right)^{\frac{1}{2}\lambda-\frac{1}{4}} \exp^{\beta(m-\mu)} \mathcal{K}_{\lambda-\frac{1}{2}}\left(\zeta\sqrt{1+\left(\frac{m-\mu}{A_\lambda(\zeta)\sigma}\right)^2}\right)$$

where $\mathcal{K}_\lambda$ are modified Bessel functions of the second kind, and $A^2_\lambda(\zeta)$ is defined as

$$A^2_\lambda(\zeta) = \frac{\zeta\mathcal{K}(\zeta)}{\mathcal{K}_{\lambda+1}(\zeta)}$$

The function is a generalization of the CB function (Eq. (5.1)) for data sets where the mass resolution is not constant, but rather unknown and marginalized over. This describes the situation in this measurement, where the mass resolution differs with particle p_T and y_lab. The Hypatia function has more parameters and a more complicated form than the CB function, and the stability of the fits was negatively impacted. In order to improve the fitting, the parameter ζ was constrained to 0. Additionally, both tail parameters, n, are set equal to each other, $n_\mathrm{L} = n_\mathrm{H}$. The means of the Hypatia function and the Gaussian function used in the overall sum are also required to be equal, $\mu_\mathrm{Hyp} = \mu_\mathrm{Gaus}$. We find that including these constraints on the alternative signal function still allowed the fits to represent both the data and MC samples well.

The alternative background description was chosen to be a first order polynomial, since the background level in the J/ψ fits is low, and a straight line provides a decent description. Table 7.2 summarizes the settings used for the J/ψ fits.

	Nominal	**Alternative signal**	**Alternative background**
Signal	CB+CB	Hypatia + Gaussian	CB+CB
Background	Exponential function	Exponential function	First-order polynomial
Removed parameters	-	$\zeta = 0$,	-
Constrained parameters	$\mu_\mathrm{CB1} = \mu_\mathrm{CB2}$	$\mu_\mathrm{Hyp} = \mu_\mathrm{Gaus}$, $n_\mathrm{L} = n_\mathrm{H}$	$\mu_\mathrm{CB1} = \mu_\mathrm{CB2}$

Table 7.2: Overview of settings used for alternative fits to the J/ψ signal. The details are provided in the text.

Examples of toy fits are shown in Fig. 7.7. The bin on display is the $9 < p_\mathrm{T}(J/\psi) < 12\,\mathrm{GeV}$ bin, with y_CM and N_tracks integrated. Two toy fits out of 100 are shown. The gray line is the nominal fit to real data from which the black pseudodata are generated. It is the same in both panels. Blue, red and green are the fits with nominal, alternative signal,

and alternative background, respectively. In the case of J/ψ, the peaks are well defined, therefore the variation in yields is small.

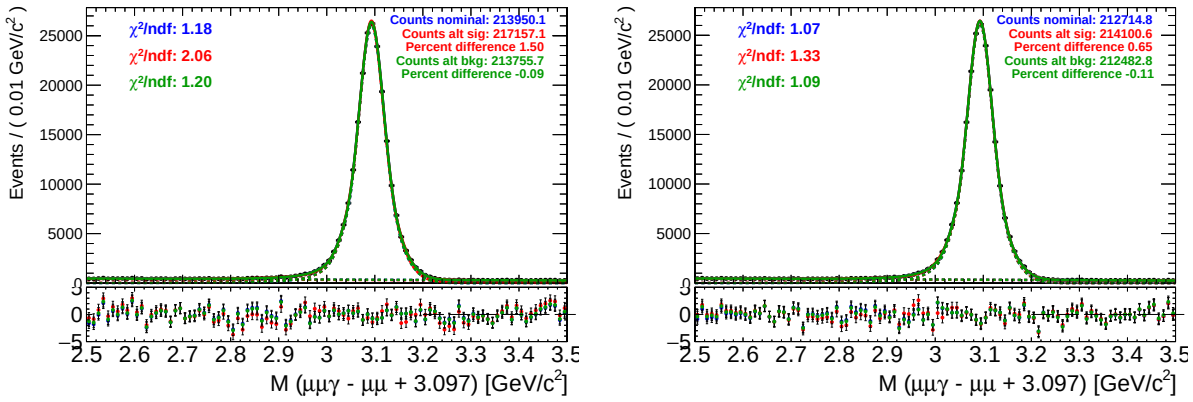

Figure 7.7: Two example toy fits for the $9 < p_{\mathrm{T}}(J/\psi) < 12\,\mathrm{GeV}$ bin (y_{CM} and N_{tracks} integrated) for the J/ψ systematic uncertainty. The gray line is the generating nominal fit from which the black pseudodata are obtained. The blue line is the fit to pseudodata with nominal settings, the red line is the fit with the alternative signal description, and the green line fit with the alternative background description. The lines largely overlap.

To obtain the final uncertainty for J/ψ fitting the remaining steps in the procedure are followed, as outlined in the beginning of this section. The results are plotted in the overall plots in Section 7.4, in Figs. 7.17, 7.18, and 7.19. The J/ψ fit uncertainty is relatively small, almost negligible.

7.2.2 Alternative signal and background for χ_c

The signal description is tested by changing the signal shape. Instead of a double-sided CB function, a Hypatia function (see Eq.(7.1)) is considered. The function has more parameters than the nominal signal shape. Therefore, the parameter ζ was removed by setting it to 0 after we checked that it does not compromise the quality of the fits. Additionally, the shape of the signal is constrained in the same manner as for the nominal fit: The Hypatia

function is first fitted to the MC and the shape parameters are fixed. Figure 7.8 shows the constrained fits, in the same bins as were used to show the nominal constraints (Fig. 5.5). Some of the parameters have a large uncertainty. This does not affect the results, as long as the shape is good, because the parameter uncertainties are not used. The background for the alternative signal toy fit is left unconstrained, which is the same setup as in the nominal case.

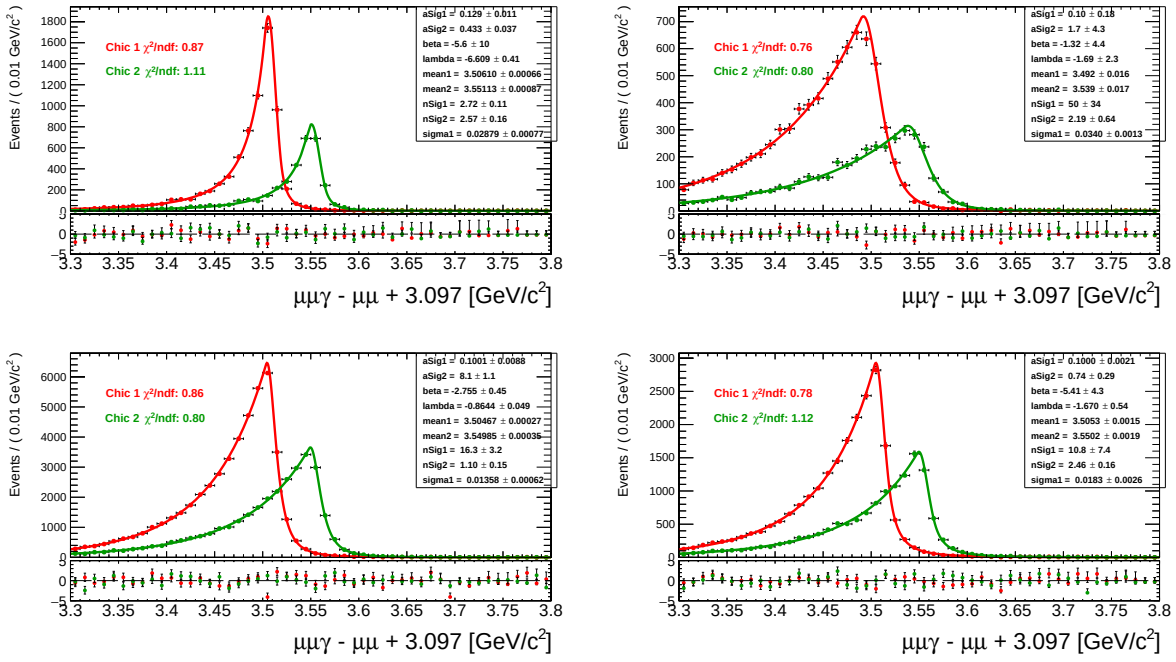

Figure 7.8: Examples of simultaneous fits to two χ_c peaks in the MC. Each peak is fitted with a Hypatia function. See the text for a detailed description of the fitting procedure. **Top row:** Comparison of resolution in different rapidity regions. Left: midrapidity ($|y_{\mathrm{CM}}| < 1.0$), third p_{T} bin ($12 < p_{\mathrm{T}} < 18\,\mathrm{GeV}$). Right: forward rapidity ($1.0 < |y_{\mathrm{CM}}| < 1.9$), third p_{T} bin ($12 < p_{\mathrm{T}} < 18\,\mathrm{GeV}$). **Bottom:** Examples of multiplicity bins. Left: $0 < N_{\mathrm{tracks}} < 50$. Right: $100 < N_{\mathrm{tracks}} < 150$.

For the background shape uncertainty, the RooDstD0BG function is used instead of the

threshold function (5.3):

$$\text{RooDSTD0}(m|m_0, A, B, C) = \left(1 - \exp\left(-\frac{m - m_0}{C}\right)\right) \cdot \left(\frac{m}{m_0}\right)^A + B\left(\frac{m}{m_0} - 1\right), \quad (7.2)$$

however with parameter $B \equiv 0$ because it was found to be consistent with 0 in most of the fits, and removing the parameter improves the fit stability. The rest of the fit is kept the same as in the nominal case, using a constrained DCB for each signal peak.

	Nominal	**Alternative signal**	**Alt. background**
Signal	Double-sided Crystal Ball (DCB)	Hypatia	DCB
Background	Threshold function	Threshold function	RooDSTD0
Removed parameters	-	$\zeta = 0$	$B = 0$
Constrained parameters	DCB shape (MC Fit)	Hypatia shape (MC Fit)	DCB shape (MC Fit)

Table 7.3: Overview of settings used for alternative fits to the χ_c signal. The details are provided in the text.

Table 7.3 summarizes the settings for the χ_c toy fits. Examples of toy distributions are shown in Fig. 7.9. Each row corresponds to a different bin. The bins are the same ones as those for which the constraints were shown in Fig. 5.5 for the nominal signal shape, and in Fig. 7.8 for the alternative signal shape. Two toy fits are always shown for each bin, out of a total of 100 toy fits performed. The gray line is the nominal fit to real data from which the black pseudodata are generated and is always the same for the two toy fits on the same row. Blue, red and green lines are the fits with nominal, alternative signal, and alternative background, respectively. The peaks are much less well defined for χ_c than was the case for J/ψ, and the variations are clearly visible. The remaining steps in the procedure outlined at the beginning of this section are followed in order to obtain the percent-difference distributions and then the fitting systematic uncertainty. The uncertainties are plotted in the overall plots in Section 7.4, in Figs. 7.17, 7.18, and 7.19. The systematic uncertainty due to χ_c fits is one of the dominant uncertainties, which is expected, considering the difficulty of fitting the peaks.

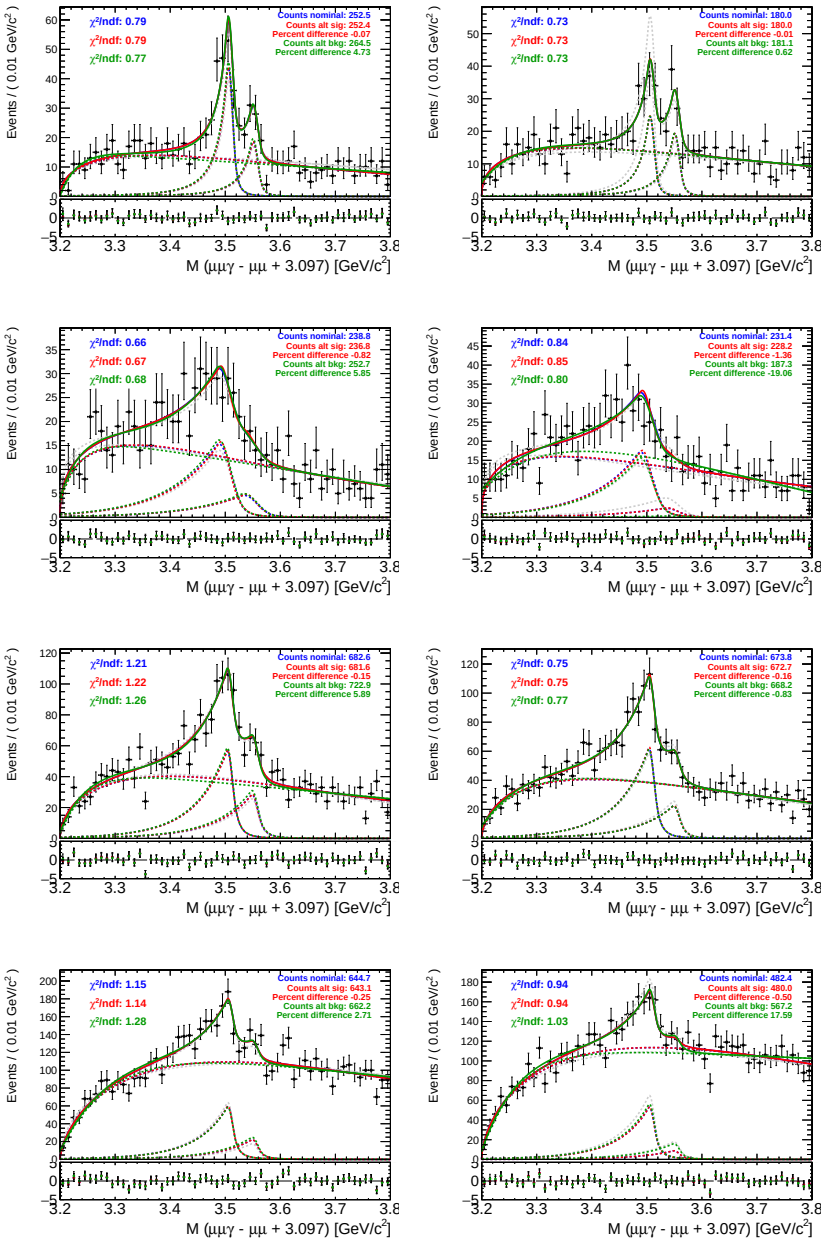

Figure 7.9: **Each row:** Two example χ_c toy fits for the four bins for which fit constraints were shown in previous figures. Details are given in the text. From top to bottom:
(1) midrapidity ($-1.0 < y_{\mathrm{CM}}(J/\psi) < 1.0$), third p_{T} bin ($12 < p_{\mathrm{T}}(J/\psi) < 18\,\mathrm{GeV}$)
(2) forward rapidity ($1.0 < |y_{\mathrm{CM}}(J/\psi)| < 1.9$), third p_{T} bin ($12 < p_{\mathrm{T}}(J/\psi) < 18\,\mathrm{GeV}$)
(3) low-multiplicity bin ($0 < N_{\mathrm{tracks}} < 50$)
(4) high-multiplicity bin ($100 < N_{\mathrm{tracks}} < 150$)

7.3 Acceptance related systematic uncertainties

The χ_c states are reconstructed only if the photon was emitted with rapidity $|y(\gamma)| < 2.4$ and $p_{\mathrm{T}}(\gamma) > 0.5\,\mathrm{GeV}/c$. We correct for the fraction of photons from the χ_c decays that lie outside of the acceptance window in order to present the results as the ratio of cross sections. This correction is determined from the Monte Carlo and depends on the underlying assumptions in the MC, namely on its χ_c kinematic distribution.

7.3.1 Pythia settings - effect of the χ_c kinematic distribution

The fraction of the photons from χ_c decays that is in the acceptance depends on the details of the settings used to generate the MC. Since the distribution is expected to be similar for χ_{c1} and χ_{c2}, the kinematic distribution plays a role mostly for the χ_c to J/ψ ratio. This effect is evaluated by changing the underlying parameters of the MC Pythia generator. This affects the χ_c kinematic distributions and changes the portion of photons that are in the acceptance: the dominant cut is $p_{\mathrm{T}}(\gamma) > 0.5$ GeV, the rapidity requirement $|y(\gamma)| < 2.4$ is secondary, since we always require $|y(J/\psi)| < 2.4$. Additionally, the photon $p_{\mathrm{T}}(\gamma)$ distribution is also changed, even when in the acceptance. The difference in overall results is then taken as the systematic uncertainty.

Table 7.4 lists the variations of the settings that were considered. The parameter *pTHat-Min* is the minimum invariant p_{T} used for generating the parton interaction. It has a direct effect on how hard or soft the resulting $p_{\mathrm{T}}(\chi_c)$ spectrum is. We vary the parameter from the nominal value of 4.5 GeV down to 3 GeV.0 and up to 6.0 GeV. The *c-mass* is the mass of the c-quark used in the generator and is varied in another step from the nominal value of 1.5 GeV to 1.43 GeV[3]. The last variation changes both the renormalization, *renormScale*,

[3] 1.43 GeV was a value used in a similar study by the advisor of this dissertation, and thus tested as a reasonable alternative.

and factorization, *factorScale*, scales. The default setting in Pythia8 is 2 (arbitrary code number), which denotes using the geometric mean of the squared transverse masses of the two outgoing particles, i.e. $mT_3 * mT_4 = \sqrt{((pT^2 + m_3^2) * (pT^2 + m_4^2))}$ for the Q^2 renormalization scale (where indices 3 and 4 denote outgoing particles, which in this case are the χ_c and gluon/quark), and the geometric mean of squared transverse masses of the two outgoing particles for the Q^2 factorization scale. This has been changed to code 3, which changes both means from geometric to arithmetic, i.e. $(mT_3^2 + mT_4^2)/2 = pT^2 + 0.5 * (m_3^2 + m_4^2)$ for renormalization. This was the setting that was used in Pythia6 and is thus a reasonable alternative. Moreover, the renormalization and factorization scales were multiplied by a factor of 2 (*renormMultFac = 2, factorMultFac = 2*) in order to amplify the effect of the scale on our measurement. For details, see Pythia8 [104] and its documentation.

	Nominal	**Alternative 1** pThat3	**Alt. 2** pThat6	**Alt. 3** *c*-mass	**Alt. 4** reNorm
pTHatMin [GeV]	4.5	3.0	6.0		
c-quark mass [GeV]	1.5 (def.)			1.43	
renormScale	2 (default)				3
factorScale	2 (default)				3
renormMultFac	1 (default)				2
factorMultFac	1 (default)				2

Table 7.4: The nominal settings for the MC (official production) and settings used for the four alternative settings used in estimating the systematic uncertainties. Blank spots for the alternatives denote using the nominal values.

We generated four alternative MC sets with the settings outlined in Table 7.4 and explained in the text. However, the χ_c efficiency is very low, and a very large sample would be needed to obtain decent statistics. This was done for the official MC, but is not practical for the systematic study. Therefore, relatively small samples were used (41k - 190k post-filter generated χ_c, compared to 31M in the official sample). The size of the samples is large enough to work with generated variables, but not reconstructed variables. It was decided to

use gen-variables to compare the p_{T} distributions of photons, derive the weight that modifies the official MC to match the alternative MC, and then use this reweighted MC to obtain the change in the overall result. The reason for this procedure is discussed in the note at the end of this section. The detailed description of the procedure follows:

p_{T} weighting: In the first step, each generated alternative MC is weighted to match data, in a similar procedure to the one done for p_{T} for the official sample (see Section 4.3). The changes to the MC settings modify the χ_c p_{T} distributions. Without correcting for this, a large portion of the difference in the overall results between the MCs would come from the alternative MCs not having realistic p_{T} distributions, and would not describe realistically possible variations. Therefore, each sample is weighted to match the χ_c data $p_{\mathrm{T}}(J/\psi)$ distribution[4]. This is done in four $p_{\mathrm{T}}(J/\psi)$ bins, as shown in Fig. 7.10. The figure shows the integrated $p_{\mathrm{T}}(J/\psi)$ distributions for χ_c passing all the acceptance and selection cuts (i.e. the raw yield of the data). The overall normalization is arbitrary, and in the figure it is set to match the value in the second bin to provide a visual cue to the hardness of the spectrum. Bin-by-bin weighting was considered good enough, especially considering the statistics we have available. Each alternative MC is then individually weighted to match the distribution of the data. The $p_{\mathrm{T}}(\gamma)$ distribution of γ from χ_c decays is shown in Fig. 7.11. The top panel shows the arbitrarily normalized distributions for various MC sets. The bottom panel shows the ratio of the alternative distributions to the nominal MC distribution. The left plot shows the spectrum that was not weighted by $p_{\mathrm{T}}(J/\psi)$ (not used anywhere, shown only in order to illustrate the effects of p_{T} reweighting). The right plot shows the results for the properly weighted MC. The most noticeable difference is in the *ptHat6* and *reNorm* variations.

[4]As discussed in Section 5.2.1.1, variables of the J/ψ daughter are used for χ_c.

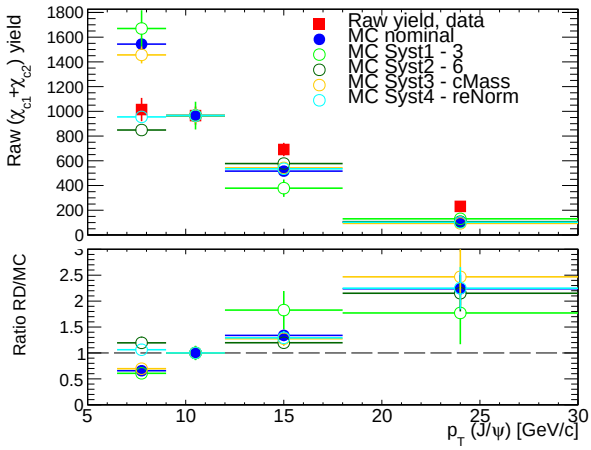

Figure 7.10: $p_{\mathrm{T}}(J/\psi)$ distributions of χ_c passing all cuts in data and MC, integrated in rapidity. Normalization is arbitrary. Bottom plot is the ratio of each MC to data, which is then used to reweight the MC to match data.

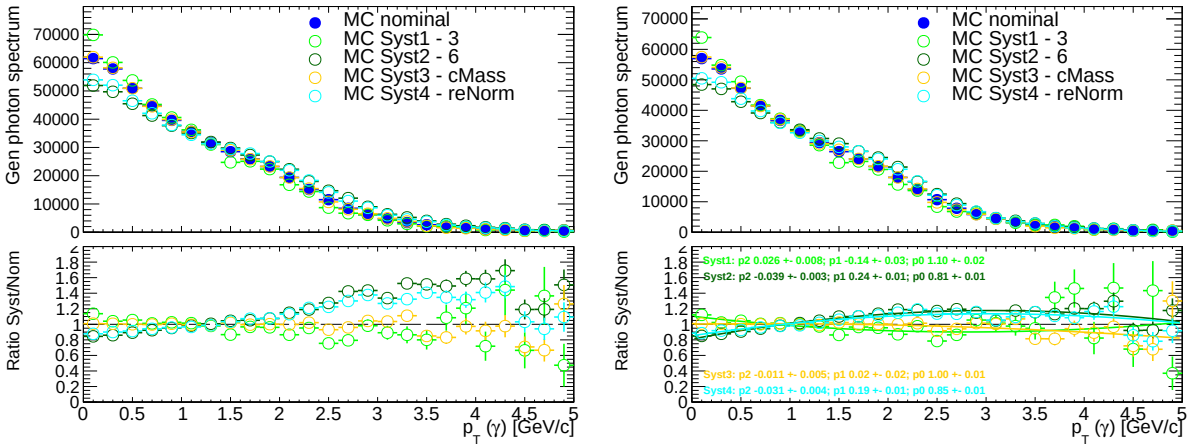

Figure 7.11: $p_{\mathrm{T}}(\gamma)$ distributions of photons from χ_c decay that are in the acceptance, plotted for nominal and alternative settings. Bottom panel shows the ratio of alternative distributions to nominal MC. Left plot shows the distributions when MC is not $p_{\mathrm{T}}(J/\psi)$-reweighted and serves only as a crosscheck. Right plot is with χ_c $p_{\mathrm{T}}(J/\psi)$ weighting and shows a plausible variation of the γ spectrum.

Variation weight: The differences in the photon $p_{\mathrm{T}}(\gamma)$ spectrum in the right plot of Fig. 7.11 are due to the details of the MC settings. In order to eliminate the statistical

fluctuations, each ratio of alternative/nominal spectrum is then fitted with a second order polynomial in the region 0-5 GeV to describe the weighting. The weights are:

- **pThat3:** $0.026 * p_{\mathrm{T}}^2 - 0.14 * p_{\mathrm{T}} + 1.10$
- **pThat6:** $-0.039 * p_{\mathrm{T}}^2 + 0.24 * p_{\mathrm{T}} + 0.81$
- **c-mass:** $-0.011 * p_{\mathrm{T}}^2 + 0.02 * p_{\mathrm{T}} + 1.00$
- **reNorm:** $-0.031 * p_{\mathrm{T}}^2 - 0.19 * p_{\mathrm{T}} + 0.85$

p_{T} denotes $p_{\mathrm{T}}(\gamma)$ of the photon from the χ_c decay (i.e. conversion in the reco). There are only few γ above 5 GeV, both in the MC and the data. For simplicity, the weights were always set to 1 for those photons.

Variations in different kinematic regions: The weights for the MC variations were determined from the integrated bin. As a cross-check, we considered the possibility that the variation is more pronounced in a specific kinematic region, in which case our procedure would underestimate the uncertainty for such a region. The weights were rederived for χ_c in the forward rapidity/midrapidity, and for low/high-p_{T}. Figure 7.12 shows the result of the crosscheck. The top row compares weights from midrapidity (left panel) and forward rapidity (right panel). The bottom row shows low-p_{T} ($6.5 < p_{\mathrm{T}}(J/\psi) < 12\,\mathrm{GeV}$) and high-$p_{\mathrm{T}}$ ($12 < p_{\mathrm{T}}(J/\psi) < 30\,\mathrm{GeV}$). We can compare the rederived weights with the weights from the integrated bin (see the right panel of Fig. 7.11) and see that the rapidity does not play a significant role. We observe that binning in $p_{\mathrm{T}}(J/\psi)$ has some effect, however it is not important: in the high-$p_{\mathrm{T}}(J/\psi)$ region the variations are smaller than in the integrated bin, and the uncertainty is thus covered. It may appear that we would underestimate the uncertainty in the low-$p_{\mathrm{T}}(J/\psi)$ region, however the difference between the weights obtained from the integrated and low-p_{T} bins is in the region of $p_{\mathrm{T}}(\gamma) > 3\,\mathrm{GeV}$, where there are almost

no photon statistics. The weights for low-p_{T} (γ), where the data lie, are similar. Thus, the integrated weights can be used everywhere.

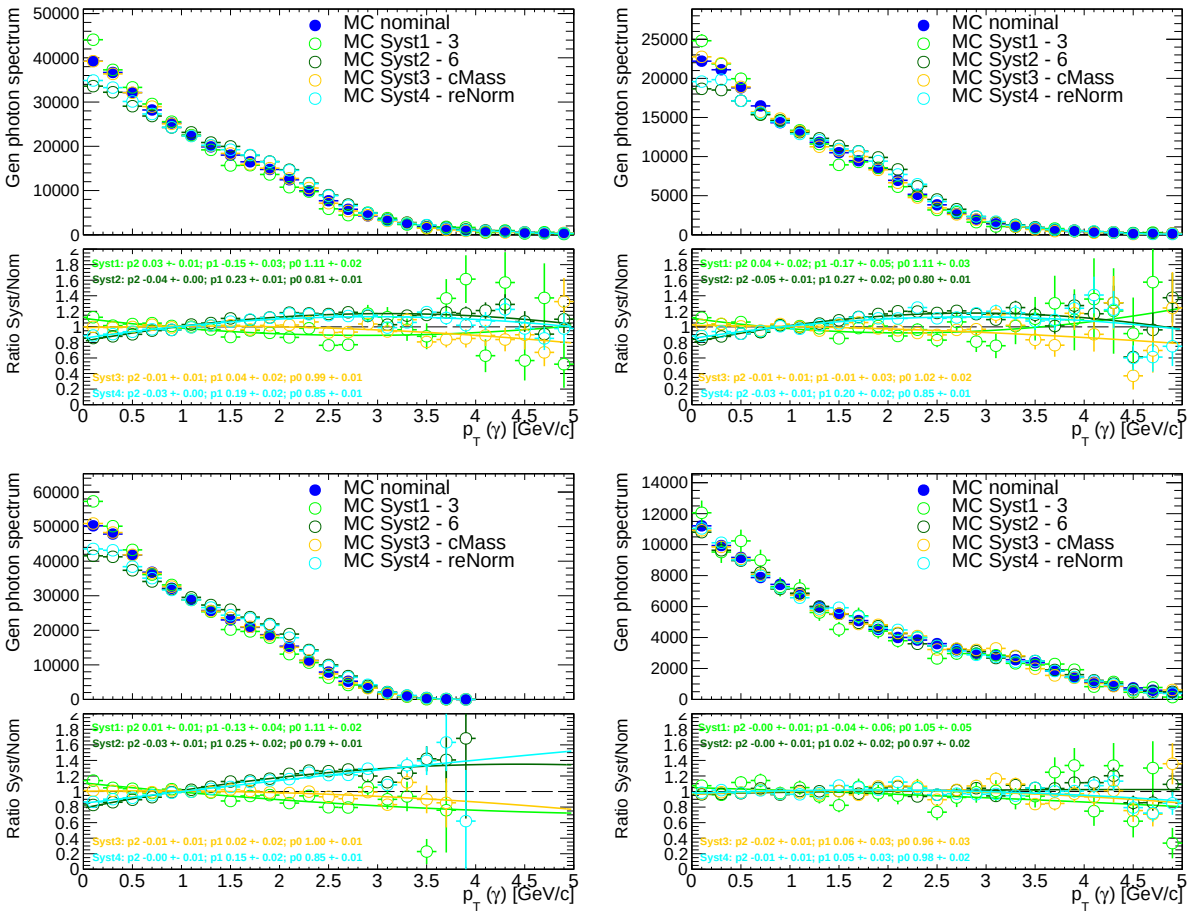

Figure 7.12: A crosscheck where the weights are rederived in various kinematic subregions of χ_c, in order to check that the overall weights are applicable. **Top row** Rapidity - left is midrapidity ($|y_{\mathrm{lab}}(J/\psi)| < 1.6$), right forward ($1.6 < |y_{\mathrm{lab}}(J/\psi)| < 2.4$) **Bottom row:** $p_{\mathrm{T}}(J/\psi)$- left is low-p_{T}: ($6.5 < p_{\mathrm{T}}(J/\psi) < 12\,\mathrm{GeV}$), right high-$p_{\mathrm{T}}$: ($12 < p_{\mathrm{T}}(J/\psi) < 30\,\mathrm{GeV}$)

Systematic differences for the χ_c to J/ψ ratio: The weights that were obtained for the MC alternatives, as described in the previous paragraph, are used to weight the official MC. The physics results are then, in principle recalculated using the newly weighted MC to

obtain the systematic variations. In practice, however, the yields from fits to data are not affected by the variation, and thus only the efficiency is recalculated. The variation of the efficiency directly matches the variation in the final results.

Figure 7.13 shows the results of varying the MC settings for the y-integrated p_{T} dependence in the left panel, and as a function of rapidity in the right panel. We see that the greatest up/down variation comes from $pThat3$ and $pThat6$, which is expected from the right panel of Fig. 7.11. Moreover, the lower-p_{T} χ_c are more affected, which originates from the decay kinematics (lower-$p_{\mathrm{T}}(J/\psi)$ χ_c have a larger probability to have a decay photon around the $p_{\mathrm{T}}(\gamma) = 0.5\,\mathrm{GeV}$ cut-off).

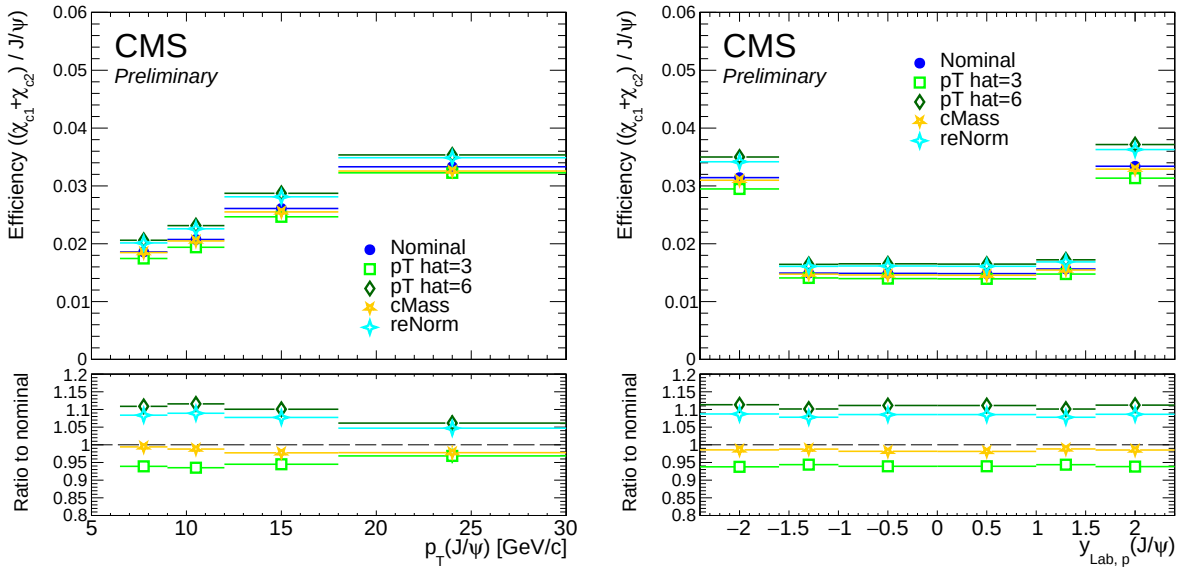

Figure 7.13: Overall variation due to changes in the MC settings, for the various changes described in the text. **Left:** As a function of p_{T}. **Right:** As a function of rapidity.

Figure 7.14 shows the variations as a function of N_{tracks}. As expected, the MC-setting variations do not depend on multiplicity, as they should be the same irrespective of the activity of the underlying event. Figure 7.15 displays the variations as a function of p_{T} for the three rapidity subranges (backward, midrapidity, and forward, in the center-of-mass

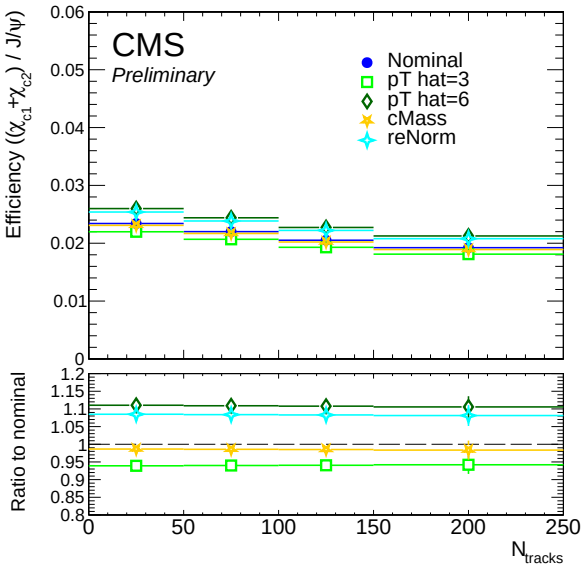

Figure 7.14: Variation due to the MC settings as a function of number of tracks.

frame). There are no significant differences from the overall, integrated p_{T} dependence. Because the systematic uncertainty due to the MC settings shows mild, but relevant, p_{T}

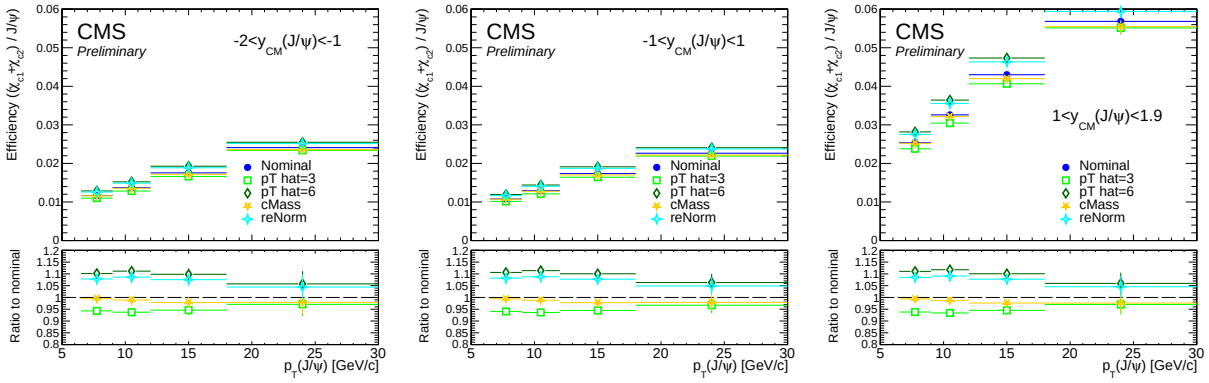

Figure 7.15: Variation due to the MC settings as a function of p_{T} in specific rapidity ranges, expressed in the center-of-mass frame. The ranges are backward rapidity (Pb-going direction, $-2 < y_{\mathrm{CM}} < -1$), midrapidity ($-1 < y_{\mathrm{CM}} < 1$), and forward rapidity (proton-going direction, $1 < y_{\mathrm{CM}} < 1.9$) for the left, middle and right panel, respectively.

dependence, it was decided to report the uncertainty bin by bin for each kinematic set,

using the largest deviation shown in Figs. 7.13, 7.14, and 7.15. The largest value is obtained independently in each bin (usually $pThat6$), and applied as both up and down systematics. This procedure symmetrizes the uncertainty. The variations that we consider are arbitrary to start with, and any observed asymmetry in the values is not significant.

Note on the methodology We decided to use the official MC that was reweighted to match differences in each alternative MC distribution, instead of using the alternative MC samples directly. The use of the official MC increases statistics to the point where we can use reconstructed variables. However, the statistics in the alternative MC is sufficient for generated variables, and for the acceptance part of the correction, that is all that is needed. We could check from the generated variables what portion of the γ fall in the acceptance (p_{T} $(\gamma) > 0.5\,\mathrm{GeV}$, $|y_{lab}(\gamma)| < 2.4$), and use the variation of that as the systematic. However, this encompasses only about half of the overall variation. The efficiency of the photon reconstruction is heavily dependent on $p_{\mathrm{T}}(\gamma)$. We see in Fig. 6.5 that the efficiency changes by almost an order of magnitude in the $p_{\mathrm{T}}(\gamma)$ range that we consider. Therefore, changes to the p_{T} spectrum of photons will change the overall efficiency of the χ_c reconstruction, even when considering only photons already in the acceptance. Figure 7.16 illustrates this effect. The left panel shows the contribution from the acceptance effects (the p_{T} $(\gamma) > 0.5\,\mathrm{GeV}$ cut), while the right plot shows the overall effect (acceptance and the change of the conversion efficiency with $p_{\mathrm{T}}(\gamma)$). The right plot is the correct variation for the overall systematic uncertainty, as it includes both effects, however in order to obtain it, the reconstructed information is needed; hence the use of the official MC.

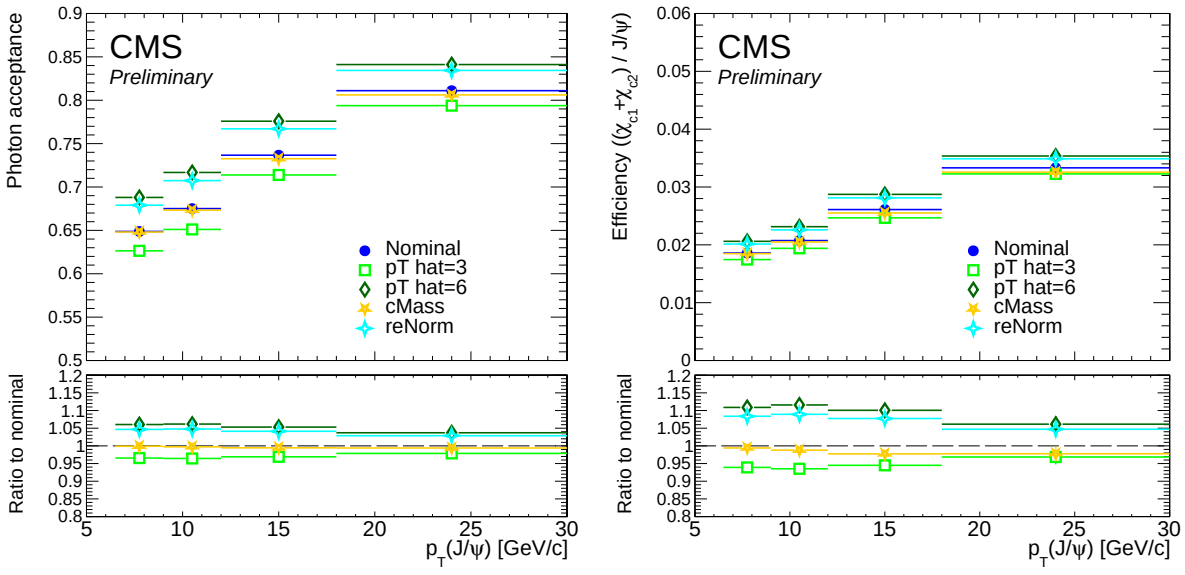

Figure 7.16: Systematic variation due to different settings for the MC generation. **Left:** Variation considering only acceptance. **Right:** Variation considering acceptance as well as efficiency.

7.3.2 Polarization

The polarization of the χ_{c1} and χ_{c2} is unknown from the data. It is assumed to be 0 (non-polarized) in the MC. The polarization affects the decay kinematics, and different polarization scenarios would modify the overall χ_c to J/ψ result. The modification would not be a systematic uncertainty as such, but rather an adjustment to the results based on the selected polarization scenario. However, the full study was deemed to be beyond the scope of the analysis, and it was not performed. The current experimental results for J/ψ are consistent with no polarization [118, 119] indicating that the zero-polarization assumption is not unrealistic. Nonetheless, there is an evidence for non-zero χ_c polarization in $p+p$ collisions [120]. Therefore, exploring the different polarization schemes would be a reasonable extension of this work.

7.4 Overall systematic uncertainty

Individual systematic uncertainties are added together in quadrature, under the assumption that they are uncorrelated. Figure 7.17 shows the overall uncertainty for the χ_c-to-J/ψ ratio as a function of $y_{\mathrm{lab},p}(J/\psi)$ and $p_{\mathrm{T}}(J/\psi)$ for the integrated bin, while Fig. 7.18 shows the uncertainty as a function of the number of tracks. We can see that the dominant uncertainties are the conversion selection, the Pythia settings, and the χ_c fits, which are all on roughly same level of 10 %. The systematic uncertainty from the J/ψ fits is predictably much smaller, because the J/ψ peak is very well defined with only a small background.

Figure 7.19 displays various components of the systematic uncertainty as a function of $p_{\mathrm{T}}(J/\psi)$ for the three rapidity bins that we use in this analysis. The uncertainties are comparable to the integrated bin. The only significant difference between the rapidity bins comes from the χ_c fits. The uncertainty for midrapidity is smaller than for forward and backward

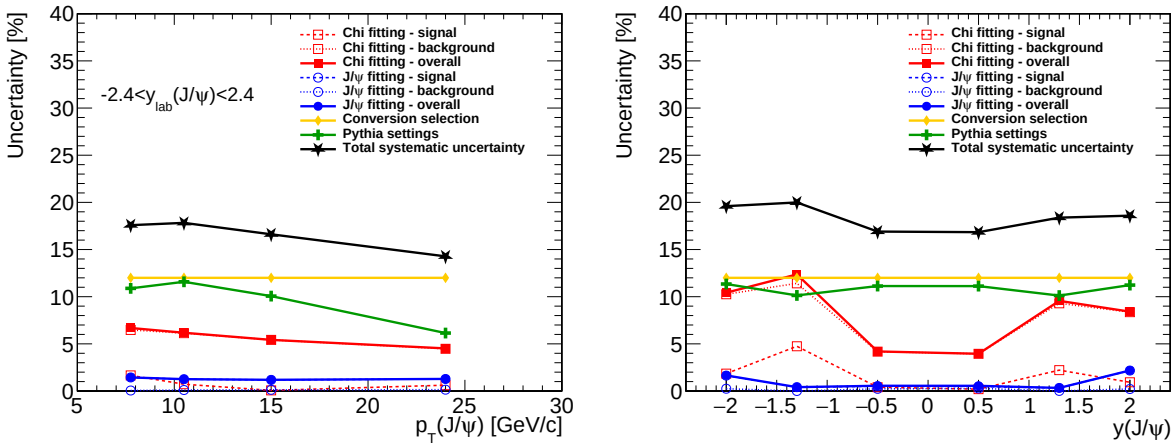

Figure 7.17: All systematic uncertainties plotted as a function of $p_{\mathrm{T}}(J/\psi)$ (left) and rapidity, $y_{\mathrm{lab},p}(J/\psi)$, (right).

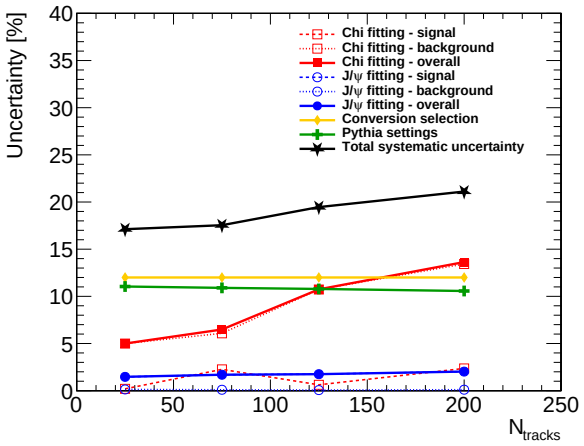

Figure 7.18: All systematic uncertainties as a function of number of tracks.

rapidities. This is predictable, because center-of-mass midrapidity mostly corresponds to the barrel region of the detector, where the resolution for χ_c peaks is much better. This, in turn, lowers the fit uncertainties.

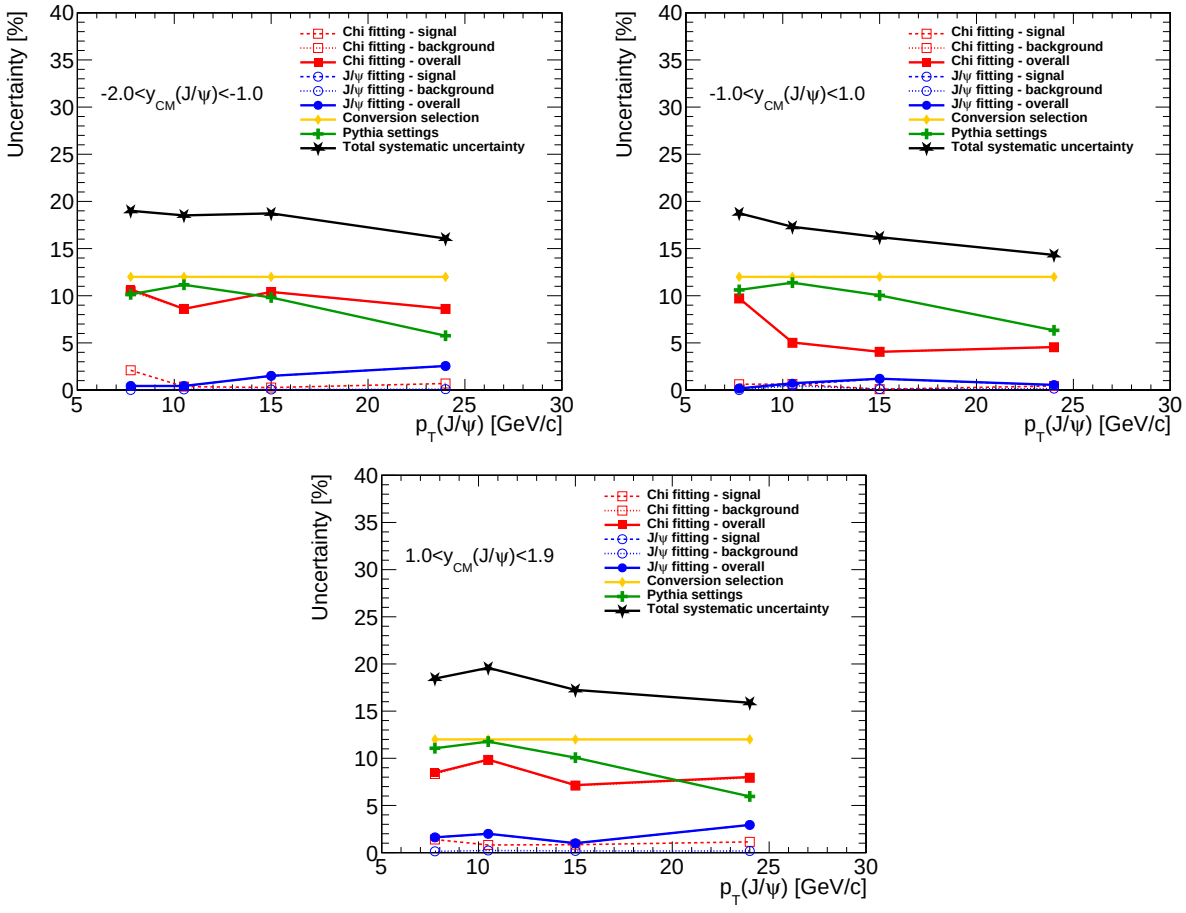

Figure 7.19: All systematic uncertainties for backward rapidity (Pb-going direction, $-2 < y_{\mathrm{CM}}(J/\psi) < -1$), midrapidity ($-1 < y_{\mathrm{CM}}(J/\psi) < 1$), and forward rapidity (p-going direction, $1 < y_{\mathrm{CM}}(J/\psi) < 1.9$).

Chapter 8

Results and discussion

In order to calculate the χ_c-to-J/ψ ratio, we start with the raw χ_c and J/ψ yields from the fits described in Section 5. The χ_c and J/ψ yields are divided and then corrected, with the correction derived in Section 6, to obtain the final χ_c-to-J/ψ ratio. To carry out this division, yields are treated as independent, and their statistical uncertainties are added in quadrature. The χ_c yields have much larger statistical uncertainties, which dominate the overall uncertainty of the ratio. The statistical uncertainties are shown in the succeeding figures as the vertical error bars. The systematic uncertainties were derived in Section 7 directly for the ratio, and are added to the overall results. They are plotted as the shaded boxes. We report the results in the variables and binning divisions discussed in Section 5.2.1. The overview of all presented results is presented at the end of this chapter in Tab. 8.1.

8.1 N_{tracks} dependence

Figure 8.1 displays the χ_c-to-J/ψ ratio as a function of N_{tracks}. The results are effectively flat across the full reach of multiplicities available in the $p+\text{Pb}$ collisions at $\sqrt{s_{_{NN}}} = 8.16\,\text{TeV}$, showing no strong multiplicity-related effects. This suggests that the event activity and the

related final-state effects do not dramatically change the ratio.

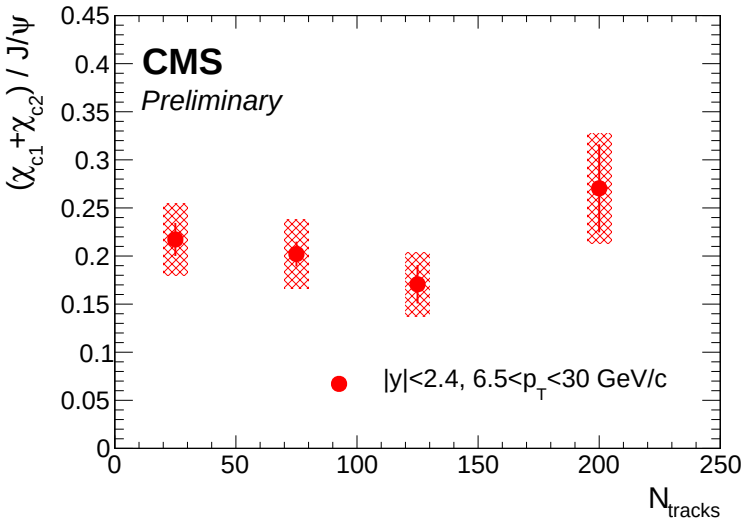

Figure 8.1: χ_c-to-J/ψ ratio plotted as a function of N_{tracks}

8.2 Rapidity dependence

Results as a function of rapidity for the full range of the analysis are presented in Fig. 8.2. The rapidity is defined in the lab frame, but with the proton beam momentum always oriented in the positive rapidity direction, as discussed in Section 5.2.1.3. The center of mass is also plotted as a brown dashed line. In this frame, it is offset by 0.465 units of rapidity.

A notable feature of the rapidity plot is that the ratio is somewhat higher at midrapidity (two central points). The first suggestion is that this is a detector artifact. We know that the overall reconstruction efficiency for χ_c varies a lot between midrapidity and forward rapidity. This variation is caused by the photon the conversion efficiency, while the J/ψ reconstruction efficiency is fairly flat. If the efficiency estimate did not capture the rapidity-dependent trend well, it would cause points to be misplaced from their real values. This would be expected to be symmetric in rapidity. However, closer inspection does not support

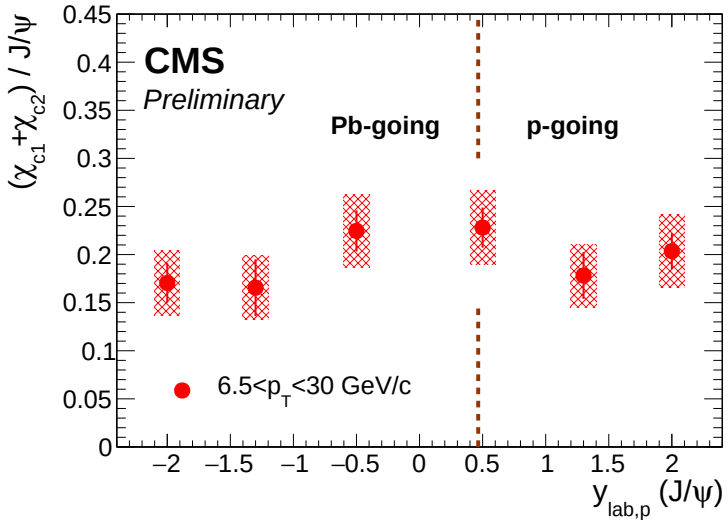

Figure 8.2: χ_c-to-J/ψ ratio plotted as a function of rapidity $y_{\mathrm{lab},p}$. The rapidity is defined in the lab frame, with the p-going direction always being positive. The center of mass of the interacting system is shown by the brown dashed line.

the artifact hypothesis. The efficiency changes rapidly around $|y_{\mathrm{lab}}| \approx 1.6$ (see Figs. 6.7 and 6.5), that is, for the two outermost points. Meanwhile, the result varies in a different region, around $|y_{\mathrm{lab}}| \approx 1.0$, for the four outermost points. In order to bring the innermost points to the same line, the photon conversion efficiency would have to be higher in the midrapidity region than it is currently (i.e. high in the forward region, low in the overlap, somewhat high again in midrapidity), for which we have no indication based on the analysis. A constant fit to the data, considering only statistical uncertainties, yields $\chi^2/\mathrm{ndf} = 8.0/5$, with a p-value of 0.20. We see no reason to exclude the hypothesis that the ratio is flat and the pattern is just a fluctuation.

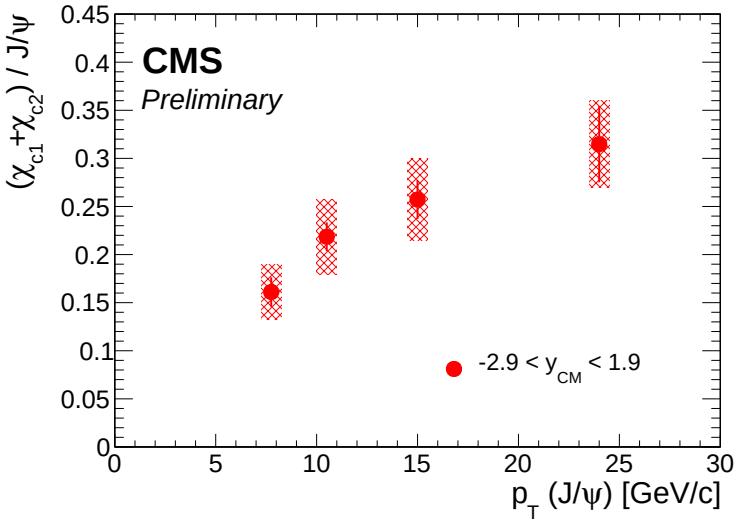

Figure 8.3: χ_c-to-J/ψ ratio plotted as a function of $p_{\mathrm{T}}(J/\psi)$, shown in red points. The results are integrated over all the detector acceptance $|y_{\mathrm{lab}}| < 2.4$, corresponding to $-2.9 < y_{\mathrm{CM}} < 1.9$.

8.3 Integrated p_{T} dependence

Figure 8.3 displays the $p_{\mathrm{T}}(J/\psi)$ dependence of the ratio, integrated over the full rapidity acceptance $|y_{\mathrm{lab}}(J/\psi)| < 2.4$. The ratio increases with increasing p_{T}, ranging from 0.16 at $p_{\mathrm{T}}(J/\psi)$ of 6.5–9 GeV, all the way to 0.31 for $18 < p_{\mathrm{T}}(J/\psi) < 30$ GeV.

8.4 Rapidity divided p_{T} dependence

We have divided our data sample into three sub-ranges in the center-of-mass frame. The resulting p_{T} dependence for each subrange is displayed in Fig. 8.4. The left panel illustrates the rapidity ranges into which we divided our data. The right plot shows the actual p_{T}-dependent results, with the colors corresponding to the shaded boxes in the left plot. The results are consistent with each other within the uncertainties and follow the same general trend as the integrated p_{T} dependence. There is no significant rapidity-dependent trend.

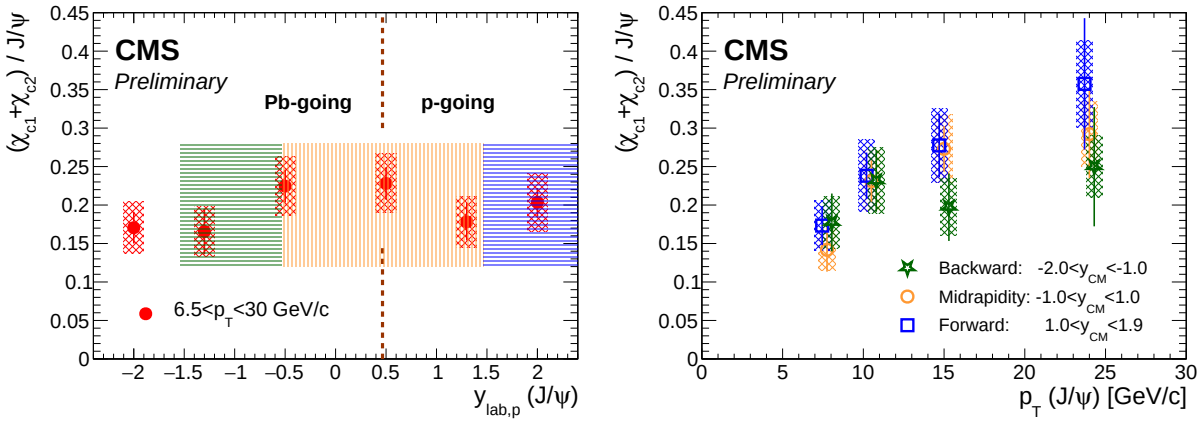

Figure 8.4: **Left:** χ_c-to-J/ψ ratio plotted as a function of rapidity $y_{\mathrm{lab},p}$ (same data points as in Fig. 8.2). The shaded boxes show the rapidity ranges corresponding to those shown in the plot on the right, with the matching colors. **Right:** χ_c-to-J/ψ ratio plotted as a function of p_{T} for three rapidity ranges defined in the center-of-mass frame: **green:** backward rapidity, Pb-going direction ($-2 < y_{\mathrm{CM}}(J/\psi) < -1$), **orange:** midrapidity ($-1 < y_{\mathrm{CM}}(J/\psi) < 1$), **blue:** forward rapidity, p-going direction ($1 < y_{\mathrm{CM}}(J/\psi) < 1.9$).

8.5 Comparison with other measurements and models

As mentioned in Section 2.5, there are limited measurements from the other experiments to which we could compare our data. Two $p+p$ measurements that were performed at a similar kinematic range and collision energy are from LHCb [74] and ATLAS [79]. Figure 8.5 shows the comparison. Our results are the same as presented earlier in this section, and in the same color scheme. The left plot compares the χ_c-to-J/ψ ratio, plotted as a function of p_{T} for our midrapidity data set, with the ATLAS measurement from $|y| < 0.75$ shown in black points. The right panel compares our rapidity integrated set with the LHCb result from forward rapidity, $2.0 < |y| < 4.5$. In both instances, the $p+p$ measurements are from $\sqrt{s} = 7\,\mathrm{TeV}$ collisions.

We observe that the χ_c-to-J/ψ ratios are similar, and the $p+\mathrm{Pb}$ results do not deviate significantly from the $p+p$ measurements. There are a few important points to consider while

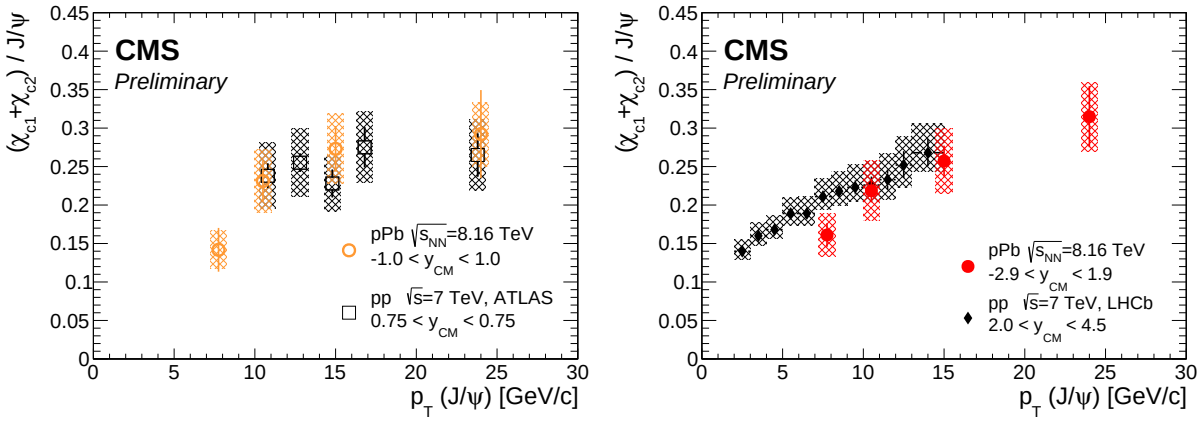

Figure 8.5: Comparison of our result with previous results from $p+p$ collisions. **Left:** Comparison of midrapidity p_{T} measurement (orange) with the ATLAS results from $p+p$ collisions at $\sqrt{s} = 7\,\mathrm{TeV}$ at $|y| < 0.75$ [79]. **Right:** Comparison of rapidity integrated p_{T} measurement (red) with the LHCb results from $p+p$ collisions at $\sqrt{s} = 7\,\mathrm{TeV}$ at forward rapidity of $2.0 < |y| < 4.5$ [74] (black).

making the comparison. The $p+p$ results differ by energy ($\sqrt{s} = 7\,\mathrm{TeV}$ vs $\sqrt{s_{NN}} = 8.16\,\mathrm{TeV}$) and, especially for the LHCb, rapidity ($2.0 < y_{\mathrm{CM}} < 4.5$ vs $-2.9 < y_{\mathrm{CM}} < 1.9$). Nonetheless, it is not naively expected that these differences should affect the χ_c-to-J/ψ ratio much:

- **Energy:** The increase in the collision energy ($\sqrt{s_{NN}} = 8.16\,\mathrm{TeV}$ vs $\sqrt{s} = 7\,\mathrm{TeV}$) should not have a large impact on the results. The increase in the production cross section is modest, and, more importantly, similar between χ_c and J/ψ. The expected effect on the χ_c-to-J/ψ ratio is small.

- **Rapidity:** The ATLAS measurement is close in rapidity to our data ($|y_{\mathrm{CM}}(J/\psi) < 0.75|$ vs. $|y_{\mathrm{CM}}(J/\psi) < 1|$) and the ratios should be directly comparable.

  There is not any overlap in rapidity between the LHCb and our results, and the ratio of χ_c to J/ψ could be different in different rapidity regions. However, our rapidities are connected (i.e. ours stops almost at $y_{\mathrm{CM}} = 2.0$, which is where the LHCb measurement starts), and there is not any evidence of a strong rapidity dependence in our measure-

ment (Fig. 8.2). Moreover, the $p+p$ results from midrapidity and forward rapidity are consistent with each other (see Fig. 2.11). Therefore, the effect from the rapidity difference between our and LHCb results should be limited.

Because the measured ratio in $p+\mathrm{Pb}$ is almost same as in the $p+p$, our results are consistent with no modification of the χ_c states in $p+\mathrm{Pb}$ collision beyond modifications that are present in J/ψ.

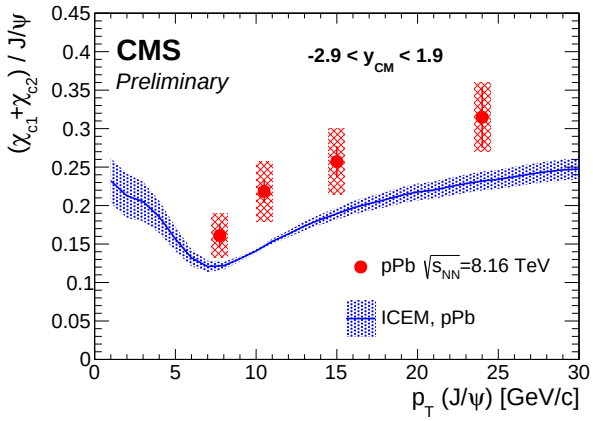

Figure 8.6: Comparison of the rapidity-integrated result (red points) to the calculation from the improved color evaporation model (blue line and band) in the same rapidity range [121].

Figure 8.6 shows the $p+\mathrm{Pb}$ calculation from the improved color evaporation model (ICEM) [121], compared to the results at the same rapidity range, $-2.9 < y_{\mathrm{CM}} < 1.9$. The model includes modifications to the nPDF using EPS09 [122]. The model captures the general increase of the ratio with the $p_{\mathrm{T}}(J/\psi)$ well, but underpredicts the values of χ_c-to-J/ψ ratio across the reported p_{T} range.

8.5.1 Comparison to ψ(2S)

In Section 2.5.3 we discussed that the existing measurements of the excited S-state, ψ(2S), favor additional suppression of the state in p + Pb compared to the ground state J/ψ. Specifically, this additional suppression is quantified by the double ratio DR defined in Eq. (2.4). The DR shows a strong $N_{\rm coll}$ trend (Fig. 2.14), and the state shows significant suppression across a range of rapidities (Fig. 2.15). We can obtain the double ratio also by dividing the χ_c-to-J/ψ ratio in p + Pb to the χ_c-to-J/ψ ratio in $p + p$, i.e. by dividing our results with the $p + p$ measurements. The DR thus obtained has only an approximate character, because the $p+p$ measurements are at a different experiment, energy and rapidity. However, as discussed in previous paragraph, these differences should not alter the results much, and the DR should be a reasonable estimate. We observe a DR consistent with 1 across the full $p_{\rm T}$ range, with a hint of lower DR only for the lowest-$p_{\rm T}$ bin. In the lowest-pt bin, the division of our results with the LHCb values, while neglecting the systematic uncertainties, leads to approximate DR value between 0.65–0.80. These values for the DR are higher than the similar values for the ψ(2S) state [85, 88, 123, 124], suggesting that the χ_c states are less suppressed. This is perhaps not surprising if only the binding energy of the states is considered (approximated as the mass difference between the state and the $D\overline{D}$ threshold) as the χ_c binding energy is between the J/ψ and ψ(2S) binding energies (see Fig.2.3), but our result disfavors any strong dissociation effects from orbital angular momentum.

Dependence		**Bin** [units]		χ_c**-to-**J/ψ **ratio** $\pm$(stat) $\pm$ (syst)
N_{tracks}		0 – 50		$0.217 \pm 0.017 \pm 0.037$
		50 – 100		$0.202 \pm 0.013 \pm 0.035$
		100 – 150		$0.171 \pm 0.020 \pm 0.033$
		150 – 250		$0.270 \pm 0.046 \pm 0.057$
$y_{\text{lab},p}(J/\psi)$		-2.4 – -1.6		$0.171 \pm 0.020 \pm 0.033$
		-1.6 – -1.0		$0.166 \pm 0.028 \pm 0.033$
		-1.0 – 0.0		$0.225 \pm 0.020 \pm 0.038$
		0.0 – 1.0		$0.228 \pm 0.020 \pm 0.038$
		1.6 – 2.4		$0.204 \pm 0.017 \pm 0.038$
$p_{\text{T}}(J/\psi)$	Integrated $-2.4 < y_{\text{lab},p}(J/\psi) < 2.4$	6.5 – 9	[GeV]	$0.161 \pm 0.015 \pm 0.028$
		9 – 12		$0.218 \pm 0.015 \pm 0.039$
		12 – 18		$0.257 \pm 0.020 \pm 0.043$
		18 – 30		$0.315 \pm 0.040 \pm 0.045$
$p_{\text{T}}(J/\psi)$	Backward rapidity $-2.0 < y_{\text{CM}}(J/\psi) < -1.0$	6.5 – 9	[GeV]	$0.177 \pm 0.038 \pm 0.034$
		9 – 12		$0.231 \pm 0.040 \pm 0.043$
		12 – 18		$0.197 \pm 0.044 \pm 0.037$
		18 – 30		$0.250 \pm 0.078 \pm 0.040$
$p_{\text{T}}(J/\psi)$	Midrapidity $-1.0 < y_{\text{CM}}(J/\psi) < 1.0$	6.5 – 9	[GeV]	$0.142 \pm 0.028 \pm 0.027$
		9 – 12		$0.231 \pm 0.027 \pm 0.040$
		12 – 18		$0.273 \pm 0.030 \pm 0.044$
		18 – 30		$0.292 \pm 0.057 \pm 0.042$
$p_{\text{T}}(J/\psi)$	Forward rapidity $1.0 < y_{\text{CM}}(J/\psi) < 1.9$	6.5 – 9	[GeV]	$0.173 \pm 0.025 \pm 0.032$
		9 – 12		$0.238 \pm 0.030 \pm 0.047$
		12 – 18		$0.277 \pm 0.041 \pm 0.048$
		18 – 30		$0.357 \pm 0.085 \pm 0.057$

Table 8.1: Overview of results presented in this work.

Chapter 9

Conclusions

We presented the χ_c-to-J/ψ ratio in $p+\mathrm{Pb}$ collisions at $\sqrt{s_{_{NN}}} = 8.16\,\mathrm{TeV}$, reported as a function of the number of tracks N_{tracks}, rapidity $y_{\mathrm{lab},p}$, and p_{T} in various rapidity bins. The J/ψ particle is reconstructed via its dimuon decay to $\mu^+\,\mu^-$. The χ_c states of χ_{c1} and χ_{c2} are measured together, and reconstructed through $\chi_c \to J/\psi\,\gamma \to \mu^+\,\mu^- + e^+\,e^-$ decay, where the photon is reconstructed as an $e^+\,e^-$ conversion. The χ_c-to-J/ψ ratio is reported in a region constrained by the CMS detector acceptance, ranging from $6.5 < p_{\mathrm{T}}(J/\psi) < 30\,\mathrm{GeV}$ and $-2.4 < y_{\mathrm{lab},p}(J/\psi) < 2.4$. The photon acceptance from the χ_c decay is fully corrected.

The χ_c-to-J/ψ ratio depends on $p_{\mathrm{T}}(J/\psi)$ rising from 0.16 in the lowest-p_{T} bin (6.5-9 GeV) to 0.31 in the highest-p_{T} bin (18-30 GeV). The ratio was found to be flat in rapidity and N_{tracks} when integrated over all accessible $p_{\mathrm{T}}(J/\psi)$, with values of the ratio around 0.20.

We found the ratio to be consistent with two previous $p+p$ measurements at a similar collision energy: with the ATLAS midrapidity results and with the LHCb measurement at forward rapidity. Our results are consistent with no suppression of the χ_c states compared to J/ψ, and suggest weaker dissociation effects compared to the ψ(2S) state.

Appendix A

Conversion selection studies

There have not been any measurements in the CMS heavy-ion group that use the collection of reconstructed conversions in $p+\mathrm{Pb}$ collisions. Therefore, it was necessary to develop and test a selection tailored to our needs. Two approaches were considered: *(i)* A cut-based approach based on the previous $p+p$ analyses (Section A.1), and *(ii)* a machine-learning approach based primarily on boosted decision trees (Section A.2).

A.1 Cut-based methods

The cut-based conversion selection was based on the previous CMS measurements, which were done in the $p+p$ system and at midrapidity $|y_{\mathrm{lab}} < 1|$ only. Therefore, the selection was revisited and optimized for the current analysis. We considered three sets of possible cuts, called *loose*, *medium*, and *tight*. These were defined as follows:

Loose

- *conversion quality*: Only general tracks from the tracker are considered.

- *compatible inner hits*: The two candidate conversion tracks must have one of the two innermost hits in the same detector layer to reduce the contribution of fake conversions due to soft displaced tracks that are spuriously propagated backwards.

- *dz to closest PV*: $dz < 10\,\text{cm}$.

- *min distance of approach (dca)*: $-10\,\text{cm} < dca$. The conversion distance of minimum approach in the xy (transverse) plane, dca, must satisfy the condition -10 cm $< dca$, where dca is the distance between the centers of the two circles made by projecting the track helices onto the transverse plane minus the sum of their radii, $dca = d_{O_1-O_2} - (R_1 + R_2)$. In the ideal case, the tracks would point exactly to the common vertex, and $dca = 0$. Due to the uncertainties, the experimental value has RMS $\approx 0.2\,\text{cm}$. The cut at $-10\,\text{cm}$ removes only conversions with $dca = -999$, which is a placeholder value.

Medium

- *conversion quality*: Same selection criteria as the loose cut.

- *compatible inner hits*: Same selection criteria as the loose cut.

- *dz to closest PV*: Same selection criteria as the loose cut, $dz < 10\,\text{cm}$.

- *min distance of approach*: Same selection criteria as the loose cut, $-10\,\text{cm} < dca$.

- *track 1 and 2 ndf*: The two tracks that were used in creating the conversion are required to have at least four degrees of freedom for the fit in the tracker.

- *conversion vertex probability:* The probability that the tracks come from the same vertex has to be larger than 0.0005.

Tight

- *conversion quality*: Tracks are required to be both general tracks, as well as high purity.
- *compatible inner hits*: Same selection criteria as the loose cut.
- *min distance of approach*: $-0.25\,\text{cm} < dca < 1\,\text{cm}$. The *dca* distribution is asymmetric, but drops off by $-0.25\,\text{cm} < dca < 1\,\text{cm}$. The cut removes only outliers.
- *track 1 and 2 ndf*: The two tracks that were used in creating the conversion are required to have at least four degrees of freedom for the fit in the tracker.
- *conversion vertex probability:* The probability that the tracks come from the same vertex has to be larger than 0.0005.
- *vertex position*: $\rho > 1.5\,\text{cm}$. The vertex is required to be a minimum distance away from the beam axis in the xy-plane.
- *track 1 and 2 sigma to vertex*: $\sigma < 5$. Both the conversion tracks are required to be compatible with the vertex.
- *track 1 and 2* χ^2: Normalized χ^2 for both tracks from the conversion has to be $\chi^2 < 10$.

Note that *dz to closest PV* is not required for the tight selection despite being present for loose and medium, because the tight selection corresponds to the selection used in the previous $p+p$ analyses. The effect of the cut is fairly small, and would not affect the outcome of this study. The cuts are summarized in Table A.1.

The selections were evaluated and results are given in Section A.3. The loose selection was chosen to be the nominal selection. For systematic studies, we also devised "very loose" selection cut to provide us with a less-strict alternative to the nominal selection (as documented in Section 7.1.1).

	Loose (nominal)	**Medium**	**Tight**
conversion quality	only general tracks	only general tracks	gen. tracks & high purity
compatible inner hits	required	required	required
dz to closest PV	$dz < 10\,\text{cm}$	$dz < 10\,\text{cm}$	-
minimum distance of approach	$-10\,\text{cm} < dca$	$-10\,\text{cm} < dca$	$-0.25\,\text{cm} < dca < 1\,\text{cm}$
track 1 and 2 ndf	-	track ndf > 3	track ndf > 3
conversion vertex probability	-	prob > 0.0005	prob > 0.0005
conversion vertex position	-	-	$\rho > 1.5\,\text{cm}$
track1/2 sigma to conv.vertex	-	-	$\sigma < 5$
track1/2 χ^2/ndf	-	-	$\chi^2/ndf < 10$

Table A.1: The three conversion selections used to determine the conversion selection for the analysis.

A.2 MVA methods

In addition to the cut-based selections, various multivariate analysis (MVA) methods from the standard ROOT toolkit for MVA (TMVA) [125] were employed to see if we could improve the efficiency and background rejection. The focus of the study was on various versions of boosted decision trees (BDT), but other methods, such as neural networks and the Fisher discriminant, were also tried. The BDTs are based on ordinary decision trees, where in each tree node, a decision is made based on a single variable x. If x is smaller than some value, the decision tree proceeds to node 1. If x is larger, it proceeds to node 2. In further nodes, another decision is made for a different variable with a different cut-off value (and not necessarily the same variable or cut-off value in node 1 as in node 2). The process continues until a final leaf (terminal node) is reached, at which point all the remaining events are classified either as signal or background. In BDT methods, these decisions are not based on a single tree, but rather on a collection of many individual decision trees created during the training, which are combined into a single classifier at the end. For this study, BDTs with adaptive boost [126] were used. The adaptive boost gives events which are misclassified during training a higher weight for the next round of training, which improves the discriminating power of

the classifier as the training progresses. Additionally, "bagging" is performed for the BDT methods. This re-samples the training data, assigning a random Poisson weight to each event in each of the training steps. The bagging improves the classifier's stability.

We first tried a wide array of possible settings for the available methods. Then, we tested in depth the most encouraging choices from the initial run. The list of the most promising methods that were explored further is:

- **BDT:** For this version of the BDT, we chose a large number of trees in the forest, each tree with a limited depth (800 trees, minimum node size 2.5%, maximum depth = 3).

- **BDT2:** Variant of the BDT with fewer, deeper trees (100 trees, minimum node size 0.5%, maximum depth = 5).

- **BDT3:** A middle-ground BDT variant with 300 trees of maximum depth = 4, minimum node size 2.5%.

- **BDTD:** For this implementation, the BDT is performed in the new variable space, where the input variables are first decorrelated (hence the D in the name). 400 trees of maximum depth = 3, minimum node size 5% are then used.

- **MLP:** An artificial neural network (ANN) was tested in the MLP implementation provided by TMVA. The ANNs consist of simulated interconnected neurons, which produce a response to the input signal. The connections are often organized into layers. The number of layers and details of the neuron connections and response differ depending on the implementation.

- **Fisher:** The method of Fisher discriminants [127] was tried. In the method, the input variables are linearly transformed into a space which separates the two classes of events (signal versus background).

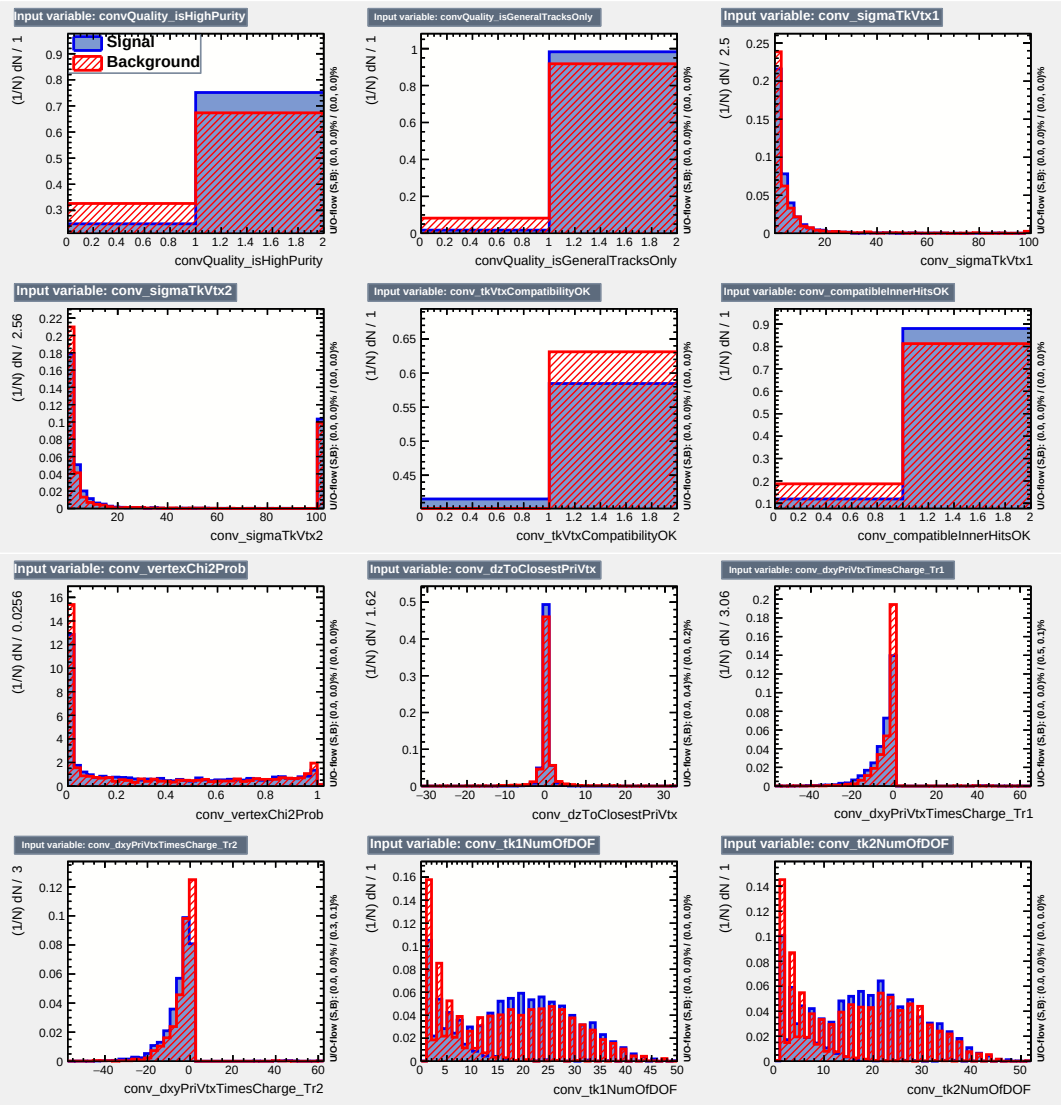

Figure A.1: Example distributions for the variables used in the MVA training. Distributions are in blue for signal and in red for background.

The variables that we considered for the training were all the variables in the *tight* selection as well as others related to conversions. Example variable distributions are shown in Fig. A.1. The training step was done on the same MC samples as evaluation but with different actual events. The MC samples are described in Section A.3.

A.3 Evaluation of methods

The cut-based selections as well as the MVA-based methods were tested on the χ_c MC sample. The signal sample consisted of the actual χ_c decays. The use of proper background sample is challenging in this case, since we are trying to distinguish two things simultaneously: good (real) conversions from bad (fake) conversions, and good conversions that come from χ_c decays from good conversions from elsewhere. We used the same-sign dimuon sample from the official MC as our background sample (that is, dimuons where both muons had the same charge, and were thus from the random combinatorial background). Since the MC events had, on average, about ten times more reconstructed conversions than reconstructed χ_c, a small portion of the conversions in the background sample will be from the actual χ_c and not a real background. However, the majority of photons is from other unrelated sources and therefore represent a proper background in our analysis. Nonetheless, the background sample is not ideal, and more emphasis was placed on the efficiency in the signal sample, which does not suffer from any of these issues. The background rejection (defined as the ratio of conversions failing the cuts for our background sample) should be used mainly for illustrative purposes.

It is important to note that the efficiencies presented here are with respect to these MC samples. Unlike the efficiencies presented in Fig. 6.5 in Section 6.3, all the events here contain a conversion. Therefore, the efficiency is relative only, and does not include the probability of photon converting nor the efficiency of the conversion reconstruction algorithm. The efficiencies test only the effect of cuts applied at the analysis level, i.e. those listed in Table A.1.

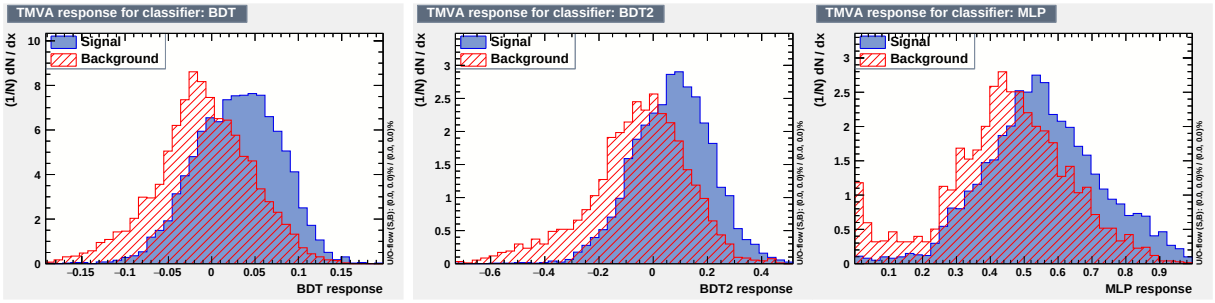

Figure A.2: Distribution of the classifier's values for the testing MC. Signal is in blue. The red distribution corresponds to the background. **Left:** *BDT* method. **Middle:** *BDT2* method. **Right:** *MLP* method.

A.3.1 MVA classifier response

The output from each of the MVA methods is the classifier, a one-dimensional variable on which a simple cut can be placed to distinguish between the signal and background. The classifier's response was tested on the MC sample described above in Section A.3. The distributions of values for a classifier from a few methods are shown in Fig. A.2. The response to the real χ_c conversions is in blue and the background response is in red. In the ideal case, the distributions would be clearly separated. However, in reality, there is some overlap. A background contamination is present, however we choose the cut-off.

Figure A.3 shows the potential efficiency as a function of the cut-off value that would be chosen for the given classifier. The blue line is the signal efficiency, which we want to be as close to one as possible. The red line is the background "efficiency", which is a value we want to be as close to zero as possible to reject the background. The green line is the signal significance defined as $S/\sqrt{S+B}$. The significance is the value we usually want to maximize in the analysis. The optimal cut for maximum significance depends on the expected signal and background. For the same response, if we have a lot of background, we need to have a stricter cut, in order not to be overwhelmed by background. On the other hand, if the background level is very low, a very strict cut would unnecessarily remove mostly signal.

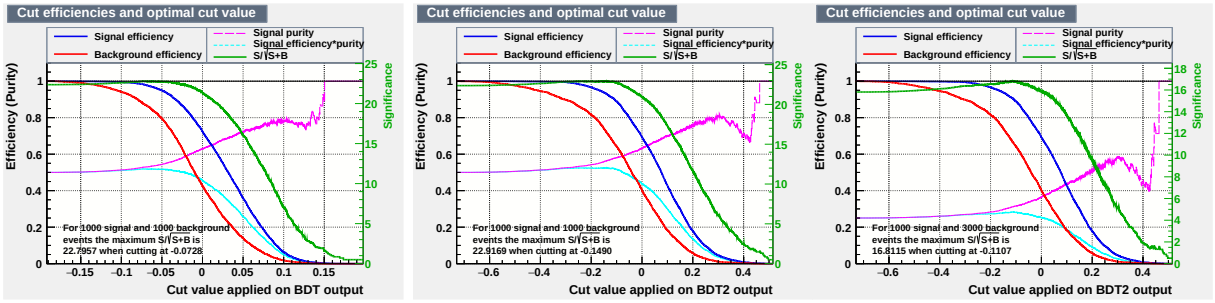

Figure A.3: Examples of response as a function of chosen classifier cut value. Signal efficiency is shown as a blue line, the red line is the background efficiency (1-rejection rate). Green is the significance, and its $y-$axis is on the right side. **Left:** "BDT" method. **Middle:** "BDT2" method. **Right:** Also "BDT2" method, but for different background expectation. Details are in the text.

This is illustrated by the middle and right panel, which both show the BDT2 classifier. The middle panel shows the results when we expect 1000 signal events and 1000 background events. In such a case, the ideal significance is obtained with a cut of -0.15. The right panel shows the results when 3000 background events are expected instead. The best significance is expected at a stricter cut of -0.11 (and is lower, due to the increased background). In all the panels, the magenta and the cyan lines depict signal purity defined as a fraction of passing events that are signal, and efficiency times purity, respectively. Similar to signal significance, both of these values also depend on the signal/background ratio.

Figure A.4 shows the ROC curve (receiver operating characteristic, plotting the signal efficiency versus background rejection for the classifier) for the various TMVA methods, as well as the location of the three cut-based selections that we considered. The signal efficiency for the tight selection was 29%, for the medium 56%, and for the loose 87%, where the denominators are the reconstructed χ_c without any cuts on conversions, but where a conversion coming from χ_c was reconstructed. The loose selection provides discriminating power that is only a little worse than the best of the MVA methods and was thus chosen to be used in the analysis.

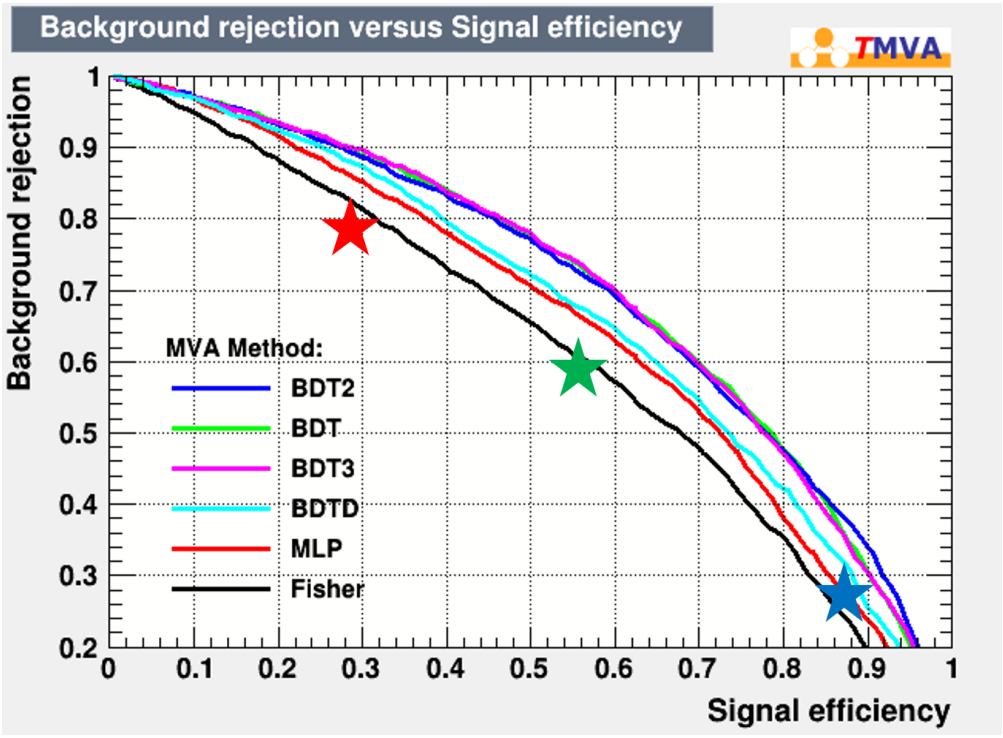

Figure A.4: Evaluation of the various selection methods for the conversions. The horizontal axis shows efficiency, while the zero-suppressed vertical axis shows the background rejection. The red star is *tight* selection, the green is *medium*, and the blue is *loose*.

The conclusions were validated by using the selections on real data, fitting the invariant mass distributions with signal and background functions, and then comparing the resulting yields with the predictions from the MC. The results are shown in Fig. A.5 for a particular bin ($50 < N_{\text{tracks}} < 100$, $|y_{\text{lab}}| < 1$). The crosscheck agreed with the prediction - a loose selection provided the most significant yields from the cut-based selections. There was a minor improvement in signal significance using the BDT2 method ($\approx 10 - 15\%$). However, it was not deemed sufficient to warrant the increased complexity from using the MVA and the challenges coming from the need for a proper background training sample.

As an additional crosscheck, the rapidity dependence of the proposed selections was studied. The results are shown in Fig. A.6. The plot shows the MC efficiency for the conversion,

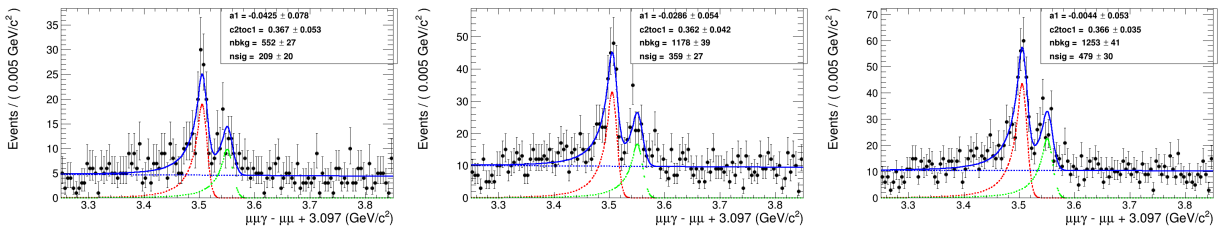

Figure A.5: Example of the fit to an invariant mass spectrum in real data. **Left:** The conversions were selected using the "medium" cut-based selection. **Middle:** The conversions were selected using the "loose" cut-based selection. This is the nominal selection. **Right:** The conversions were selected using the *BDT2* method. Using the the fits, the nsig/σ_{nsig} values for this bin are 10, 13, and 16, respectively. The improvements of the BDT over the nominal selection varies for bins in different kinematic regions, but the significance, on average, improved by $\approx 10-15\%$, and similar improvement can be seen in the χ_{c2}-to-χ_{c1} ratio uncertainties ("c2toc1" in the fits).

assuming that the conversion happened in the first place and exists in the conversion collection. The results show that for the loose selection, the rapidity dependence is mostly flat. This is not true for the medium and the tight selections. While not strictly necessary, the fact that the efficiency of the nominal selection does not show a rapidity trend is beneficial for the analysis' robustness.

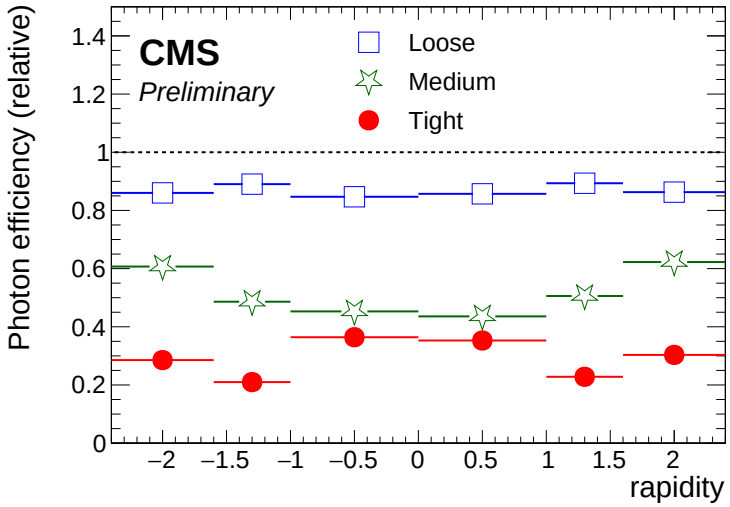

Figure A.6: Evaluation of the various selection methods for the conversions in the MC as a function of conversion rapidity. The red is the tight selection, the green is the medium, and the blue is the loose.

Appendix B

Additional crosschecks

B.1 $p + \mathrm{Pb}$ vs $\mathrm{Pb} + p$ direction

The $p + \mathrm{Pb}$ run consisted of two periods, separated by when the directions of the p and the Pb beam were reversed. The beam reversal helps to mitigate any systematic effects a from non-symmetric detector. While the Monte Carlo samples are weighted by the luminosity of the individual pPb/Pbp periods (see Section 4.3), it is useful to check if any asymmetries are present between the runs. The left panel of Fig. B.1 shows the overall reconstruction efficiency for χ_c states. In addition, the reconstruction efficiency of photons (i.e. chance that a photon will be reconstructed as a conversion, without any selection) is in the middle, which is the dominant contribution to the correction for the χ_c-to-J/ψ ratio. This efficiency also includes the probability that the photon will convert in the detector. The right plot shows the efficiency of the loose photon selection described in Section 5.1.3 in the case that the conversion exists. The efficiencies are symmetric, which further improves our confidence that we do not introduce any biases by combining the $p + \mathrm{Pb}$ and $\mathrm{Pb} + p$ portions of the run.

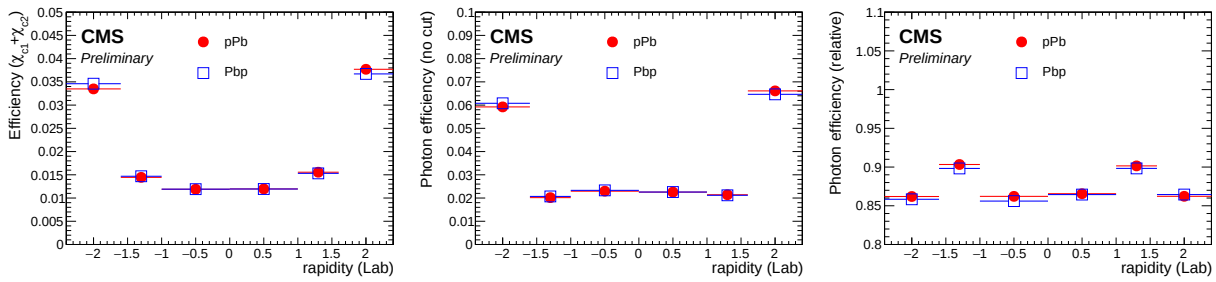

Figure B.1: Comparison of the efficiencies for the p+Pb and Pb+p portions of the overall data sample. **Left:** χ_c efficiency. **Middle:** photon conversion reconstruction efficiency (no selection). **Right:** Loose conversion selection assuming the photon converted and was reconstructed.

B.2 Dependence of efficiency on N_{tracks}

We explored the N_{tracks}-dependent correction to the overall χ_c-to-J/ψ ratio in Section 6. However, it is also important to check the dependence of the efficiencies themselves, as many trends cancel out in the ratio. The single particle efficiencies are shown in Fig. B.2. The left panel shows the efficiency of the photon reconstruction, with two data sets - the loose selection (nominal) in blue squares and the tight in red. There is a noticeable dependence on the number of tracks for both selections. Both selections exhibit the same trend when accounting for the larger overall efficiency of the loose selection. The middle panel displays the N_{tracks} dependence of the reconstruction efficiency for J/ψ. The efficiency is essentially flat across the full range of N_{tracks}. The right panel shows the dependence for χ_c. Its shape is largely a combination of the left (conversion) and the middle (J/ψ) panels, even though there are a few additional χ_c-specific cuts (see Section 5.1 for details). We observe that the χ_c efficiency decreases with N_{tracks}, a trend that comes mainly from the conversion efficiency. It is thus important to use the properly weighted MC sample for any corrections that are integrated over the N_{tracks} variable. See the Section 4.3 for details of the weighting procedure.

Technical note: The number of tracks in the figure is slightly different in Fig. B.2

than in the plots for our physics results. The results use the number of tracks coming from the primary vertex associated with the J/ψ and thus with χ_c. However, that information is available only after the event reconstruction step, and does not exist directly in the generated MC. It is thus unavailable for those χ_c, J/ψ or photons that were not reconstructed. Since these plots show the ratios of reconstructed to the generated, the denominator often does not have the reconstruction information. Therefore, for this figure the standard N_{tracks} *in event* was used, where the greatest PV vertex is assumed. This is the same vertex for the vast majority of events, and differs only rarely when the χ_c actually comes from a small primary vertex when another larger primary vertex is present in the same event (see Section 5.2.1.2 and especially Fig. 5.3 for details). The difference is negligible and does not affect the conclusions.

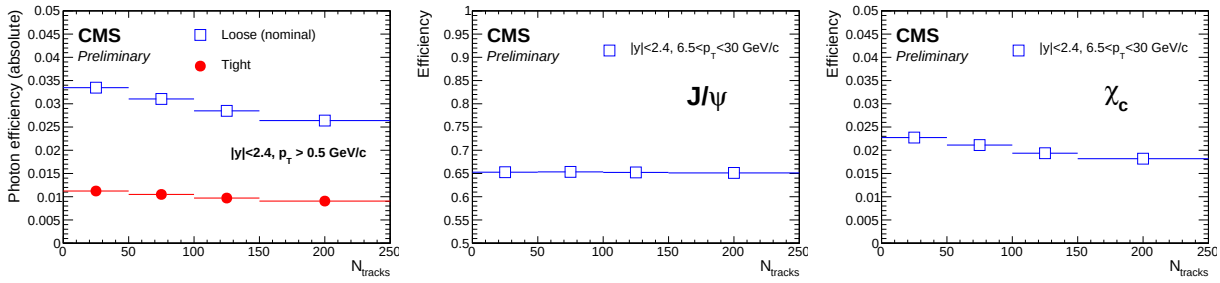

Figure B.2: Efficiency dependence on the number of tracks in the event. **Left:** Photon efficiency for loose (nominal) and tight conversion selections. **Middle:** J/ψ efficiency. **Right:** Overall χ_c reconstruction efficiency.

Bibliography

[1] J. C. Collins and M. J. Perry. "Superdense Matter: Neutrons or Asymptotically Free Quarks?" In: *Phys. Rev. Lett.* 34 (21 May 1975), pp. 1353–1356. DOI: 10.1103/PhysRevLett.34.1353. URL: https://link.aps.org/doi/10.1103/PhysRevLett.34.1353.

[2] N. Cabibbo and G. Parisi. "Exponential Hadronic Spectrum and Quark Liberation." In: *Phys. Lett. B* 59 (1975), pp. 67–69. DOI: 10.1016/0370-2693(75)90158-6.

[3] Alexander M. Polyakov. "Thermal Properties of Gauge Fields and Quark Liberation." In: *Phys. Lett. B* 72 (1978), pp. 477–480. DOI: 10.1016/0370-2693(78)90737-2.

[4] Leonard Susskind. "Lattice Models of Quark Confinement at High Temperature." In: *Phys. Rev. D* 20 (1979), pp. 2610–2618. DOI: 10.1103/PhysRevD.20.2610.

[5] Ulrich W. Heinz and Maurice Jacob. "Evidence for a new state of matter: An Assessment of the results from the CERN lead beam program." In: (Jan. 2000). arXiv: nucl-th/0002042.

[6] I. Arsene et al. "Quark gluon plasma and color glass condensate at RHIC? The Perspective from the BRAHMS experiment." In: *Nucl. Phys. A* 757 (2005), pp. 1–27. DOI: 10.1016/j.nuclphysa.2005.02.130. arXiv: nucl-ex/0410020.

[7] K. Adcox et al. "Formation of dense partonic matter in relativistic nucleus-nucleus collisions at RHIC: Experimental evaluation by the PHENIX collaboration." In: *Nucl.*

Phys. A 757 (2005), pp. 184–283. DOI: 10.1016/j.nuclphysa.2005.03.086. arXiv: nucl-ex/0410003.

[8] B. B. Back et al. "The PHOBOS perspective on discoveries at RHIC." In: *Nucl. Phys. A* 757 (2005), pp. 28–101. DOI: 10.1016/j.nuclphysa.2005.03.084. arXiv: nucl-ex/0410022.

[9] John Adams et al. "Experimental and theoretical challenges in the search for the quark gluon plasma: The STAR Collaboration's critical assessment of the evidence from RHIC collisions." In: *Nucl. Phys. A* 757 (2005), pp. 102–183. DOI: 10.1016/j.nuclphysa.2005.03.085. arXiv: nucl-ex/0501009.

[10] D. J. Gross and F. Wilczek. "Ultraviolet Behavior of Non-Abelian Gauge Theories." In: *Phys. Rev. Lett.* 30 (26 June 1973), pp. 1343–1346. DOI: 10.1103/PhysRevLett.30.1343. URL: https://link.aps.org/doi/10.1103/PhysRevLett.30.1343.

[11] H. David Politzer. "Asymptotic Freedom: An Approach to Strong Interactions." In: *Phys. Rept.* 14 (1974), pp. 129–180. DOI: 10.1016/0370-1573(74)90014-3.

[12] T. Matsui and H. Satz. "J/ψ Suppression by Quark-Gluon Plasma Formation." In: *Phys. Lett. B* 178 (1986), pp. 416–422. DOI: 10.1016/0370-2693(86)91404-8.

[13] F. Karsch, M. T. Mehr, and H. Satz. "Color Screening and Deconfinement for Bound States of Heavy Quarks." In: *Z. Phys. C* 37 (1988), p. 617. DOI: 10.1007/BF01549722.

[14] F. Abe et al. "Observation of top quark production in $\bar{p}p$ collisions." In: *Phys. Rev. Lett.* 74 (1995), pp. 2626–2631. DOI: 10.1103/PhysRevLett.74.2626. arXiv: hep-ex/9503002.

[15] S. Abachi et al. "Observation of the top quark." In: *Phys. Rev. Lett.* 74 (1995), pp. 2632–2637. DOI: 10.1103/PhysRevLett.74.2632. arXiv: hep-ex/9503003.

[16] K. Kodama et al. "Observation of tau neutrino interactions." In: *Phys. Lett. B* 504 (2001), pp. 218–224. DOI: 10.1016/S0370-2693(01)00307-0. arXiv: hep-ex/0012035.

[17] Serguei Chatrchyan et al. "Observation of a New Boson at a Mass of 125 GeV with the CMS Experiment at the LHC." In: *Phys. Lett. B* 716 (2012), pp. 30–61. DOI: 10.1016/j.physletb.2012.08.021. arXiv: 1207.7235 [hep-ex].

[18] Georges Aad et al. "Observation of a new particle in the search for the Standard Model Higgs boson with the ATLAS detector at the LHC." In: *Phys. Lett. B* 716 (2012), pp. 1–29. DOI: 10.1016/j.physletb.2012.08.020. arXiv: 1207.7214 [hep-ex].

[19] J. Engels, F. Karsch, and K. Redlich. "Scaling properties of the energy density in SU(2) lattice gauge theory." In: *Nucl. Phys. B* 435 (1995), pp. 295–310. DOI: 10.1016/0550-3213(94)00491-V. arXiv: hep-lat/9408009.

[20] Frithjof Karsch. "Lattice results on QCD thermodynamics." In: *Nucl. Phys. A* 698 (2002). Ed. by T. J. Hallman et al., pp. 199–208. DOI: 10.1016/S0375-9474(01)01365-3. arXiv: hep-ph/0103314.

[21] M. Asakawa and K. Yazaki. "Chiral Restoration at Finite Density and Temperature." In: *Nucl. Phys. A* 504 (1989), pp. 668–684. DOI: 10.1016/0375-9474(89)90002-X.

[22] K. Kajantie et al. "Is there a hot electroweak phase transition at $m_H \gtrsim m_W$?" In: *Phys. Rev. Lett.* 77 (1996), pp. 2887–2890. DOI: 10.1103/PhysRevLett.77.2887. arXiv: hep-ph/9605288.

[23] M. M. Aggarwal et al. "An Experimental Exploration of the QCD Phase Diagram: The Search for the Critical Point and the Onset of De-confinement." In: (July 2010). arXiv: 1007.2613 [nucl-ex].

[24] S. L. Olsen, T. Skwarnicki, and D. Zieminska. "Nonstandard heavy mesons and baryons: Experimental evidence." In: *Rev. Mod. Phys.* 90.1 (2018), p. 015003. DOI: 10.1103/RevModPhys.90.015003. arXiv: 1708.04012 [hep-ph].

[25] R. Vogt. *Ultrarelativistic Heavy-Ion Collisions*. Ed. by Ramona Vogt. Amsterdam: Elsevier Science B.V., 2007, pp. 385–426. ISBN: 978-0-444-52196-5. DOI: https://doi.org/10.1016/B978-044452196-5/50008-6. URL: https://www.sciencedirect.com/science/article/pii/B9780444521965500086.

[26] T. Barnes, S. Godfrey, and E. S. Swanson. "Higher charmonia." In: *Phys. Rev. D* 72 (2005), p. 054026. DOI: 10.1103/PhysRevD.72.054026. arXiv: hep-ph/0505002.

[27] J. E. Augustin et al. "Discovery of a Narrow Resonance in e^+e^- Annihilation." In: *Phys. Rev. Lett.* 33 (1974), pp. 1406–1408. DOI: 10.1103/PhysRevLett.33.1406.

[28] J. J. Aubert et al. "Experimental Observation of a Heavy Particle J." In: *Phys. Rev. Lett.* 33 (1974), pp. 1404–1406. DOI: 10.1103/PhysRevLett.33.1404.

[29] R. L. Workman et al. "Review of Particle Physics." In: *PTEP* 2022 (2022), p. 083C01. DOI: 10.1093/ptep/ptac097.

[30] Helmut Satz. "Quarkonium Binding and Dissociation: The Spectral Analysis of the QGP." In: *Nucl.Phys.* A783 (2007), pp. 249–260. DOI: 10.1016/j.nuclphysa.2006.11.026. arXiv: hep-ph/0609197 [hep-ph].

[31] E. Eichten et al. "Charmonium: The Model." In: *Phys. Rev. D* 17 (1978). [Erratum: Phys.Rev.D 21, 313 (1980)], p. 3090. DOI: 10.1103/PhysRevD.17.3090.

[32] M. Laine et al. "Real-time static potential in hot QCD." In: *JHEP* 03 (2007), p. 054. DOI: 10.1088/1126-6708/2007/03/054. arXiv: hep-ph/0611300.

[33] Kenneth G. Wilson. "Confinement of quarks." In: *Phys. Rev. D* 10 (8 Oct. 1974), pp. 2445–2459. DOI: 10.1103/PhysRevD.10.2445. URL: https://link.aps.org/doi/10.1103/PhysRevD.10.2445.

[34] Jens O. Andersen, Eric Braaten, and Michael Strickland. "Hard thermal loop resummation of the thermodynamics of a hot gluon plasma." In: *Phys. Rev. D* 61 (2000), p. 014017. DOI: 10.1103/PhysRevD.61.014017. arXiv: hep-ph/9905337.

[35] A. Beraudo, J. -P. Blaizot, and C. Ratti. "Real and imaginary-time Q anti-Q correlators in a thermal medium." In: *Nucl. Phys. A* 806 (2008), pp. 312–338. DOI: 10.1016/j.nuclphysa.2008.03.001. arXiv: 0712.4394 [nucl-th].

[36] Alexander Rothkopf, Tetsuo Hatsuda, and Shoichi Sasaki. "Complex Heavy-Quark Potential at Finite Temperature from Lattice QCD." In: *Phys. Rev. Lett.* 108 (2012), p. 162001. DOI: 10.1103/PhysRevLett.108.162001. arXiv: 1108.1579 [hep-lat].

[37] Yannis Burnier, Olaf Kaczmarek, and Alexander Rothkopf. "Static quark-antiquark potential in the quark-gluon plasma from lattice QCD." In: *Phys. Rev. Lett.* 114.8 (2015), p. 082001. DOI: 10.1103/PhysRevLett.114.082001. arXiv: 1410.2546 [hep-lat].

[38] R. Baier and R. Ruckl. "Hadronic Collisions: A Quarkonium Factory." In: *Z. Phys. C* 19 (1983), p. 251. DOI: 10.1007/BF01572254.

[39] F. Abe et al. "Production of J/ψ Mesons from χ_c Meson Decays in $p\overline{p}$ Collisions at $\sqrt{s} = 1.8$TeV." In: *Phys. Rev. Lett.* 79 (4 July 1997), pp. 578–583. DOI: 10.1103/PhysRevLett.79.578. URL: https://link.aps.org/doi/10.1103/PhysRevLett.79.578.

[40] G. Peter Lepage et al. "Improved nonrelativistic QCD for heavy quark physics." In: *Phys. Rev. D* 46 (1992), pp. 4052–4067. DOI: 10.1103/PhysRevD.46.4052. arXiv: hep-lat/9205007.

[41] Geoffrey T. Bodwin, Eric Braaten, and G. Peter Lepage. "Rigorous QCD analysis of inclusive annihilation and production of heavy quarkonium." In: *Phys. Rev. D* 51 (1995). [Erratum: Phys.Rev.D 55, 5853 (1997)], pp. 1125–1171. DOI: 10.1103/PhysRevD.55.5853. arXiv: hep-ph/9407339.

[42] J. F. Amundson et al. "Colorless states in perturbative QCD: Charmonium and rapidity gaps." In: *Phys. Lett. B* 372 (1996), pp. 127–132. DOI: 10.1016/0370-2693(96)00035-4. arXiv: hep-ph/9512248.

[43] J. F. Amundson et al. "Quantitative tests of color evaporation: Charmonium production." In: *Phys. Lett. B* 390 (1997), pp. 323–328. DOI: 10.1016/S0370-2693(96)01417-7. arXiv: hep-ph/9605295.

[44] Yan-Qing Ma and Ramona Vogt. "Quarkonium Production in an Improved Color Evaporation Model." In: *Phys. Rev. D* 94.11 (2016), p. 114029. DOI: 10.1103/PhysRevD.94.114029. arXiv: 1609.06042 [hep-ph].

[45] Vardan Khachatryan et al. "Observation of Long-Range Near-Side Angular Correlations in Proton-Proton Collisions at the LHC." In: *JHEP* 09 (2010), p. 091. DOI: 10.1007/JHEP09(2010)091. arXiv: 1009.4122 [hep-ex].

[46] Kevin Dusling, Wei Li, and Björn Schenke. "Novel collective phenomena in high-energy proton–proton and proton–nucleus collisions." In: *Int. J. Modern Physics E* 25.01 (2016), p. 1630002. DOI: 10.1142/S0218301316300022. arXiv: 1509.07939 [nucl-ex].

[47] R.J. Glauber. "High energy collision theory." In: *Lectures in Theoretical Physics* 1 (1959), pp. 315–414.

[48] Michael L. Miller et al. "Glauber modeling in high energy nuclear collisions." In: *Ann. Rev. Nucl. Part. Sci.* 57 (2007), pp. 205–243. DOI: 10.1146/annurev.nucl.57.090506.123020. arXiv: nucl-ex/0701025.

[49] Constantin Loizides, Jason Kamin, and David d'Enterria. "Improved Monte Carlo Glauber predictions at present and future nuclear colliders." In: *Phys. Rev. C* 97.5 (2018). [Erratum: Phys. Rev. C 99, 019901 (2019)], p. 054910. DOI: 10.1103/PhysRevC.97.054910. arXiv: 1710.07098 [nucl-ex].

[50] Georges Aad et al. "Measurement of Z boson Production in Pb+Pb Collisions at $\sqrt{s_{NN}} = 2.76$ TeV with the ATLAS Detector." In: *Phys. Rev. Lett.* 110.2 (2013), p. 022301. DOI: 10.1103/PhysRevLett.110.022301. arXiv: 1210.6486 [hep-ex].

[51] Serguei Chatrchyan et al. "Study of Z production in PbPb and pp collisions at $\sqrt{s_{\mathrm{NN}}} = 2.76$ TeV in the dimuon and dielectron decay channels." In: *JHEP* 03 (2015), p. 022. DOI: 10.1007/JHEP03(2015)022. arXiv: 1410.4825 [nucl-ex].

[52] Georges Aad et al. "Z boson production in Pb+Pb collisions at $\sqrt{s_{\mathrm{NN}}}$= 5.02 TeV measured by the ATLAS experiment." In: *Phys. Lett. B* 802 (2020), p. 135262. DOI: 10.1016/j.physletb.2020.135262. arXiv: 1910.13396 [nucl-ex].

[53] Georges Aad et al. "Measurement of $W^{\pm}$ boson production in Pb+Pb collisions at $\sqrt{s_{\mathrm{NN}}} = 5.02$ TeV with the ATLAS detector." In: *Eur. Phys. J. C* 79.11 (2019), p. 935. DOI: 10.1140/epjc/s10052-019-7439-3. arXiv: 1907.10414 [nucl-ex].

[54] Serguei Chatrchyan et al. "Study of W boson production in PbPb and pp collisions at $\sqrt{s_{NN}} = 2.76$ TeV." In: *Phys. Lett. B* 715 (2012), pp. 66–87. DOI: 10.1016/j.physletb.2012.07.025. arXiv: 1205.6334 [nucl-ex].

[55] Sourendu Gupta and Helmut Satz. "Final state J/ψ suppression in nuclear collisions." In: *AIP Conference Proceedings* 272.1 (1992), pp. 991–999. DOI: 10.1063/1.43254.

[56] Peter Braun-Munzinger and Johanna Stachel. "On charm production near the phase boundary." In: *Nucl. Phys. A* 690 (2001). Ed. by P. Braun-Munzinger and A. Zilges, pp. 119–126. DOI: 10.1016/S0375-9474(01)00936-8. arXiv: nucl-th/0012064.

[57] L. Grandchamp and R. Rapp. "Thermal versus direct J / Psi production in ultrarelativistic heavy ion collisions." In: *Phys. Lett. B* 523 (2001), pp. 60–66. DOI: 10.1016/S0370-2693(01)01311-9. arXiv: hep-ph/0103124.

[58] Robert L. Thews, Martin Schroedter, and Johann Rafelski. "Enhanced J/ψ production in deconfined quark matter." In: *Phys. Rev. C* 63 (2001), p. 054905. DOI: 10.1103/PhysRevC.63.054905. arXiv: hep-ph/0007323.

[59] A. Andronic et al. "Statistical hadronization of charm in heavy ion collisions at SPS, RHIC and LHC." In: *Phys. Lett. B* 571 (2003), pp. 36–44. DOI: 10.1016/j.physletb.2003.07.066. arXiv: nucl-th/0303036.

[60] Richard D. Ball et al. "Parton distributions from high-precision collider data." In: *Eur. Phys. J. C* 77.10 (2017), p. 663. DOI: 10.1140/epjc/s10052-017-5199-5. arXiv: 1706.00428 [hep-ph].

[61] P. Skands, S. Carrazza, and J. Rojo. "Tuning PYTHIA 8.1: the Monash 2013 tune." In: *The European Physical Journal C* 74.8 (Aug. 2014). DOI: 10.1140/epjc/s10052-014-3024-y. URL: https://doi.org/10.1140%2Fepjc%2Fs10052-014-3024-y.

[62] V. N. Gribov and L. N. Lipatov. "Deep inelastic e p scattering in perturbation theory." In: *Sov. J. Nucl. Phys.* 15 (1972), pp. 438–450.

[63] Yuri L. Dokshitzer. "Calculation of the Structure Functions for Deep Inelastic Scattering and e+ e- Annihilation by Perturbation Theory in Quantum Chromodynamics." In: *Sov. Phys. JETP* 46 (1977), pp. 641–653.

[64] Guido Altarelli and G. Parisi. "Asymptotic Freedom in Parton Language." In: *Nucl. Phys. B* 126 (1977), pp. 298–318. DOI: 10.1016/0550-3213(77)90384-4.

[65] Rabah Abdul Khalek et al. "nNNPDF3.0: evidence for a modified partonic structure in heavy nuclei." In: *Eur. Phys. J. C* 82.6 (2022), p. 507. DOI: 10.1140/epjc/s10052-022-10417-7. arXiv: 2201.12363 [hep-ph].

[66] A. Capella et al. "J / psi and psi-prime suppression in heavy ion collisions." In: *Phys. Lett. B* 393 (1997), pp. 431–436. DOI: 10.1016/S0370-2693(96)01650-4. arXiv: hep-ph/9607265.

[67] E. G. Ferreiro. "Charmonium dissociation and recombination at LHC: Revisiting comovers." In: *Phys. Lett. B* 731 (2014), pp. 57–63. DOI: 10.1016/j.physletb.2014.02.011. arXiv: 1210.3209 [hep-ph].

[68] Xiaojian Du and Ralf Rapp. "In-Medium Charmonium Production in Proton-Nucleus Collisions." In: *JHEP* 03 (2019), p. 015. DOI: 10.1007/JHEP03(2019)015. arXiv: 1808.10014 [nucl-th].

[69] Carlos Lourenco, Ramona Vogt, and Hermine K. Woehri. "Energy dependence of J/psi absorption in proton-nucleus collisions." In: *JHEP* 02 (2009), p. 014. DOI: 10.1088/1126-6708/2009/02/014. arXiv: 0901.3054 [hep-ph].

[70] Francois Arleo, Stephane Peigne, and Taklit Sami. "Revisiting scaling properties of medium-induced gluon radiation." In: *Phys. Rev. D* 83 (2011), p. 114036. DOI: 10.1103/PhysRevD.83.114036. arXiv: 1006.0818 [hep-ph].

[71] Francois Arleo and Stephane Peigne. "Heavy-quarkonium suppression in p-A collisions from parton energy loss in cold QCD matter." In: *JHEP* 03 (2013), p. 122. DOI: 10.1007/JHEP03(2013)122. arXiv: 1212.0434 [hep-ph].

[72] François Arleo et al. "Centrality and pT dependence of J/psi suppression in proton-nucleus collisions from parton energy loss." In: *JHEP* 05 (2013), p. 155. DOI: 10.1007/JHEP05(2013)155. arXiv: 1304.0901 [hep-ph].

[73] François Arleo and Stéphane Peigné. "Quarkonium suppression in heavy-ion collisions from coherent energy loss in cold nuclear matter." In: *JHEP* 10 (2014), p. 073. DOI: 10.1007/JHEP10(2014)073. arXiv: 1407.5054 [hep-ph].

[74] R Aaij et al. "Measurement of the ratio of prompt χ_c to J/ψ production in pp collisions at $\sqrt{s} = 7$ TeV." In: *Phys. Lett. B* 718 (2012), pp. 431–440. DOI: 10.1016/j.physletb.2012.10.068. arXiv: 1204.1462 [hep-ex].

[75] L. A. Harland-Lanf and W. J. Stirling. "CHIGEN: Monte Carlo Event Generator for inclusive χ_{cJ} production." URL: http://projects.hepforge.org/superchic/chigen.html.

[76] Yan-Qing Ma, Kai Wang, and Kuang-Ta Chao. "QCD radiative corrections to χ_{cJ} production at hadron colliders." In: *Phys. Rev. D* 83 (2011), p. 111503. DOI: 10.1103/PhysRevD.83.111503. arXiv: 1002.3987 [hep-ph].

[77] R. Aaij et al. "Measurement of the cross-section ratio $\sigma(\chi_{c2})/\sigma(\chi_{c1})$ for prompt χ_c production at $\sqrt{s} = 7$ TeV." In: *Phys. Lett. B* 714 (2012), pp. 215–223. DOI: 10.1016/j.physletb.2012.06.077. arXiv: 1202.1080 [hep-ex].

[78] A. Abulencia et al. "Measurement of $\sigma_{\chi_{c2}} B(\chi_{c2} \to J/\psi\gamma)/\sigma_{\chi_{c1}} B(\chi_{c1} \to J/\psi\gamma)$ in $p\bar{p}$ Collisions at $\sqrt{s} = 1.96$-TeV." In: *Phys. Rev. Lett.* 98 (2007), p. 232001. DOI: 10.1103/PhysRevLett.98.232001. arXiv: hep-ex/0703028.

[79] Georges Aad et al. "Measurement of χ_{c1} and χ_{c2} production with $\sqrt{s} = 7$ TeV pp collisions at ATLAS." In: *JHEP* 07 (2014), p. 154. DOI: 10.1007/JHEP07(2014)154. arXiv: 1404.7035 [hep-ex].

[80] Serguei Chatrchyan et al. "Measurement of the Relative Prompt Production Rate of χ_{c2} and χ_{c1} in pp Collisions at $\sqrt{s} = 7$ TeV." In: *Eur. Phys. J. C* 72 (2012), p. 2251. DOI: 10.1140/epjc/s10052-012-2251-3. arXiv: 1210.0875 [hep-ex].

[81] I. Abt et al. "Production of the Charmonium States χ_{c1} and χ_{c2} in Proton Nucleus Interactions at $\sqrt{s} = 41.6$-GeV." In: *Phys. Rev. D* 79 (2009), p. 012001. DOI: 10.1103/PhysRevD.79.012001. arXiv: 0807.2167 [hep-ex].

[82] R. Aaij et al. "Measurement of prompt-production cross-section ratio $\sigma(\chi_{c2})/\sigma(\chi_{c1})$ in pPb collisions at $\sqrt{s_{NN}} = 8.16$ TeV." In: *Phys. Rev. C* 103 (2021), p. 064905. DOI: 10.1103/PhysRevC.103.064905. arXiv: 2103.07349 [hep-ex].

[83] R. Aaij et al. "Measurement of the relative rate of prompt χ_{c0}, χ_{c1} and χ_{c2} production at $\sqrt{s} = 7$TeV." In: *JHEP* 10 (2013), p. 115. DOI: 10.1007/JHEP10(2013)115. arXiv: 1307.4285 [hep-ex].

[84] A. Adare et al. "Nuclear Modification of ψ', χ_c, and J/ψ Production in d+Au Collisions at $\sqrt{s_{NN}}$=200 GeV." In: *Phys. Rev. Lett.* 111.20 (2013), p. 202301. DOI: 10.1103/PhysRevLett.111.202301. arXiv: 1305.5516 [nucl-ex].

[85] Jaroslav Adam et al. "Centrality dependence of ψ(2S) suppression in p-Pb collisions at $\sqrt{s_{\rm NN}} = 5.02$ TeV." In: *JHEP* 06 (2016), p. 050. DOI: 10.1007/JHEP06(2016)050. arXiv: 1603.02816 [nucl-ex].

[86] Xiaojian Du and Ralf Rapp. "Sequential Regeneration of Charmonia in Heavy-Ion Collisions." In: *Nucl. Phys. A* 943 (2015), pp. 147–158. DOI: 10.1016/j.nuclphysa.2015.09.006. arXiv: 1504.00670 [hep-ph].

[87] E. G. Ferreiro. "Excited charmonium suppression in proton-nucleus collisions as a consequence of comovers." In: *Phys. Lett. B* 749 (2015), pp. 98–103. DOI: 10.1016/j.physletb.2015.07.066. arXiv: 1411.0549 [hep-ph].

[88] Betty Bezverkhny Abelev et al. "Suppression of ψ(2S) production in p-Pb collisions at $\sqrt{s_{\mathrm{NN}}} = 5.02$ TeV." In: *JHEP* 12 (2014), p. 073. DOI: 10.1007/JHEP12(2014)073. arXiv: 1405.3796 [nucl-ex].

[89] Maximilien Brice. "Aerial View of the CERN taken in 2008." 2008. URL: http://cds.cern.ch/record/1295244.

[90] Ewa Lopienska. *The CERN accelerator complex, layout in 2022. Complexe des accélérateurs du CERN en janvier 2022*. General Photo. 2022. URL: https://cds.cern.ch/record/2800984.

[91] S. Chatrchyan et al. "The CMS Experiment at the CERN LHC." In: *JINST* 3 (2008), S08004. DOI: 10.1088/1748-0221/3/08/S08004.

[92] David Barney and Sergio Cittolin. *CMS Detector Drawings*. 2010. URL: https://cds.cern.ch/record/2629816.

[93] The CMS Collaboration. "Description and performance of track and primary-vertex reconstruction with the CMS tracker." In: *Journal of Instrumentation* 9.10 (2014), P10009–P10009. DOI: 10.1088/1748-0221/9/10/p10009. URL: https://doi.org/10.1088%2F1748-0221%2F9%2F10%2Fp10009.

[94] The Tracker Group Of The CMS Collaboration. *The CMS Phase-1 Pixel Detector Upgrade*. 2020. DOI: 10.48550/ARXIV.2012.14304. URL: https://arxiv.org/abs/2012.14304.

[95] M Brice. "Images of the CMS ECAL Barrel (EB)." CMS Collection. 2008. URL: https://cds.cern.ch/record/1431477.

[96] "Performance of the CMS Muon Detectors in 2016 collision runs." In: (2016). URL: http://cds.cern.ch/record/2202964.

[97] CMS Collaboration. "Performance of the CMS drift tube chambers with cosmic rays." In: *Journal of Instrumentation* 5.03 (2010), T03015–T03015. DOI: 10.1088/1748-0221/5/03/t03015. URL: https://doi.org/10.1088%2F1748-0221%2F5%2F03%2Ft03015.

[98] "The CMS muon project: Technical Design Report." In: (1997).

[99] J Puerta-Pelayo. "Images of CMS MUONs - Resistive Plate Chambers (RPC)." CMS Collection. 2008. URL: https://cds.cern.ch/record/1431509.

[100] R. Fruhwirth. "Application of Kalman filtering to track and vertex fitting." In: *Nucl. Instrum. Meth. A* 262 (1987), pp. 444–450. DOI: 10.1016/0168-9002(87)90887-4.

[101] Serguei Chatrchyan et al. "Performance of CMS Muon Reconstruction in *pp* Collision Events at $\sqrt{s} = 7$ TeV." In: *JINST* 7 (2012), P10002. DOI: 10.1088/1748-0221/7/10/P10002. arXiv: 1206.4071 [physics.ins-det].

[102] A. M. Sirunyan et al. "Performance of the CMS muon detector and muon reconstruction with proton-proton collisions at $\sqrt{s} = 13$ TeV." In: *JINST* 13.06 (2018), P06015. DOI: 10.1088/1748-0221/13/06/P06015. arXiv: 1804.04528 [physics.ins-det].

[103] A. M. Sirunyan et al. "Particle-flow reconstruction and global event description with the CMS detector." In: *JINST* 12.10 (2017), P10003. DOI: 10.1088/1748-0221/12/10/P10003. arXiv: 1706.04965 [physics.ins-det].

[104] Torbjörn Sjostrand et al. "An Introduction to PYTHIA 8.2." In: *Comput. Phys. Commun.* 191 (2015), p. 159. DOI: 10.1016/j.cpc.2015.01.024. arXiv: 1410.3012 [hep-ph].

[105] Vardan Khachatryan et al. "Event generator tunes obtained from underlying event and multiparton scattering measurements." In: *The European Physical Journal C* 76 (2016), pp. 1–52.

[106] N. Davidson, T. Przedzinski, and Z. Was. "PHOTOS interface in C++: Technical and Physics Documentation." In: *Comput. Phys. Commun.* 199 (2016), pp. 86–101. DOI: 10.1016/j.cpc.2015.09.013. arXiv: 1011.0937 [hep-ph].

[107] T. Pierog et al. "EPOS LHC: test of collective hadronization with data measured at the CERN Large Hadron Collider." In: *Phys. Rev. C* 92 (2015), p. 034906. DOI: 10.1103/PhysRevC.92.034906. arXiv: 1306.0121 [hepph].

[108] S. Agostinelli et al. "GEANT4—a simulation toolkit." In: *Nucl. Instrum. Meth. A* 506 (2003), p. 250. DOI: 10.1016/S0168-9002(03)01368-8.

[109] V Khachatryan et al. "Measurement of the production cross section ratio σ(Xb2(1P)) / σ(Xb1(1P) in pp collisions at $\sqrt{s} = 8$ TeV." In: *Phys. Lett. B* 743 (2015), pp. 383–402. DOI: 10.1016/j.physletb.2015.02.048. arXiv: 1409.5761 [hep-ex].

[110] A. M. Sirunyan et al. "Observation of the χ_{b1}(3P) and χ_{b2}(3P) and measurement of their masses." In: *Phys. Rev. Lett.* 121 (2018), p. 092002. DOI: 10.1103/PhysRevLett.121.092002. arXiv: 1805.11192 [hep-ex].

[111] O. Kukral et al. "Muon performance studies in 2017 pp and 2018 PbPb 5.02TeV data." CMS Analysis Note AN-2018-316. 2022.

[112] CMS Collaboration. "Performance of muon identification in pp collisions at $\sqrt{s} =$ 7 TeV." In: CMS-PAS-MUO-10-002 (2010). URL: https://cds.cern.ch/record/1279140.

[113] A. M. Sirunyan et al. "Performance of the CMS muon detector and muon reconstruction with proton-proton collisions at $\sqrt{s} = 13$ TeV." In: *JINST* 13.06 (2018), P06015. DOI: 10.1088/1748-0221/13/06/P06015. arXiv: 1804.04528 [physics.ins-det].

[114] P.A. Zyla et al. "Review of Particle Physics." In: *PTEP* 2020 (2020), p. 083C01. DOI: 10.1093/ptep/ptaa104.

[115] David G. d'Enterria. "Hard scattering cross-sections at LHC in the Glauber approach: From pp to pA and AA collisions." In: (Feb. 2003). arXiv: nucl-ex/0302016.

[116] M. J. Oreglia. "A study of the reactions $\psi' \to \gamma\gamma\psi$." SLAC Report SLAC-R-236, see Appendix D. PhD thesis. Stanford University, 1980. URL: http://www.slac.stanford.edu/pubs/slacreports/slac-r-236.html.

[117] Diego Martinez Santos and Frederic Dupertuis. "Mass distributions marginalized over per-event errors." In: *Nucl. Instrum. Meth. A* 764 (2014), pp. 150–155. DOI: 10.1016/j.nima.2014.06.081. arXiv: 1312.5000 [hep-ex].

[118] Betty Abelev et al. "J/ψ polarization in pp collisions at $\sqrt{s} = 7$ TeV." In: *Phys. Rev. Lett.* 108 (2012), p. 082001. DOI: 10.1103/PhysRevLett.108.082001. arXiv: 1111.1630 [hep-ex].

[119] S. Acharya et al. "Measurement of the inclusive J/ ψ polarization at forward rapidity in pp collisions at $\sqrt{\mathbf{s}} = \mathbf{8}$ TeV." In: *Eur. Phys. J. C* 78.7 (2018), p. 562. DOI: 10.1140/epjc/s10052-018-6027-2. arXiv: 1805.04374 [hep-ex].

[120] Albert M Sirunyan et al. "Constraints on the χ_{c1} versus χ_{c2} Polarizations in Proton-Proton Collisions at $\sqrt{s} = 8$ TeV." In: *Phys. Rev. Lett.* 124.16 (2020), p. 162002. DOI: 10.1103/PhysRevLett.124.162002. arXiv: 1912.07706 [hep-ex].

[121] Vincent Cheung and Ramona Vogt. "Private communication, calculation based on "Production and polarization of prompt J/ψ in the improved color evaporation model using the k_T-factorization approach"." In: *Phys. Rev. D* 98.11 (2018), p. 114029. DOI: 10.1103/PhysRevD.98.114029. arXiv: 1808.02909 [hep-ph].

[122] K. J. Eskola, H. Paukkunen, and C. A. Salgado. "EPS09: A New Generation of NLO and LO Nuclear Parton Distribution Functions." In: *JHEP* 04 (2009), p. 065. DOI: 10.1088/1126-6708/2009/04/065. arXiv: 0902.4154 [hep-ph].

[123] Shreyasi Acharya et al. "Measurement of nuclear effects on ψ(2S) production in p-Pb collisions at $\sqrt{s_{\rm NN}}$ = 8.16 TeV." In: *JHEP* 07 (2020), p. 237. DOI: 10.1007/JHEP07(2020)237. arXiv: 2003.06053 [nucl-ex].

[124] Albert M Sirunyan et al. "Measurement of prompt ψ(2S) production cross sections in proton-lead and proton-proton collisions at $\sqrt{s_{\rm NN}} = 5.02$ TeV." In: *Phys. Lett. B* 790 (2019), pp. 509–532. DOI: 10.1016/j.physletb.2019.01.058. arXiv: 1805.02248 [hep-ex].

[125] A. Hoecker et al. *TMVA - Toolkit for Multivariate Data Analysis*. 2009. arXiv: physics/0703039 [physics.data-an].

[126] Yoav Freund and Robert E Schapire. "A Decision-Theoretic Generalization of On-Line Learning and an Application to Boosting." In: *Journal of Computer and System Sciences* 55.1 (1997), pp. 119–139. ISSN: 0022-0000. DOI: https://doi.org/10.1006/jcss.1997.1504.

[127] R. A. Fisher. "The use of multiple measurements in taxonomic problems." In: *Annals of Eugenics* 7.2 (1936), pp. 179–188. DOI: https://doi.org/10.1111/j.1469-1809.1936.tb02137.x.